Exploring Defects in Superconducting Qubits: Fully Tunable Flux Qubits and Parasitic RF-SQUIDS

Zur Erlangung des akademischen Grades eines

Doktors der Naturwissenschaften (Dr. rer. nat.)

von der KIT-Fakultät für Physik des

Karlsruher Instituts für Technologie (KIT)

genehmigte

Dissertation

von

M.Sc. Benedikt Berlitz

Tag der mündlichen Prüfung:	24.04.2026
Referent:	Prof. Dr. Alexey V. Ustinov
Korreferent:	Prof. Dr. Alexander Shnirman

Contents

1 Introduction

1.1 Qubits

Quantum computing is a computational paradigm that leverages phenomena occurring at the quantum level to achieve increased computational power. It was proposed by Richard Feynman in 1981 [1] and later formalized by David Deutsch in 1985 [2].
Replacing the 0 and 1 state of the classical bit by the quantum states $|0\rangle$ and $|1\rangle$ of a quantum bit (qubit) allows one to access superposition states and entanglement of multiple qubits. Performing appropriate manipulations in the form of a quantum algorithm on a set of qubits could solve certain computational problems orders of magnitude faster than any classical algorithm [3].
Formally, a qubit is a two-level quantum system, represented by the Hamiltonian

$$\hat{H} = \frac{1}{2}\hbar\omega_q\hat{\sigma}_z, \tag{1.1}$$

where ω_q is the angular qubit eigen-frequency associated with the energy difference between the two eigen-states $E_1 - E_0 = \hbar\omega_q$ and $\hat{\sigma}_z$ is the z-Pauli-operator. The possible states of the qubit can be intuitively represented on the Bloch sphere, as is illustrated in Fig. 1.1 a). Any pure state can be written as

$$|\psi\rangle = \cos\left(\frac{\theta}{2}\right)|0\rangle + e^{i\phi}\sin\left(\frac{\theta}{2}\right)|1\rangle, \tag{1.2}$$

where θ and ϕ correspond to the polar and azimuthal angles on the sphere, respectively. In this picture, the north and south poles represent the ground and excited states, while points on the equator correspond to equal superpositions of the two. In the ideal case of an isolated qubit, the vector of the qubit state will precede around the quantization axis with an angular momentum of ω_q. Single qubit gates, e.g. manipulations of the qubit state, are realized by applying drives of various strengths and angles to the Bloch-Vector and will be discussed in chapter 3.
In reality, qubits interact with their environment, which allows for the dissipation of their energy. This energy relaxation process is represented by a relaxation rate Γ, with which the qubit spontaneously decays into its ground state. Furthermore,

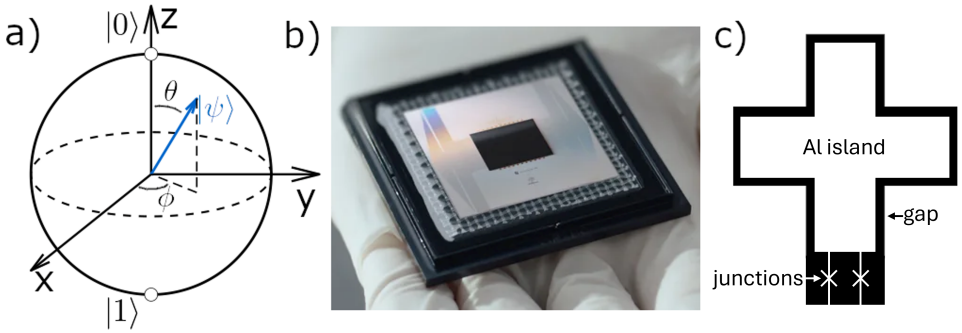

Figure 1.1: a) A Bloch-Sphere representing a qubit state $|\psi\rangle$, defined by the angles θ and ϕ. b) A photograph of the Willow quantum processor, consisting of 105 individual transmon qubits [4]. c) Top-view schematic of a transmon qubit. Two Josephson junctions, denoted by the X symbols, are shunted by a capacitance formed by the superconducting island, which is separated from the surrounding ground plane by a small gap.

real qubits experience fluctuations in their Larmor frequency (ω_q), leading to a loss of phase coherence.
These processes of energy relaxation and decoherence represent a central obstacle to large scale quantum computing, and are further explored in chapter 2.5.

1.2 Superconducting Qubits

There is a diversity of physical systems which are being researched for their usability as qubits. In principle, any system that can house two quantum states while fulfilling a short list of criteria, which were proposed by David DiVincenzo in the year 2000, can be considered a qubit [5]. Prominent examples include trapped ions, semiconductor spins, photons, and superconducting circuits, to name just a few. Among these, superconducting qubits have emerged as one of the most promising candidates for scalable quantum computing, owing to their design flexibility and straightforward integration with microwave control electronics.
Today's most advanced quantum processors, like the Google Willow depicted in Fig. 1.1 b) [4], are built from superconducting circuits of the transmon type. As shown in Fig. 1.1 c), a transmon qubit consists of a pair of Josephson tunnel junctions, a shunt capacitance, and is coupled to a harmonic oscillator, which functions as a readout resonator. All of these concepts will be explored in detail in chapter 2.
In a 2019 breakthrough, Google demonstrated the advantage of quantum computing over classical computers in a circuit sampling experiment [3]. In two hundred

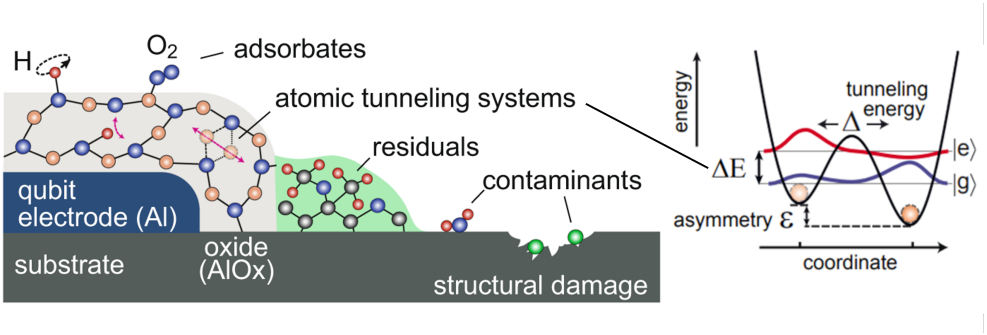

Figure 1.2: Left: Schematic of various imperfections found on a qubit sample (from [6]). Right: an atomic tunneling defect is modeled as a particle (orange sphere) trapped in a double-well potential characterized by the tunneling energy Δ and the potential asymmetry ε. This gives rise to the name-giving two levels $|g\rangle$ and $|e\rangle$ of the two-level system [7].

seconds, the quantum processor performed an assigned task that is estimated to require several days of computation on a conventional supercomputer.
Despite milestone experiments like this, superconducting qubits have yet not entered the regime of large scale quantum computing. A major challenge remains their limited coherence, which continues to be the focus of intensive research.

1.3 TLS and Motivation

A central impediment to the coherence of superconducting qubits is the presence of atomic-scale material defects in the amorphous oxide layers on the chip surface and in the Josephson tunnel junctions. While their exact microscopic nature is subject of ongoing debate, they are most commonly pictured as atoms that can tunnel between two positions in the amorphous lattice. These defects form two-level systems (TLS) as illustrated in Fig. 1.2. Via their dipole moment, they couple to the AC-electric field of the qubit sample on which they reside, which allows them to act as channels for energy relaxation. The ubiquitous presence of amorphous oxides in superconducting technology makes TLS-caused energy relaxation a challenging problem.
Strategies to mitigate their detrimental effects include qubit design optimized to reduce the coupling electric fields [8], the avoidance of stray junctions[9], and the detuning of TLS from the qubit via electric fields [6]. The study of TLS defects is necessary to further the coherence of superconducting quantum technology.

For the past 50 years TLS have been described by the standard tunneling model (STM)[10]. It describes the tunneling atom as a particle trapped in a double-well

potential characterized by a tunneling energy Δ and a potential asymmetry ε, as shown in Fig. 1.2. The energy splitting of the TLS defects is then given by

$$\Delta E_{\mathrm{TLS}} = \sqrt{\Delta^2 + \varepsilon^2}. \tag{1.3}$$

More details on the theory of TLS will be given in section 2.1. The STM assumes random distributions of the parameters defining the TLS defects and has been used to describe the low-temperature behavior of amorphous substances[11].
While being a robust and well-tested theory, many questions about TLS remain, which are not captured by the STM. For example, it leaves out the coupling of TLS among each other, which has been explicitly verified using superconducting qubits in 2015 [12][13]. Further questions remain about the exact microscopic origins of TLS defects. Beside individual tunneling atoms, alternative proposals include tunneling electrons, non-equilibrium quasi-particles, or the collective motion of several atoms[14],[15].
Therein lie the two main motivations of the research done in this work. On the one hand, revealing the properties of individual TLS using superconducting qubits will allow us to better understand their underlying physics which have puzzled researchers for many decades. On the other hand, this understanding will further help us to tackle the pressing issue of decoherence in superconducting qubits and thereby may pave the way to practical large scale quantum computing.
A powerful method to study the properties of defects is swap-spectroscopy, which is detailed in section 3.5. This technique reveals the resonance frequencies of individual defects interacting with a qubit via their detrimental effect on its energy relaxation. Thus turning the qubit's sensitivity to defects into a feature, swap spectroscopy has since been used to study individual defects' properties, such as their reaction to mechanical strain and electric fields[6][7], their dipole-moment, their tunneling energy, and their location [16],[17].
In this work, we aim to expand the scope of defect detection in superconducting qubits in two ways.
Firstly, we employ qubit types previously unused in defect spectroscopy: fluxmon qubits and newly developed fully tunable C-shunted flux qubits of our own design, which are further detailed in chapters 2 and 3. An increase in qubit frequency tuning range, and thereby in the TLS detection frequency window, is the main focus of this approach. The results are presented in section 4.
Another approach we pursue is to study the response of defects to magnetic fields. While aiming to reveal the prevalence of magnetically sensitive submicroscopic defects, such as quasiparticle TLS or isolated spins, we made the unexpected discovery of a new type of macroscopic defect. A parasitic RF-SQUID, which was surprisingly formed by the on-sample bonding wires, was shown to interfere destructively with qubit operation. This unforeseen finding has implications for

qubit prototyping and wider superconducting technology, and is detailed in section 5.

1.4 Flux Qubit Development

As the main approach of this thesis consists of the design of fully tunable flux qubits, we want to briefly review the development of this technology and highlight important experiments here, while in-depth technical details are given in sections 2 and 3.
The original flux qubit [18, 19] consisted of a superconducting loop that is interrupted by three Josephson junctions. In early experiments, flux qubits were read out by measuring the flux through the qubit loop using a DC-SQUID in switching-current [20] or dispersive measurements [21], and were used to demonstrate two-qubit gates [22], access the ultra-strong coupling cavity QED regime [23, 24], and multiplexed qubit readout [25] through coupling to transmission line resonators.
The quantum coherence of flux qubits has been subject to steady, incremental improvement over the past years. Bertet *et al.* [26] and Yoshihara *et al.* [27] reported T_1 times of 2-4µs in early experiments, which were likely limited by strongly coupled readout-SQUIDs. Subsequently, longer T_1 times of 6-20 µs were reached by Orgiazzi *et al.* [28] and Stern *et al.* [29], by replacing the readout-SQUID with coplanar waveguide resonators and 3D cavities, respectively.
Another design improvement was the addition of a shunt-capacitor. While in early experiments using interdigitated capacitors by Steffen *et al.* [30] and Córcoles *et al.* [31], T_1 times were limited to 1-6 µs, Yan *et al.* demonstrated coherence times of $T_1 \approx 50$ µs, using larger square-plate shunt-capacitors [32]. This breakthrough, which they attributed to reduced dielectric loss in their shunt capacitors and a reduction in the qubit persistent current (I_p), put flux qubits close to the coherence of transmon qubits.

1.5 Fully tunable Flux Qubits

The flux qubit variants studied in this work are "fully tunable" or "gap-tunable" flux qubits. A fully tunable flux qubit has an additional loop which allows for *in situ* control of the tunneling barrier in the qubit's double-well potential, which is illustrated in Fig. 1.3 c). This was first experimentally realized by Paauw *et al.* [33],

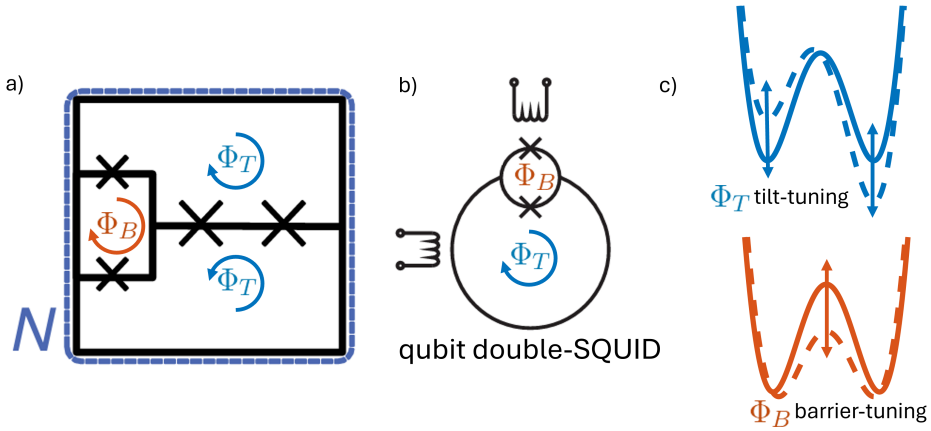

Figure 1.3: Example schematics of fully tunable flux qubits. a) Paauw *et al.*'s first experimental realization of the concept [33]. The qubit is controlled via the control fluxes Φ_T and Φ_B, with the outermost loop (blue dashed line) trapping N fluxoids to prebias the qubit. b) Poletto *et al.*'s double-SQUID qubit design uses two junctions and a large superconducting loop [34], with local coils inducing the bias fluxes. Both designs were read-out using a DC-SQUID (not shown). c) Schematic of the potential energy control in a fully tunable flux qubit, with Φ_T and Φ_B controlling the potential tilt and tunnel barrier height, respectively.

whose design is shown schematically in Fig. 1.3 a). Soon after, Poletto *et al.* demonstrated operation in both the flux qubit regime, where the potential has the shape of a double-well and the phase qubit regime, where the potential has a single well [34], using a double-SQUID qubit design shown in Fig. 1.3 b). This control of the qubit potential makes fully tunable flux qubits attractive for different applications, such as quantum annealing [35, 36], as couplers and computational qubits in quantum processors [37, 38], for use in quantum metamaterials [39], and for microwave-free qubit manipulation [40]. Fully tunable flux qubits are particularly well suited for investigating decoherence sources, since a single device can access both flux-like and phase-like operating regimes. Their wide tunability enhances the accessible range for swap-spectroscopy scanning of their electromagnetic environment.
So far, balancing the enhanced qubit tunability with good coherence has been proven to be difficult. Early fully tunable designs exhibited T_1 times between 1.4 ns and 1.5 µs, which have been attributed to thermal noise[33], and dielectric loss[34], respectively. In a recent experiment using an asymmetric α-junction SQUID, Chang *et al.* reported T_1 times up to 8 μs [38], attributing this limit to dielectric loss. However, this approach limits the tuning range of the device (about 7 GHz was reported). Despite this significant improvement in energy relaxation, a fully tunable flux qubit, which combines access to a wide tuning range with a long T_1 time has

not yet been achieved.
With the fully tunable C-shunted flux qubits we present a design that combines the advantageous coherence properties of the C-shunted flux qubit with full tunability in sections 2, 3 and 4. During this thesis we show how this design is a useful platform for defect spectroscopy and further applications, with a tuning range of up to 20 GHz and a competitive energy relaxation time of over 25 µs.

2 Theory

2.1 Two-Level Systems (TLS)

Two-level systems (TLSs) are ubiquitous microscopic defects in amorphous materials. Their description as an ensemble of tunneling particles shapes our understanding of the low-temperature properties of glasses since the 70s [10, 11]. Nowadays, their detrimental effect on the coherence of newly emerging quantum technology revitalizes the study of TLS with both renewed urgency and new tools. This very work aims to be part of this effort, and we shall begin by reviewing the basic theory of TLS.

2.1.1 Standard Tunneling Model

The standard tunneling model (STM) describes a TLS as a virtual particle trapped in a one-dimensional double-well potential. The Hamiltonian of an individual TLS is

$$\hat{H}_{\mathrm{TLS}} = \frac{\hbar}{2}\Delta\hat{\sigma}_x + \frac{\hbar}{2}\varepsilon\hat{\sigma}_z = \frac{\hbar}{2}\begin{pmatrix}\varepsilon & \Delta\\ \Delta & -\varepsilon\end{pmatrix}. \tag{2.1}$$

where $\hbar\varepsilon$ is the asymmetry energy between the two wells, and $\hbar\Delta$ is the tunneling energy between the two lowest bound states. In the common image of the TLS as an atom tunneling between two positions in the amorphous lattice, this tunneling energy is in dependence of the tunneling mass m, the tunneling distance d, the barrier height V_0 and the ground state energy E_0 given by

$$\Delta = E_0 e^{-\lambda}, \lambda = \frac{d}{\hbar}\sqrt{2mV}. \tag{2.2}$$

Diagonalization of the Hamiltonian gives the energy splitting

$$E = \hbar\sqrt{\Delta^2 + \varepsilon^2}, \tag{2.3}$$

where we note the hyperbolical dependence on ε, as depicted in Fig. 2.1.

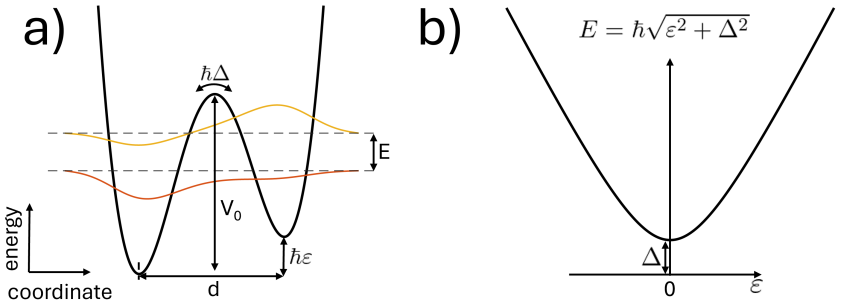

Figure 2.1: a) The double-well potential of a single TLS defect as defined by the STM. It describes a virtual particle tunneling between two configurations, separated by a tunneling distance d and a potential barrier V_0, giving rise to the tunneling energy $\hbar\Delta$. The tunneling energy together with the asymmetry energy $\hbar\varepsilon$ define the TLS' splitting energy E between the TLS energy levels (dashed lines). b) E depends hyperbolically on ε, with $\hbar\Delta$ defining its minimum. This gives rise to observable TLS parabola, when ε is varied intentionally by applied strain or electric fields.

2.1.2 TLS Density of States

Due to the disorder of amorphous solids, individual TLS parameters are randomly distributed. As a central assumption, the STM assumes the parameters ε and λ to be independent and uniformly distributed in the intervals $d\varepsilon$ and $d\lambda$, i.e.

$$P(\varepsilon, \lambda) = P_0 d\varepsilon d\lambda, \tag{2.4}$$

where P_0 is a constant. From this distribution we gain the TLS' density of states (DoS) $D(E)$, by re-expressing in terms of E and Δ,

$$P(E, \Delta) d\Delta dE = P_0 \frac{E}{\Delta\sqrt{E^2 - \hbar^2\Delta^2}} d\Delta dE, \tag{2.5}$$

and integrating over Δ

$$D(E) = \int_{\hbar\Delta_{\min}}^{E} P(E, \Delta) d\Delta = P_0 \ln \frac{2E}{\hbar\Delta_{\min}} \approx D_0, \tag{2.6}$$

where $\Delta_{\min}$ is the minimal Δ which still allows for tunneling between the wells. The DoS is approximately constant over the energy scales of interest, where $\hbar\Delta_{\min} \ll E$. This assumption holds for amorphous glasses in general and typical experimental energy scales [14].

2.1.3 TLS Interaction with Environment

There are two mechanisms by which TLS couple to their environment. As localized defects, they couple to local strain in the form of phonons or deformation of the sample, and as charged particles, they couple to electric fields via their dipole moment. These effects can be described by the interaction Hamiltonian

$$\hat{H}_{\text{int}} = \begin{pmatrix} 1 & 0 \\ 0 & 1 \end{pmatrix} \boldsymbol{p}\boldsymbol{F} + \begin{pmatrix} 1 & 0 \\ 0 & 1 \end{pmatrix} \boldsymbol{\gamma}\boldsymbol{\xi}, \tag{2.7}$$

where $\boldsymbol{F}$ is the electric field, $\boldsymbol{p}$ is the TLS' electric dipole moment, ξ is the strain field and γ the TLS' elastic dipole moment. Combining equations (2.1) and (2.7) with the definitions of the dipole moments $\boldsymbol{d} \equiv \partial\varepsilon/2\partial\boldsymbol{E}$ and $\gamma \equiv \partial\varepsilon/2\partial\xi$, we find the dependence of the TLS' energy splitting on the applied fields

$$E(\boldsymbol{F}, \boldsymbol{\xi}) = \hbar\sqrt{\Delta^2 + \left(\varepsilon + \frac{2\boldsymbol{p}\boldsymbol{F}}{\hbar} + \frac{2\boldsymbol{\gamma}\boldsymbol{\xi}}{\hbar}\right)^2}. \tag{2.8}$$

These interactions are fundamental to the research presented here in several ways. The TLS couple to the oscillating supercurrents in a qubit circuit via their dipole moment, which allows for the dissipation of the qubit's excitation into the TLS bath. This effect, which is further explored in section 2.5.5, makes TLS one of the leading limitations to the lifetime of superconducting qubits. At the same time, this sensitivity is exploited to study the energy splitting of individual TLS using the methods detailed in section 3.5. During these measurements, electric fields and mechanical strain are applied to the sample, tuning the individual TLS' energy splittings, and revealing the hyperbolic behaviour predicted by Eq. (2.8).

2.2 Superconducting Circuits and Josephson Junction Physics

The qubits presented in this work are superconducting qubits, which means they are microcircuits patterned from a superconducting material. Here, we use Aluminium which is cooled to millikelvin temperature. These circuits combine macroscopic electrical elements like inductors, capacitors, and Josephson junctions into engineered quantum systems whose dynamics can be described by the laws of quantum mechanics. Unlike conventional electronic devices, superconducting circuits exploit the collective behavior of Cooper pairs, which move without resistance and maintain long-range phase coherence. This macroscopic quantum coherence allows

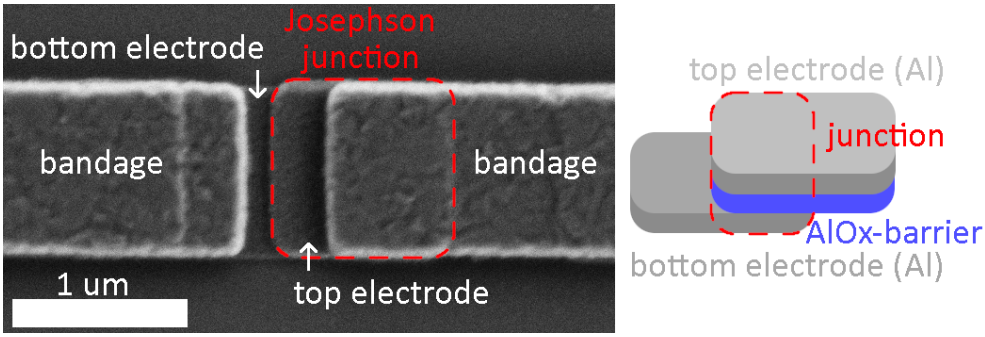

Figure 2.2: SEM-image and schematic of a Josephson junction. The superconducting aluminium electrodes are separated by a layer of aluminium-oxide, which allows Cooper pairs to tunnel between the two. The SEM also shows a third 'bandage'-layer of aluminium on top of the two electrodes, whose purpose is detailed in section 3.1

superconducting circuits to behave as artificial atoms, exhibiting discrete energy spectra and enabling strong, controllable coupling to electromagnetic fields.

The central element of superconducting qubits is the **Josephson junction**, a weak link between two superconductors separated by a few nanometers of an insulating barrier, as depicted in figure 2.2. The underlying Josephson effect, for which Brian D. Josephson received the 1973 Nobel Prize in Physics, introduces intrinsic nonlinearity into the otherwise harmonic dynamics of linear circuits. This nonlinearity is essential for defining and manipulating quantum states, as it allows the circuit's energy levels to become anharmonic and individually addressable, which we will see in the following chapter.

2.2.1 Basic Josephson Effect

The fundamental phenomena associated with a Josephson junction arise from the quantum mechanical phase coherence of the superconducting condensate. According to the Ginzburg-Landau theory [41], each superconducting electrode is described by a macroscopic wavefunction of the form

$$\Psi = |\Psi| e^{i\varphi}, \tag{2.9}$$

where φ is the superconducting phase. When two superconductors are brought into weak contact through a thin insulating barrier, their phases φ_1 and φ_2 are no longer independent. Instead, a supercurrent can tunnel across the barrier which depends on the phase difference

$$\delta = \varphi_1 - \varphi_2 \tag{2.10}$$

across the junction, and is described by the two Josephson equations [42]:

1. Current-phase relation:

$$I_s = I_c \sin\delta, \tag{2.11}$$

where I_s is the supercurrent across the junction and I_c is the critical current, e.g. the maximum supercurrent. It describes a constant supercurrent tunneling across the junction, even in the absence of an applied voltage, which is known as the **DC Josephson effect**.

2. Voltage-phase relation:

$$\frac{d\delta}{dt} = \frac{2e}{\hbar}V, \tag{2.12}$$

where V is an applied voltage across the junction, e is the elementary charge, and $\hbar$ is the reduced Planck constant. This equation expresses that a constant voltage drives a linear evolution of the phase difference, and in combination with Eq. 2.11 describes the **AC Josephson effect**:

$$I_s(t) = I_c \sin(\delta(t)) = I_c \sin(\delta_0 + \frac{2eV}{\hbar}t), \tag{2.13}$$

which means that voltage across the junction induces a supercurrent oscillation with the frequency

$$\omega_J = \frac{2eV}{\hbar} = \frac{2\pi}{\phi_0}V, \tag{2.14}$$

introducing the flux quantum $\phi_0 = h/2e$.
We can see that the Josephson junction behaves as a nonlinear inductive element, by expanding the sine in Eq. 2.13 to first order and using the voltage relation $V(t) = \frac{\phi_0}{2\pi}\dot{\delta}$, leading to

$$V(t) = \frac{\phi_0}{2\pi}\frac{\dot{I}(t)}{I_c\cos\delta} \equiv L_J\dot{I}(t), \tag{2.15}$$

which is equivalent to the linear inductance relation $V = -L \cdot dI/dt$, but with the non-linear Josephson inductance

$$L_J = \frac{\hbar}{2eI_c\cos\delta}. \tag{2.16}$$

Using the same relations, we can further derive the energy stored in the junction as a function of δ:

$$U(\delta) = \int P\,dt = \frac{\Phi_0}{2\pi}\int I(\delta)\,d\delta \;= \frac{\Phi_0 I_c}{2\pi}\int \sin\delta\,d\delta \;= -\frac{\Phi_0 I_c}{2\pi}\cos\delta + C. \tag{2.17}$$

Defining the **Josephson energy** $E_J = \frac{\hbar I_c}{2e}$, we arrive at the expression

$$U(\delta) = -E_J\cos(\delta), \tag{2.18}$$

which is an important term used in the Hamiltonian descriptions of the circuits used in this work.
The Josephson energy depends on the geometry of the junction, as it increases proportionally with the junction area, and decreases exponentially with the thickness of the tunnel junction. This can be easily understood from the **Ambegaokar-Baratoff relation**

$$I_c R_n = \frac{\pi\Delta_{\mathrm{Al}}}{2e}, \tag{2.19}$$

which relates a junction's room temperature resistance R_n to its critical current and the material's superconducting gap Δ_{Al} (aluminium here). Thus, a single junction's parameters are fixed during fabrication, and can be probed via room temperature resistance measurements.

2.2.2 DC-SQUID: a Tunable Josephson Junction

Experiments with qubits often require the tuning of a circuit's critical current *in situ*. For this purpose a DC-SQUID (Superconducting Quantum Interference Device) can be employed. Originally developed as a very sensitive magnetometer [43], the DC-SQUID consists of a superconducting loop containing two Josephson junctions. Effectively, it acts as a Josephson junction, whose Josephson energy depends on the external flux applied to the SQUID loop.
To understand this behavior, we need to introduce the concept of *flux quantization*. Since the superconducting condensate is described by a wavefunction of the form shown in Eq. (2.9), the total phase change around a superconducting loop has to be a multiple of 2π, which can be expressed as

$$\oint_{\mathcal{C}} \left(\nabla\varphi - \frac{2\pi}{\Phi_0}\mathbf{A}\right)\cdot d\mathbf{l} = 2\pi m. \tag{2.20}$$

Using Stokes' theorem and $\oint \mathbf{A}d\mathbf{l} = \Phi_{\mathrm{tot}}$ being the total magnetic flux through the loop, we get

$$\Delta\varphi_{\mathrm{tot}} + \frac{2\pi}{\Phi_0}\Phi_{\mathrm{tot}} = 2\pi m. \tag{2.21}$$

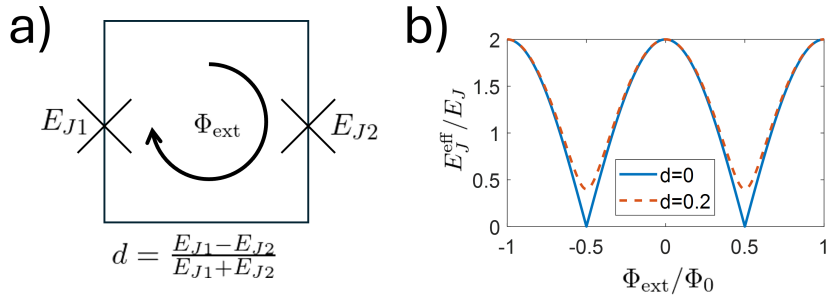

Figure 2.3: a) Circuit schematic of a DC-SQUID. Two Josephson junctions with respective Josephson energies E_{J1} and E_{J2} share a superconducting loop, which is threaded by the external flux Φ_{ext}. The parameter d describes the asymmetry between the junctions. b) The DC-SQUID's effective Josephson energy E_J^{eff} in dependence of Φ_{ext} for different values of d, according to Eq. (2.26). The plot is normalized by the average Josephson energy $E_J = (E_{J1} + E_{J2})/2$. We note that junction asymmetry results in a lower bound to the E_J^{eff} tuning range.

In the case of a superconducting loop interrupted by n Josephson junctions, $\Delta\varphi_{\text{tot}}$ is the sum of the phase differences across the junctions, and Φ_{tot} is given by the external magnetic flux Φ_{ext}, leading to the condition

$$\sum_{j=1}^{n} \delta_j + \frac{2\pi}{\Phi_0}\Phi_{\text{ext}} = 2\pi m. \tag{2.22}$$

Neglecting the geometric inductance of the loop, and using equation 2.11, the inductance of the DC-SQUID reads as

$$I_{\text{DCSQUID}} = I_{c1}\sin\delta 1 + I_{c2}\sin\delta_2. \tag{2.23}$$

Defining the average phase $\delta_m = \frac{\delta_1+\delta_2}{2}$. and using the flux quantization relation (Eq. (2.22)) we find

$$I_{\text{DCSQUID}} = I_{c1}\sin\left(\delta_m - \frac{\pi\Phi_{\text{ext}}}{\Phi_0}\right) + I_{c2}\sin\left(\delta_m + \frac{\pi\Phi_{\text{ext}}}{\Phi_0}\right). \tag{2.24}$$

In the symmetrical case $I_{c1} = I_{c2} = I_c$, Eq. (2.24) reduces to:

$$I_{\text{DCSQUID}} = 2I_c\cos\frac{\pi\Phi_{\text{ext}}}{\Phi_0}\sin\delta_m \tag{2.25}$$

By comparison with Eq. (2.24), we see that the device behaves like a single effective Josephson junction with a tunable critical current of $2I_c\cos\frac{\pi\Phi_{\text{ext}}}{\Phi_0}$, and an effective Josephson energy of

$$E_J^{\text{eff}}(\Phi_{\text{ext}}) = 2E_J\cos\left(\frac{\pi\Phi_{\text{ext}}}{\Phi_0}\right), \tag{2.26}$$

where Φ_{ext} is the external magnetic flux threading the loop. This flux dependence allows in-situ tuning of the qubit transition frequency when a DC-SQUID is used in place of a fixed Josephson junction.
In the case of a small asymmetry between the junctions, the effective Josephson energy generalizes to

$$E_J^{\text{eff}}(\Phi_{\text{ext}}) = 2E_J \cos\left(\frac{\pi\Phi_{\text{ext}}}{\Phi_0}\right)\sqrt{1 + d^2 \tan\left(\frac{\pi\Phi_{\text{ext}}}{\Phi_0}\right)^2}, \tag{2.27}$$

with the asymmetry factor $d = \frac{E_{J1}-E_{J2}}{E_{J1}+E_{J2}}$ and assuming $E_{J1} + E_{J2} = 2E_J$ for ease of comparison. As can be seen in Fig. 2.3, an asymmetry factor $d > 0$ leads to a reduction in the E_J^{eff}-tuning range of the DC-SQUID and a reduced $dE_J^{\text{eff}}/d\Phi_{\text{ext}}$ dependency.

2.3 The Hamiltonian Formalism for Superconducting Circuits

Despite being macroscopic objects consisting of many atoms, the physics of a qubit can often be described by a simple one-dimensional Hamiltonian, representing the dynamics of charges tunneling across the qubit junctions. This is possible in the so called lumped element limit, in which the circuit elements, such as capacitors, inductances and junctions, are much smaller than the wavelengths of the relevant modes of the circuit.

2.3.1 Harmonic Oscillator Hamiltonian

The simplest example of a quantum circuit is the oscillator circuit, formed by a capacitance C and a linear inductance L, as shown in Fig. 2.4 a) and b). The depicted circuit describes the coplanar waveguide resonators we use for qubit readout in the lumped-element limit. The two elements contribute to the Lagrangian of the system through their energies $T = \dot{\Phi}C/2$ and $V = \Phi^2/2L$ respectively, where Φ is the flux along the inductance. Introducing the charge $Q = \delta\mathcal{L}/\delta\dot{\Phi} = C\dot{\Phi}$ as the conjugate variable to Φ, one arrives at the classical Hamiltonian of the resonator

$$H_{\text{res}} = Q\dot{\Phi} - \mathcal{L}_{\text{res}} = \frac{Q^2}{2C} + \frac{\Phi^2}{2L}, \tag{2.28}$$

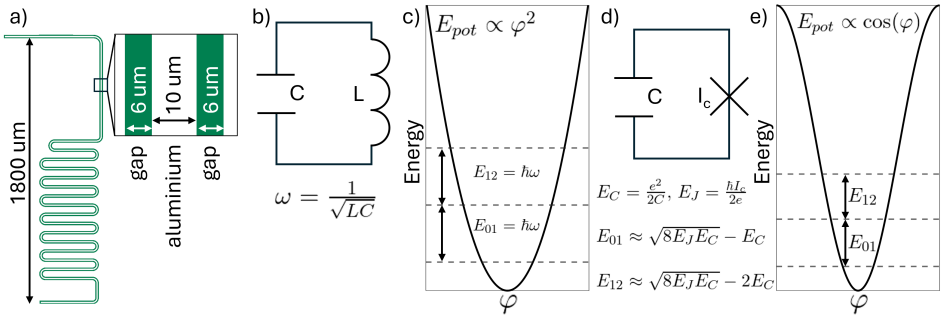

Figure 2.4: a) Schematic of a meander readout resonator. The zoom-in inset shows how in this coplanar waveguide design a central conductor is separated from the surrounding ground-plane. b) Idealized circuit-diagram of the resonator. Its resonance frequency ω is defined by its inductance L and capacitance C. c) Energy potential and spectrum of the resonator. The harmonic potential gives rise to equidistant energy states. d) Circuit-diagram of a transmon qubit which consists of a capacitance C and a Josephson junction with critical current I_c, which define the characteristic energy scales of the qubit, E_C and E_J. e) Energy potential and spectrum of a transmon qubit. In contrast to the linear inductance of the resonator, the Josephson junction provides an *anharmonic* potential, which gives rise to the different energy spacings E_{01} E_{02}. This allows for the transmon states to be addressed independently.

which is the well-known harmonic-oscillator form. We arrive at the quantum harmonic oscillator description by promoting Φ and Q to operators, fulfilling the commutation relation $[\hat{\Phi}, \hat{Q}] = i\hbar$

$$\hat{H}_{\text{res}} = \frac{\hat{Q}^2}{2C} + \frac{\hat{\Phi}^2}{2L} = \hbar\omega_{\text{res}}(\hat{a}^\dagger\hat{a} + \frac{1}{2}) = \hbar\omega_{\text{res}}(\hat{n}_{\text{res}} + \frac{1}{2}), \tag{2.29}$$

with the angular resonance frequency $\omega_{\text{res}} = 1/\sqrt{LC}$, the excitation number operator $\hat{n}_{\text{res}} = \hat{a}^\dagger\hat{a}$ and the ladder operator $\hat{a} = \sqrt{\frac{1}{2\hbar Z}}\hat{\Phi} + i\sqrt{\frac{Z}{2\hbar}}$, where $Z = \sqrt{\frac{L}{C}}$ is the characteristic impedance of the oscillator.
In other words, this Hamiltonian describes a flux particle of virtual mass C moving in a harmonic potential generated by the linear inductance, with the angular resonance frequency $\omega_{\text{res}} = 1/\sqrt{LC}$, which is illustrated in Fig. 2.4 c). For experiments, it is more useful to refer to the linear resonance frequency $f_{\text{res}} = \omega_{\text{res}}/2\pi$, which typically lies in the 5-10 GHz range.
Usually, we describe quantum circuits with respect to the superconducting phase difference $\varphi = 2\pi\Phi/\Phi_0$ and the Cooper-pair number operator $\hat{n} = \hat{Q}/2e = -i\partial/\partial\varphi$, leading to

$$\hat{H}_{\text{res}} = 4E_C\hat{n}^2 + \frac{1}{2}E_L\hat{\varphi}^2, \tag{2.30}$$

with the characteristic energy scales $E_C = e^2/2C$, $E_L = \Phi_0^2/L$.

2.3.2 Transmon Hamiltonian

As motivated in the introduction, the transmon qubit is a simple, yet powerful and widely used circuit, which consists of a Josephson junction which is shunted by a capacitance C, as depicted in Fig. 2.4 c). The transmon Hamiltonian can be derived analogous to the harmonic oscillator, by replacing the quadratic linear inductance term $V = \Phi^2/2L$ by that of a Josephson junction. According to equation 2.18, this gives us the potential term $V = E_J(1 - \cos(\Phi))$, which results in the Hamiltonian

$$\hat{H}_{\text{transmon}} = \frac{\hat{Q}^2}{2C_\Sigma} - E_J \cos(2\pi \frac{\hat{\Phi}}{\Phi_0}) = 4E_C\hat{n} - E_J \cos\hat{\varphi}, \tag{2.31}$$

with $E_C = e^2/2C_\Sigma$, where $C_\Sigma = C + C_J$ is the sum of the shunt capacitance C and the intrinsic capacitance of the Josephson junction C_J. Importantly, a transmon should be designed to have a large E_J/E_C-ratio, with the original publication suggesting a range of $20 < E_J/E_C \ll 5 \times 10^4$, which is also called the transmon limit [44]. Analogous to the harmonic resonator, this describes a phase particle moving in a cosine potential, as illustrated in Fig. 2.4 d). In contrast to the harmonic case, the potential of the Josephson junction introduces *anharmonicity* into the system. This leads to the important effect, that the energy levels of the transmon qubit are not equidistant, and can thus be addressed individually. The energy levels are approximately

$$E_m \approx -E_J + \sqrt{8E_CE_J}\left(m + \frac{1}{2}\right) - \frac{E_C}{12}(6m^2 + 6m + 3). \tag{2.32}$$

The *anharmonicity* α is a measure of how much the energy levels are not equidistant, and is defined as

$$\alpha \equiv E_{12} - E_{01} = E_2 - E_1 - E_1 - E_0, \tag{2.33}$$

which in the transmon case calculates to

$$\alpha_{\text{transmon}} = -E_C. \tag{2.34}$$

In the context of experiments with superconducting circuits, it is useful to express energies in terms of linear frequency, as it gives a more intuitive picture how the system interacts with microwave drives and its environment. For example, we define the qubit resonance frequency $f_q = E_{01}/h$.

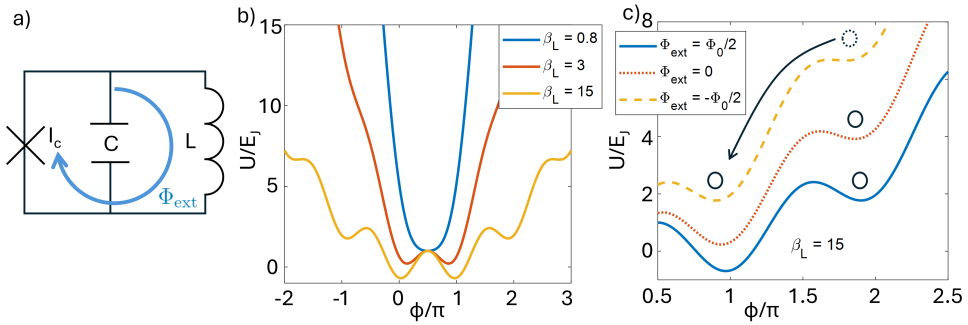

Figure 2.5: a) Circuit-diagram of an RF-SQUID, featuring a capacitance C, a linear inductance L, and a Josephson junction with critical current I_c. The loop formed by the junction and L is threaded by an external flux Φ_{ext}. b) RF-SQUID energy potentials for different values of the β_L parameter, at an external flux of $\Phi_{ext} = \Phi_0/2$. A higher β_L parameter leads to more potential wells. c) RF-SQUID energy potentials for different values of Φ_{ext} at a fixed $\beta_L = 15$. As the external flux changes, the local minimum, in which virtual particle (black circle) is trapped, becomes flatter and less stable, until the particle escapes.

2.3.3 RF-SQUID

Another common type of superconducting circuit is the RF-SQUID. As illustrated in Fig. 2.5 a), its most general form features a Josephson junction, a linear inductance and a capacitance. Similar to the DC-SQUID, it was originally used as a magnetometer, with the "RF" and "DC" naming convention being a reference to the historical readout methods for these devices. We will see that the RF-SQUID's combination of both a linear and a Josephson inductance in a superconducting loop leads to a versatile potential energy, which depends on the circuit parameters and the applied external flux. Understanding its flux-dependent and hysteretic properties allowed us to identify the presence of an unintended, parasitic RF-SQUID in one of our circuits, which is described in chapter 5.
The RF-SQUID Hamiltonian can be derived analogously to the harmonic oscillator and transmon case detailed in the previous section as

$$\hat{H} = \frac{\hat{Q}^2}{2C} - E_j \cos\left(2\pi\frac{\hat{\Phi}}{\Phi_0}\right) + \frac{(\hat{\Phi} - \Phi_{ext})^2}{2L} = 4E_C\hat{n}^2 - E_J\cos(\hat{\varphi}) + \frac{1}{2}E_L(\hat{\varphi} - \varphi_{ext})^2. \tag{2.35}$$

As with the DC-SQUID, the flux quantization condition links the fluxes along the superconducting loop via the applied external flux Φ_{ext}. The shape of the potential energy depends on Φ_{ext} and the inductance ratio $\beta_L = E_J/E_L = 2\pi L I_c/\Phi_0$, which is illustrated in Fig. 2.5.

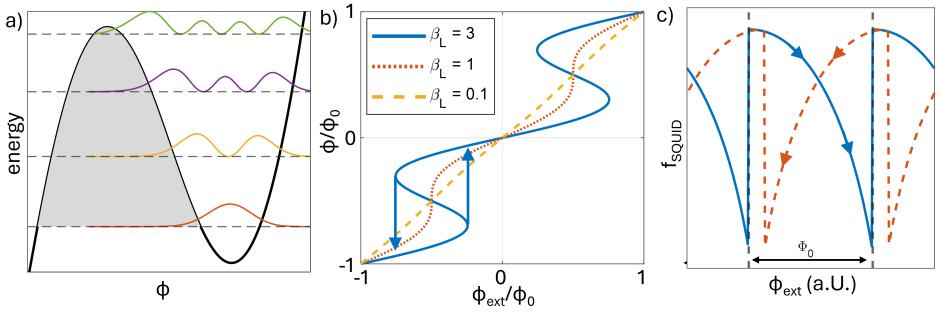

Figure 2.6: a) Energy potential and states of an RF-SQUID with $\beta_L = 15$ and $\Phi_{\text{ext}} = -\Phi_0/2$. In the case shown, where the system is trapped in a local minimum, the energy spacing is similar to that of a transmon, and the system behaves like a phase qubit. b) Plots showing the internal flux in the RF-SQUID Φ_q varying with the external flux Φ_{ext} for different values of β_L. For $\beta_L > 1$, this function becomes multivalued, which coincides with the presence of multiple metastable potential wells (see Fig. 2.5). Indicated by the arrows, the internal flux shows hysteretic behaviour for $\beta_L > 1$. c) Plot showing the RF-SQUID resonance frequency f_{SQUID} under variation of Φ_{ext}, with the solid blue line showing an increase and the dashed red line a decrease in Φ_{ext}, respectively. f_{SQUID} dips down in the sweep direction followed by sudden upward jumps in regular intervals. These jumps coincide with the internal flux jumps shown in subfigure b) and the well-jumps illustrated in Fig. 2.5 c).

For $\beta_L < 1$ the parabolic term dominates the potential energy and the RF-SQUID behaves like a slightly anharmonic oscillator. For $\beta_L > 1$ the Josephson term is strong enough to create additional local minima. This leads to a double-well potential when $\beta_L \gtrsim 1$ and a multi-well potential when $\beta_L \gg 1$.
In the double-well case, the RF-SQUID behaves like a persistent-current flux qubit, which will be detailed in the following section. In the multi-well case, the main mode is that of a phase particle oscillating in one of the potential wells, similar to a phase qubit. An example well with the corresponding energy levels is shown in Fig. 2.6 a). The energy levels depend on the exact shape of the potential well in which the phase particle is trapped, referred to as the "active well", with deeper wells leading to higher qubit frequencies, and flatter wells to lower. Here, the energy levels and eigenfunctions are calculated numerically from the Hamiltonian, using a method which is explained in section 2.4.
From the Hamiltonian we see that the external flux acts as an offset between the Josephson potential term and the harmonic term. Figure 2.5 c) shows the potential shape for different values of Φ_{ext}, with a black circle representing the phase particle indicating the active well. As Φ_{ext} is decreased, the active well flattens until the phase particle escapes into the next deeper well.

According to the Wentzel-Kramers-Brillouin approximation (WKB), the quantum escape rate from energy level n is given by

$$\Gamma_n \approx \frac{\omega_0}{2\pi} f_n \exp\left(-iS_n/\hbar\right), \tag{2.36}$$

where

$$S_n = \int_{\varphi_1}^{\varphi_2} \sqrt{2m[U(\varphi) - E_n]}\, d\varphi, \tag{2.37}$$

with the classical turning points φ_1 and φ_2, E_n being the energy of state n and

$$f_n = \frac{\sqrt{2\pi}}{n!} \left(\frac{n + 1/2}{\mathrm{e}}\right)^{n+1/2} \tag{2.38}$$

being a numerical factor. For the lowest lying state $n = 0$, the factor S_n is proportional to the gray area in Fig. 2.6. As this area gets smaller with decreasing Φ_{ext}, the escape rate Γ_0 increases, until the system escapes to the next deeper well. With continual change of Φ_{ext}, this behaviour will then repeat, resulting in regular well-jumps with a Φ_{ext} periodicity of Φ_0.
These jumps coincide with two important effects shown in Fig. 2.6 b) and c), namely jumps of the SQUID's eigenfrequency f_{SQUID} and jumps of the flux in the SQUID-loop Φ.
How Φ depends on Φ_{ext} can be understood as a consequence of the flux quantization condition in the SQUID loop, Eq. (2.21), and the current-phase relation of the Josephson junction, Eq. (2.11). The total flux in the SQUID loop is then the sum of the external flux Φ_{ext} plus the flux which the Junction's supercurrent I_s generates in the loop inductance L. The resulting equation

$$\Phi = \Phi_{ext} + LI_s = \Phi_{ext} - LI_c \sin\left(2\pi\Phi/\Phi_0\right) \tag{2.39}$$

is plotted in Fig. 2.6 b) for different values of β_L.
The f_{SQUID} behaviour in dependence of Φ_{ext} is caused by the variation of the shape of the active well. As the well gets flatter, f_{SQUID} decreases, until the system escapes into the next deeper well, which has a higher f_{SQUID}, resulting in regular dips and jumps with the same periodicity as the well-escapes.
Also indicated in Fig. 2.6 is that both of these effects are hysteretic, with the hysteresis depending on β_L.

2.3.4 3-junction Flux Qubit

Figure 2.7 a) shows the circuit diagram of a flux qubit. In the original three-junction design shown here, it functions similar to the RF-SQUID, with the difference

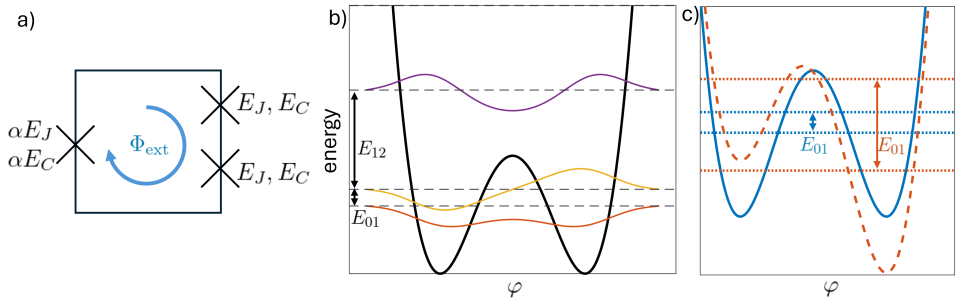

Figure 2.7: a) Circuit-diagram of a 3-JJ flux qubit. Two of the three junctions threading the loop are identical, with Joesphson energy E_J and capacitive Energy E_C while the third one is smaller by a factor of $0.5 < \alpha < 1$, resulting in the reduced energy scales αE_J and αE_C. The loop is threaded by an external flux Φ_{ext} b) Potential energy of the 3-JJ flux qubit at the half-flux point, where $\Phi_{ext} = \Phi_0/2$, with an $E_J/E_c = 100$ and $\alpha = 0.7$. The dashed lines indicate the qubit energy levels and the colored lines the corresponding eigenfunctions, both calculated numerically from the Hamiltonian. c) The potential energy of the same qubit for different values of Φ_{ext} ($\Phi_{ext} = 0.5\Phi_0, 0.49\Phi_0$ for the solid blue line and the dashed orange line, respectively). Φ_{ext} changes the potential tilt and thereby the qubit energy splitting E_{01}.

being that the large inductance is now contributed by two Josephson junctions with identical E_J and E_C instead of a linear inductance. The third junction has reduced size by a factor of α and thereby reduced energy scales αE_J and αE_C. In contrast to the circuits we've considered previously, the flux qubit has three superconducting islands, leading to a higher-dimensional Hamiltonian. The flux quantization condition links the superconducting phase differences across the junctions $\varphi_k, k = [1, 2, \alpha]$

$$\varphi_1 - \varphi_2 + \varphi_\alpha = \frac{2\pi\Phi_{ext}}{\Phi_0}, \tag{2.40}$$

leading to the two-dimensional potential energy

$$V = E_J \left(\cos\varphi_1 - \cos\varphi_2 - \alpha \cos\left(\frac{2\pi\Phi_{ext}}{\Phi_0} + \varphi_1 - \varphi_2 \right) \right). \tag{2.41}$$

To find a one-dimensional expression, we first transform the coordinates by introducing the phases $\varphi_p = (\varphi_1 + \varphi_2)/2$ and $\varphi_m = (\varphi_1 - \varphi_2)/2$, leading to the reduced Hamiltonian

$$\hat{H} = \frac{1}{2} E_{\text{C,p}} \hat{n}_{\text{p}}^2 + \frac{1}{2} E_{\text{C,m}} \hat{n}_{\text{m}}^2 + E_J(-2\cos(\varphi_p)\cos(\varphi_m) - \alpha\cos(\frac{2\pi\Phi_{\text{ext}}}{\Phi_0} + 2\varphi_m)), \tag{2.42}$$

where $E_{\text{C,p}} = 2e^2/C$ and $E_{\text{C,m}} = e^2/C(\alpha + 1/2)$ are the effective charging energies of the p-mode and m-mode respectively, and $\hat{n}_\sigma = -i\partial/\partial\varphi_\sigma, (\sigma = p, m)$ the

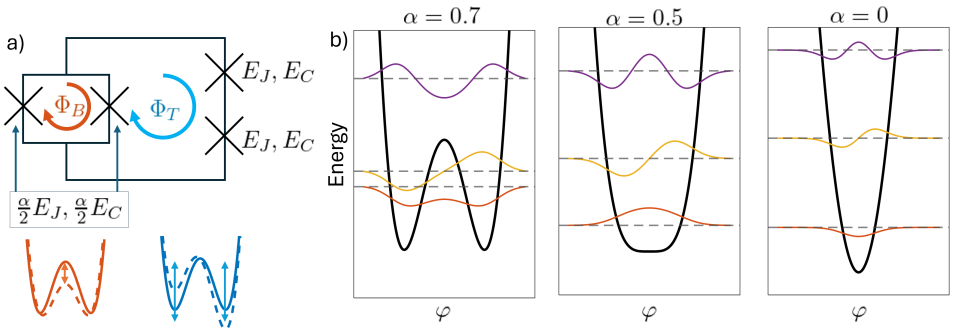

Figure 2.8: a) Circuit diagram of a fully tunable flux qubit, where the α-junction is replaced by a symmetric DC-SQUID. The two bias fluxes Φ_B and Φ_T control the potential barrier-height and tilt respectively as indicated by the colored potential sketches. b) Fully tunable flux qubit potentials at the half-flux point for $\alpha = 0.7, 0.5, 0$, respectively, with the dashed lines indicating the energy levels and the colored lines the corresponding eigenfunctions, calculated numerically for $E_J/E_C = 100$. Decreasing alpha leads to an increase in f_q and a decrease in the anharmonicity.

respective Cooper-pair number operators. In analogy to the Born-Oppenheimer approximation, we can omit the p-mode in cases where it oscillates much faster than the m-mode. The validity of this approach for the circuits fabricated in this work will be discussed in the next section. This gives us the 1-dimensional Hamiltonian

$$\hat{H} = \frac{1}{2}E_{C,m}\hat{n}_m^2 + E_J\left(-2\cos\varphi_m + \alpha\cos\left(\frac{2\pi\Phi_{\text{ext}}}{\Phi_0} + 2\varphi_m\right)\right). \tag{2.43}$$

In this form, the analogy to the RF-SQUID becomes apparent. Instead of the β_L-factor, here the α factor determines the potential shape. For $\alpha < 0.5$, the potential has one well, and multiple wells for $\alpha > 0.5$. A special case is $\alpha = 0.5$, which is used in so-called "quarton" qubits, which are named after the quartic term, which dominates the expansion of the potential.
Similar to the RF-SQUID, the potential can be manipulated by an external flux Φ_{ext}. Of special interest is the range around the half-flux point $\Phi_{\text{ext}} = 0.5\Phi_0$, where the potential is symmetric. This symmetric double-well configuration is used in so called "persistent current" qubit, which was the original idea for the flux qubit, where currents of opposite direction function as the computational states. This allows for a very intuitive picture, where the qubit states $|L\rangle$ and $|R\rangle$ represent the supercurrents of opposing directions associated with the left and right potential well, respectively. In the $\{|L\rangle, |R\rangle\}$-basis, the effective two-level Hamiltonian reads:

$$H = -\frac{\varepsilon}{2}\sigma_z - \frac{\Delta}{2}\sigma_x, \tag{2.44}$$

where $\varepsilon = 2I_p\left(\Phi_{\text{ext}} - \frac{\Phi_0}{2}\right)$ is the energy bias between the wells, tunable via the external flux, Δ is the tunneling amplitude between the wells, and σ_z and σ_x are the Pauli matrices in the $\{|L\rangle, |R\rangle\}$ basis.

Diagonalization of H gives the eigenenergies

$$E_\pm = \pm\frac{1}{2}\sqrt{\varepsilon^2 + \Delta^2}\,, \tag{2.45}$$

and the corresponding eigenstates are superpositions of the current states:

$$|\pm\rangle = \cos\frac{\theta}{2}\,|L\rangle \pm \sin\frac{\theta}{2}\,|R\rangle\,, \tag{2.46}$$

with the mixing angle

$$\tan\theta = \frac{\Delta}{\varepsilon}\,. \tag{2.47}$$

At the degeneracy point, $\varepsilon = 0$, the eigenstates are equal superpositions:

$$|\pm\rangle = \frac{1}{\sqrt{2}}\left(|L\rangle \pm |R\rangle\right)\,. \tag{2.48}$$

2.3.5 C-shunted Fully Tunable Flux Qubit

As motivated in the introduction, the circuits we developed in this work are fully tunable C-shunted flux qubits. They expand the design of the 3-JJ flux qubit introduced in the previous section by replacing the α-junction by a DC-SQUID and addition of a shunt capacitance C_{sh}. In a fully tunable flux qubit, we combine the ideas of the DC-SQUID with the 3-junction flux qubit, by replacing the α-junction by a DC-SQUID with both junctions having critical current smaller by the factor $\alpha/2$. Combining Eq. (2.26) and 2.43 leads to the 1-d Hamiltonian

$$\hat{H} = \frac{1}{2}E_{C,m}\hat{n}_m^2 + E_J\left(-2\cos\varphi_m + \alpha\cos\left(\frac{\pi\Phi_{\text{B}}}{\Phi_0}\right)\cos\left(\frac{2\pi\Phi_{\text{T}}}{\Phi_0} + 2\varphi_m\right)\right), \tag{2.49}$$

with $E_{C,m} = e^2/(C_{sh} + C/2 + \alpha C)$, where C is the intrinsic capacitance of one large junction. The flux Φ_B threading the α-SQUID, is now effectively tuning the α-factor of the qubit, allowing for *in situ* control of the potential shape as illustrated in Fig. 2.8 b).
As we will see in section 4, this control can be leveraged into a large ω_q tuning range, which is the key feature that makes this design attractive to be used for the study of defects.

2.3.6 Readout Resonator Coupling

The qubits discussed in this thesis are read-out using dispersive readout, which means the state of the qubit is detected by observing the resonance frequency of a readout resonator which is coupled to the qubit. Assuming a single mode of frequency f_q in the qubit and f_r in the resonator respectively, and a coupling strength g, a simple expression for the dispersive shift of the readout resonator can be derived from the Hamiltonian

$$H = \begin{pmatrix} f_q & g \\ g & f_r \end{pmatrix}. \tag{2.50}$$

The eigenvalues of this matrix are

$$\lambda_{\pm} = \frac{f_q + f_r}{2} \pm \sqrt{\left(\frac{f_q - f_r}{2}\right)^2 + g^2}, \tag{2.51}$$

which in the dispersive limit $g \ll \delta$, where $\delta = f_q - f_r$ is called the "detuning", approximates to

$$\begin{aligned} \lambda_+ &\approx f_r + \frac{g^2}{\delta} - \frac{g^4}{\delta^3} + \mathcal{O}(g^6) \\ \lambda_- &\approx f_q - \frac{g^2}{\delta} + \frac{g^4}{\delta^3} + \mathcal{O}(g^6) \end{aligned} \tag{2.52}$$

so the resonance frequency of both the qubit and the resonator are repulsed by a shift of $\approx \frac{g^2}{\delta}$, which is a common approximation in the literature.

2.4 Numerical Treatment of Hamiltonians

Important system properties, such as the energy eigenvalues, eigenstates, and their time development, can be extracted from the Hamiltonian operator. To this end it is often useful to diagonalize the Hamiltonian numerically, which we illustrate here at the example of a transmon qubit before generalizing to more complicated cases. According to Eq. (2.31), the Hamiltonian reads

$$\hat{H} = 4E_C\hat{n}^2 - E_J \cos\hat{\varphi}, \tag{2.53}$$

where $\hat{n}$ is the Cooper-pair number operator, $\hat{\varphi}$ is the superconducting phase difference, E_C is the charging energy and E_J the Josephson energy. We note the canonical relation $[\hat{\varphi}, \hat{n}] = i\hbar$.

To use numerical diagonalization methods, the Hamiltonian must be brought into a finite matrix representation. Here, we illustrate both the *charge basis* and *phase basis* representation.

Charge-basis Representation

Charge states $|n\rangle$ are the eigenstates of the Cooper-pair number operator, $\hat{n}|n\rangle = n|n\rangle$, trivially diagonalizing the $4E_C\hat{n}^2$ term. We treat the potential term by using the identity

$$\cos\hat{\varphi} = \frac{1}{2}\left(e^{i\hat{\varphi}} + e^{-i\hat{\varphi}}\right),$$

and $e^{\pm i\hat{\varphi}}|n\rangle = |n \pm 1\rangle$, which follows from the canonical relation between $\hat{\varphi}$ and $\hat{n}$, analogous to how the translation operator is related to the momentum operator. It follows that the Hamiltonian matrix elements in the charge basis are

$$\langle n|\hat{H}|m\rangle = 4E_C n^2\delta_{n,m} - \frac{E_J}{2}\left(\delta_{n,m+1} + \delta_{n,m-1}\right), \tag{2.54}$$

with $n, m \in \mathbb{Z}$ and the Kronecker delta $\delta_{n,m}$. To limit this matrix to finite dimensions, one has to truncate the allowed space for n and m. For example, limiting $n, m \in \{-1, 0, 1\}$ leads to the matrix representation

$$\hat{H} = \begin{pmatrix} 4E_C & -\frac{E_J}{2} & 0 \\ -\frac{E_J}{2} & 0 & -\frac{E_J}{2} \\ 0 & -\frac{E_J}{2} & 4E_C \end{pmatrix}.$$

The eigenvalues of this matrix will then be the energy eigenvalues of the system, with the corresponding eigenvectors in charge space representation, and can be found with numerical solving algorithms. In this work, we used MatLab. The larger the chosen truncated space is, the more accurate this representation becomes, at the cost of higher computational complexity. Best practice is to increase the space until the results stop changing significantly. In this work, $n, m \in \{-15, 15\}$ has usually fulfilled this condition.

Phase-basis Representation

In the phase basis, wave functions are expressed as $\psi(\varphi) = \langle\varphi|\psi\rangle$, where $\varphi \in [0, 2\pi)$ reflects the 2π-periodicity of the superconducting phase. Since φ is a continuous variable, a common approach is to discretize it on a finite periodic grid $\{\varphi_j\}$, with

$j = 0, ..., N-1$, $\varphi_j = j\Delta\varphi$, and $\Delta\varphi = 2\pi/N$. In this basis, the potential term of the Hamiltonian diagonalizes trivially to

$$\langle\varphi_j| - E_J \cos\hat{\varphi}\,|\varphi_k\rangle = -E_J \cos(\varphi_j)\delta_{j,k}. \tag{2.55}$$

To treat the $4E_C\hat{n}^2$ term, we use the canonical relation $\hat{n} = -i\partial/\partial\hat{\varphi}$, and approximate the differential with a finite differential quotient

$$\frac{\partial^2\psi(\varphi_j)}{\partial\varphi^2} \approx \frac{\psi(\varphi_{j+1}) - 2\psi(\varphi_j) + \psi(\varphi_{j-1})}{(\Delta\varphi)^2}, \tag{2.56}$$

leading to the matrix element

$$\langle\varphi_j|\,4E_C\hat{n}^2\,|\varphi_k\rangle = \frac{4E_C}{(\Delta\varphi)^2}(2\delta_{j,k} - \delta_{j,k+1} - \delta_{j,k-1}). \tag{2.57}$$

A finer discretization, i.e. a higher N, leads to more accurate results. For an optimal value, N should be increased until results stop changing significantly.

2.5 Energy Relaxation

A central property of any quantum system is the time scale on which its state dissipates. The relaxation time $T_1$is a measurement of the time over which a system decays to its ground state due to energy relaxation processes. It is defined as the time constant governing the exponential decay of the excited state population

$$P_e(t) = P_e(0)\,e^{-t/T_1},$$

where $P_e(t)$ is the probability of finding the system in the excited state at time t. The relaxation rate $\Gamma_1 = 1/T_1$ is defined as the inverse of T_1, with both depending on the dissipative channels to which a system is coupled. In the case of superconducting qubits, the most important relaxation channels include loss into the readout resonator in form of the Purcell effect, dielectric losses caused by microscopic defects, relaxation due to quasiparticle tunneling and bias line noise. The total relaxation rate is then the sum over the relaxation rates of each channel:

$$1/T_1 = \Gamma_1 = \Gamma_{\text{Purcell}} + \Gamma_{\text{TLS}} + \Gamma_{\text{qp}} + \Gamma_{\text{noise}} \tag{2.58}$$

2.5.1 Loss Via General Noise Channels

Charge and flux noise limiting a qubit's T_1time can reach the qubit via flux bias lines, charge gates and intrinsic microscopic degrees of freedom in the sample

material. A general approach to calculate the T_1limitations from these sources can be derived using Fermi's Golden Rule, which is used for calculating the transition rate between quantum states due to a weak perturbation. For a system with Hamiltonian $\hat{H}$ and a general noise parameter λ, the relaxation caused by the noise is given by [45]

$$\Gamma_\lambda = \frac{1}{\hbar^2} \left| \left\langle 1 \left| \frac{\partial \hat{H}}{\partial \lambda} \right| 0 \right\rangle \right|^2 S_\lambda(\omega_q), \tag{2.59}$$

where $S_\lambda(\omega_q)$ is the spectral density of the noise evaluated at the qubit frequency. This equation often has to be re-expressed in terms of the noise spectral density at the noise source mediated by the mechanism by which it couples into the qubit. For example, a flux-sensitive qubit can be affected by a noisy current source, when the current induces flux Φ via a mutual inductance M. The current-noise induced relaxation is then

$$\Gamma_I = \frac{1}{\hbar^2} \left| \left\langle 1 \left| \frac{\partial \hat{H}}{\partial \Phi} \right| 0 \right\rangle \right|^2 M^2 S_I(\omega_q), \tag{2.60}$$

where S_I is the spectral density of the current noise.

2.5.2 Purcell Loss

The Purcell effect describes the change of the spontaneous emission of a system, when placed inside a cavity [46], and represents an important loss channel for qubits when they are coupled to a readout resonator. Even if the resonator is detuned from the qubit frequency, the qubit can still emit energy into the resonator mode and decay to its ground state. This spontaneous emission channel, first described by E. M. Purcell, limits the qubit relaxation time T_1. The presence of the resonator modifies the electromagnetic density of states available to the qubit, enhancing spontaneous emission at the qubit transition frequency. Using Fermi's golden rule, this limit can be estimated to be [44]

$$\frac{1}{T_1^{\text{Purcell}}} = \kappa \frac{g^2}{\Delta^2}, \tag{2.61}$$

where g is the coupling strength between the qubit and the resonator, $\kappa = \omega_r / Q_r$ is the resonator loss rate, with ω_r the resonator frequency and Q_r its quality factor, and $\Delta = \omega_q - \omega_r$ is the detuning between the qubit frequency ω_q and the resonator frequency ω_r.

2.5.3 Vacuum Radiation Loss

The qubit can also spontaneously emit energy into the vacuum. An intuitive picture for this effect can be attained by viewing the qubit as an electric dipole, which emits the average power

$$P = \frac{1}{4\pi\varepsilon_0}\frac{d^2\omega^4}{3c^3} \tag{2.62}$$

into the vacuum, where d is the dipole moment, ω the oscillation frequency, ε_0 is the vacuum permittivity and c is the speed of light in vacuum. For a qubit transition with frequency ω_q and an effective electric dipole moment d, the spontaneous emission rate into the vacuum can be described as[44]

$$\frac{1}{T_1^{\text{vac}}} = \frac{P}{\hbar\omega_q} = \frac{\omega_q^3 d^2}{12\pi\varepsilon_0\hbar c^3}. \tag{2.63}$$

We note that the emission rate grows rapidly with frequency ($\propto \omega_{ge}^3$) and with the square of the dipole moment. In superconducting qubits, radiative loss to the vacuum is typically negligible compared to Purcell loss or dielectric loss, due to the strong electromagnetic confinement of on-chip structures. However, in devices with high operating frequencies or significant dipole coupling to free space, such as qubits with large antennas or weak electromagnetic shielding, this mechanism can become dominant.

2.5.4 Quasiparticle-induced Loss

Quasiparticles, which are non-equilibrium excitations of the superconducting condensate, are another cause of energy relaxation in superconducting qubits. In general, the decay rate caused by quasiparticles is given by [47]

$$\Gamma_{qp} = |\langle 0|\sin\frac{\hat{\phi}}{2}|1\rangle|^2 S_{qp}(\omega_q), \tag{2.64}$$

where $S_{qp}(\omega_q)$ is the quasiparticle spectral density evaluated at the qubit frequency. The matrix element $|\langle 0|\sin\frac{\hat{\phi}}{2}|1\rangle|^2$ depends on the qubit type and parameters via the wave functions $|0\rangle$ and $|1\rangle$ and can be evaluated numerically with the methods introduced in section 2.4.

2.5.5 TLS-induced loss

Last, but not least, the energy relaxation of a qubit is limited by the presence of TLS residing in the circuit dielectrics, i.e. the substrate, the tunnel barriers in the junctions and the surface oxide layers. Strongly coupled TLS can coherently exchange energy with the qubit, causing a loss in T_1 and dispersively shift the qubit's resonance frequency, analogous to the shift caused by the readout resonator, see sec. 2.3.6. The relaxation rate induced by a strongly coupled TLS is given by [48]

$$\Gamma_{\mathrm{TLS}} = \frac{2g^2\Gamma}{\Gamma^2 + \Delta^2}, \tag{2.65}$$

where Δ is the detuning between qubit and TLS, g is the TLS-qubit coupling strength and $\Gamma = \Gamma_1^{\mathrm{TLS}}/2 + \Gamma_\phi^{\mathrm{TLS}} + \Gamma_1^{\mathrm{Q}}/2 + \Gamma_\phi^{\mathrm{Q}}$. The rates Γ_1^{TLS} and Γ_1^{Q} are the relaxation rates of the TLS and the qubit respectively, when the systems are far detuned, and $\Gamma_\phi^{\mathrm{TLS}}$ and Γ_ϕ^{Q} are their respective pure dephasing rates. This expression is valid when $\Gamma_1^{\mathrm{TLS}} > g > \Gamma_1^{\mathrm{Q}}$, and is closely linked to the TLS detection sensitivity of the qubit, which will be detailed in sec. 3.5.

Additionally to the effects of strongly coupled TLS, the presence of a bath of weakly coupled TLS also affects the energy relaxation of a qubit, an effect which is also called dielectric loss. Each interface contributes a relaxation rate proportional to its *participation ratio*, which is the fraction of the qubit's total energy that is contained in the respective component. The dielectric relaxation rate can therefore be expressed by[49]

$$\Gamma_{\mathrm{diel}} = \omega_q \sum_i \frac{p_i}{Q_i}, \tag{2.66}$$

where i sums over all components, with p_i being the component's respective participation ratio and Q_i being its internal quality factor. The denser the TLS bath is and the stronger the TLS couple to the environmental electric fields and phonons, the lower the internal quality factor of a material becomes. According to the STM, the internal quality factors driven by electrically and phononically interacting TLS in component i are given by [50]

$$\frac{1}{Q_{i,\mathrm{el}}} = \frac{\pi |\boldsymbol{p}|^2 D_0}{3\epsilon_i}, \text{and} \frac{1}{Q_{i,\mathrm{ph}}} = \frac{\pi |\gamma|^2 D_0}{2\rho v^2} \tag{2.67}$$

respectively, where D_0 is the TLS' DoS, ϵ_i the component's permittivity, ρ its density, v the sound velocity and $\boldsymbol{p}$ and γ the electric and elastic dipole moments of the TLS, respectively.

3 Experimental Methods

3.1 Sample Fabrication

Here, we describe the fabrication process of the fluxmon qubits and C-shunted flux-qubits, while the fabrication of the mergemon qubits used in chapter 5 is detailed in [51]. While different sample designs are used in this work, the fabrication processes are identical, with exception of the geometry of the patterned structures, of course.

Wafer Preparation

In this step, the sample substrate is processed from a 3 inch diameter sapphire wafer of 500 µm thickness, which is cleaned with a piranha acid. After heating for 2 hours at 200°C, a 100 nm thick Al ground plane is deposited with a *PLASYS MEB 550 S* and passivated via static oxidation for ten minutes in a 30 mbar pure oxygen environment. From this wafer, nine 2x2 cm² dies are cut for further processing. From each of these dies, six 6x6 mm samples will be cut after the circuit structures

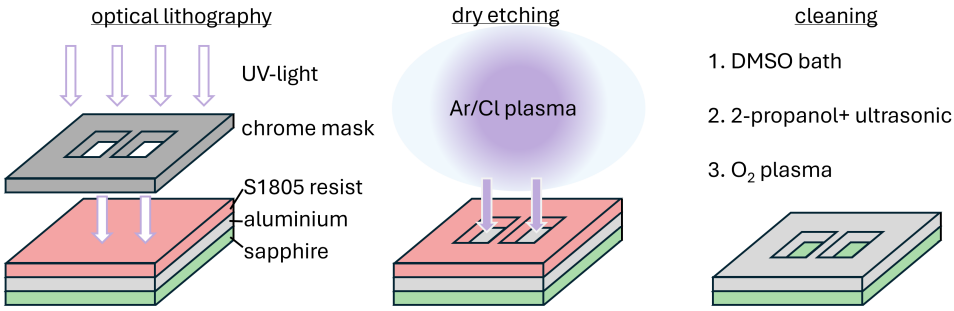

Figure 3.1: Schematic of the dry-etching process used to define structures with a resolution >2µm. Symbolically depicted as two rectangular holes, the structures are transferred from a hard-mask to a positive resist, via UV-light exposure and subsequent development (not shown). Then, they are etched into the sample aluminium via Ar/Cl plasma etching. Finally, the optical resist is removed thoroughly.

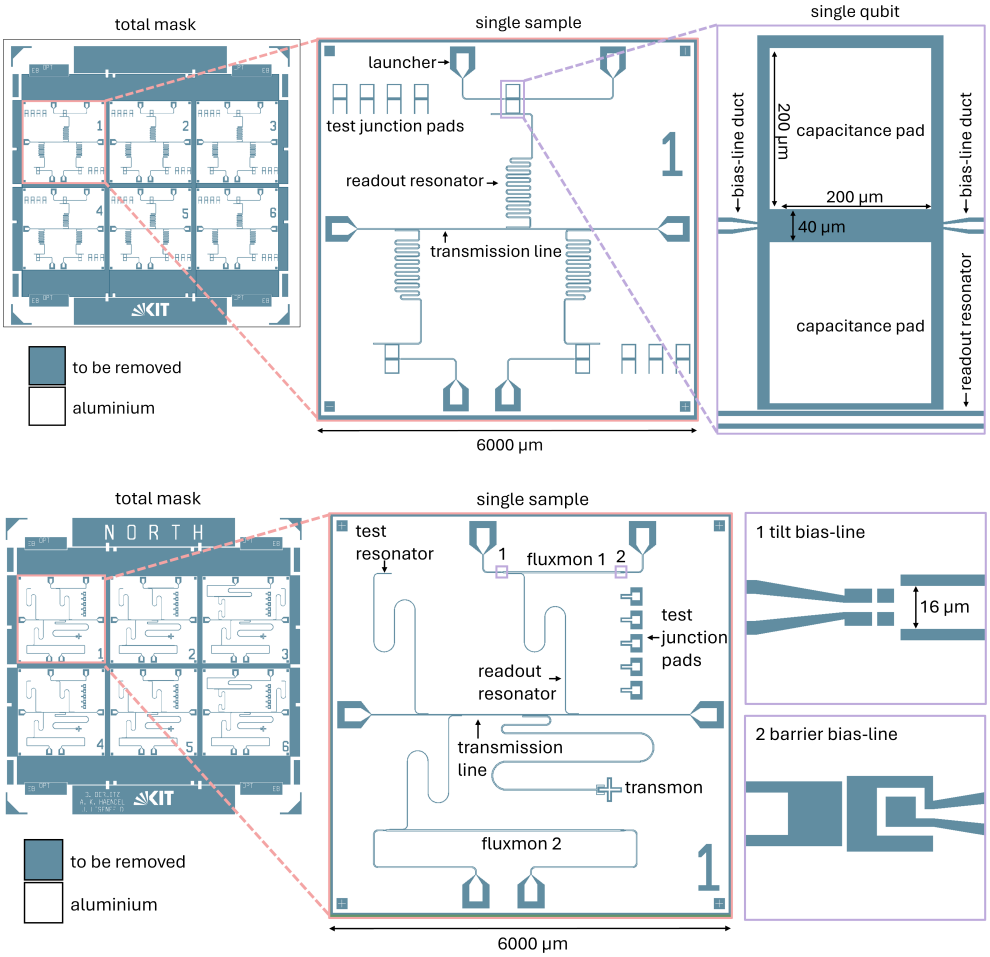

Figure 3.2: Patterns of the hard masks used for the optical lithography step. Six 6x6cm^2 samples are patterned on one die. Top: pattern for C-shunted flux qubits with a zoom-in on a single sample and a subsequent zoom-in on a single qubit. Bottom: Pattern for Fluxmon qubits with a zoom-in on a single sample and subsequent zoom-ins on the flux bias lines.

are fully processed as described in the following two sections.

Optical Lithography and Dry Etching

Fig. 3.1 shows how larger structures (resolution >2µm), such as transmission lines, resonators and capacitors are patterned. The desired patterns are defined

using *S1805* photoresist and a hard mask in a *Carl Suess MA6* maskaligner, and subsequently dry-etched into the ground plane using an argon-chlorine plasma, in an inductively coupled plasma etcher of the type *Oxford Plasmalab 100 ICP180*. The hard-mask patterns for the C-shunted flux qubits and the fluxmon qubits are shown in Fig. 3.2.

E-Beam Lithography and Lift-off

Figure 3.3 illustrates the Al-AlOx-Al tri-layer deposition, using an $in-situ$ bandaged Niemeyer-Dolan technique, which is used to create structures with a resolution of a few nm. To create an undercut for a clean lift-off, the sample is covered with a bilayer resist stack of 250 nm *A4* (PMMA) on top of 900 nm *El-13* (MMA), which is subsequently exposed with a *JEOL JBX-5500ZD* electron beam writing system, and developed using a mixture of 2-propanol and bi-distilled water.
This creates trenches and bridges for the Niemeyer-Dolan deposition. To create junctions of the desired critical current, the exact geometry and e-beam dosage has to be carefully fine-tuned (see e.g. [16] for details).
Figure 3.3 b) details the subsequent deposition process, which is executed in a vacuum inside the plasma deposition system. First, the bottom electrode is deposited at angle 1. Then the tunnel barrier is formed via controlled oxidation. Then the top electrode is deposited at angle 2. This forms the Josephson junction.
After removing unwanted oxide layers, a third Al layer is deposited at an angle perpendicular to the ground plane. This bandage layer serves to avoid stray junctions, and in case of the fully tunable flux qubits, to connect the junction loops to the plate capacitors. This method was developed for transmon qubits by Bilmes *et al.* [52].
We note that here this method was adapted to create the large junctions necessary for flux qubits. Consequently, the first layer is deposited at a very steep angle (> 60), which overshoots the dolan bridge. This makes it necessary to make the trench a bit wider on the side of the second electrode, to prevent shorting the junction at the sides of the trench, which is further explored in section 6.1. It is furthermore vital that the second electrode ends under the dolan bridge, otherwise the junction will be shorted in the bandaging step.
In the case of the C-shunted flux qubits, four Junctions, as well as two local flux bias lines are defined in this step and connected to the rest of the circuit in the bandaging step, which is illustrated in Fig. 3.4.

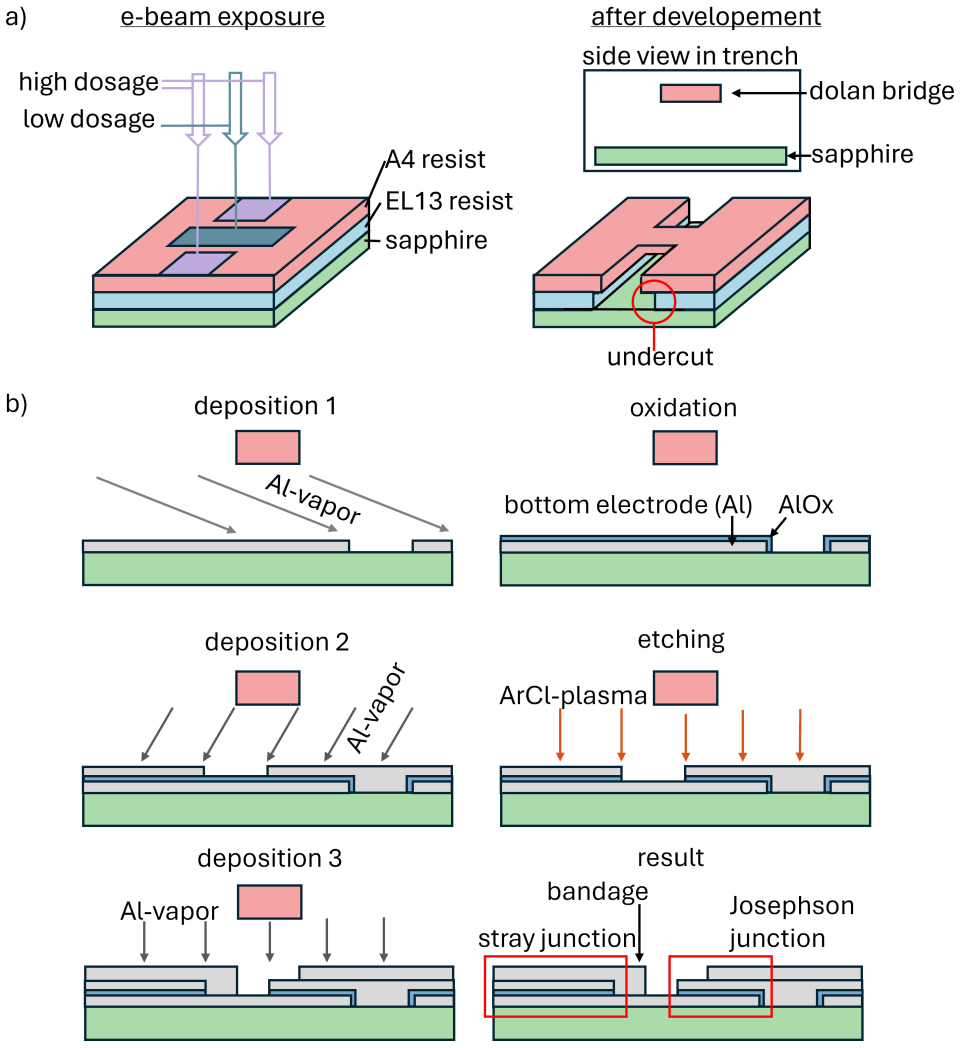

Figure 3.3: Fabrication of Josephson junctions. a) Different electron-beam dosages define trenches and bridges in an MMA-PMMA resist stack. A clean undercut allows for later lift-off of unwanted deposited metal. b) Schematic of the 3-angle shadow-evaporation process used to form the junction in the previously defined trench.

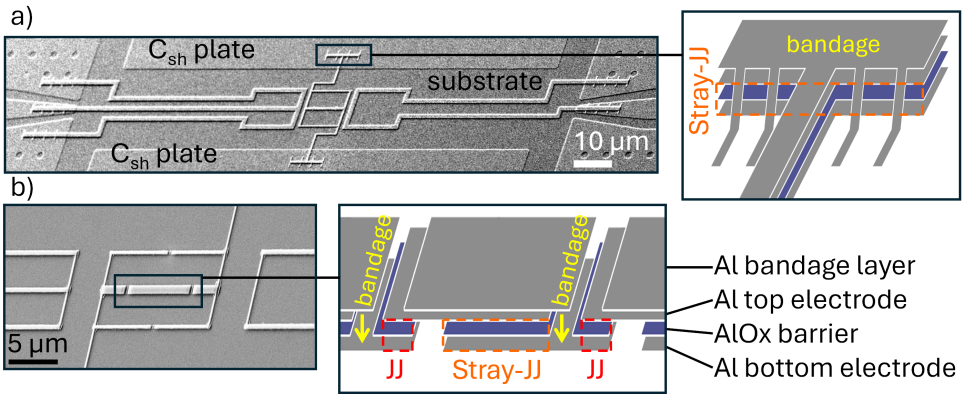

Figure 3.4: a),b): SEM-images of samples A and B respectively, showing the bias line and circuit layout. Inlays illustrate how an in-situ deposited bandage layer is used to avoid stray-junctions and contact the junction-circuit to the coplanar shunt-capacitor.

3.2 Cryogenic Setup

Figure 3.5 shows a schematic of the attenuation and filtering setup used to minimize thermal noise and environmental radiation reaching the sample, which is located at the base stage of a dilution refrigerator (T≈25 mK). This cooling way below the critical temperature of aluminium (1.2 K) is necessary to suppress thermal excitation of the qubit. The probability of finding a qubit in the excited state at temperature T is given by

$$p_e(T) = \frac{1}{1 + e^{hf_q/k_B T}}, \tag{3.1}$$

which for a qubit of $f_q = 3$ GHz is negligible at T=25 mK ($p_e \approx 0.3\%$), but becomes significant ($p_e \approx 20\%$) at T=100 mK.
On the input line, we apply a total of 60 dB of attenuation, divided across the 4-K, still, and mixing chamber (M/C) stages. This staged attenuation thermalizes incoming signals and suppresses room-temperature Johnson-Nyquist noise. For a cascaded attenuation chain thermalized at N temperature stages i, with power attenuation factors $a_i > 1$ and corresponding stage temperatures T_i, the effective noise temperature at the device input is given by

$$T_n^{\text{eff}} = T_1 + \sum_{i=1}^{N-1} \frac{T_{i+1}}{\prod_{j=1}^{i} a_j}. \tag{3.2}$$

This expression shows that each attenuator itself contributes thermal noise weighted by all subsequent attenuation. We note that the amount of attenuation that can be

thermalized at a stage is limited by the stages cooling power, which prevents us from trivially installing all attenuation at the coldest stage. For our input-line we expect $T_n^{\text{eff}} \approx 26\,\text{mK}$.
Additional low-pass and band-pass filters (LPF and BPF, respectively) are placed at the base stage to reject out-of-band noise and suppress higher harmonics.
On the output side, the signal passes through a pair of circulators and a HEMT amplifier at the 4-K stage, followed by further amplification at room temperature. The circulators prevent amplifier noise from reaching the qubit.
The local qubit flux lines are controlled via pulses generated by an arbitrary waveguide generator (AWG). On these lines, lower attenuation and 1 GHz bandwidth filtering enable the fast and wide qubit flux-pulses necessary for qubit swap-spectroscopy, while preventing noise at the qubit frequency from reaching the sample.
We note that high attenuation limits the amount of current that can be supported by a given line without heating the cryostat, which in turn limits the accessible bias-flux range. Here, we have chosen to err on the side of maximum reach, at the detriment of higher bias line noise. This makes filtering of noise at the qubit frequency crucial in these lines to prevent excessive thermal excitation.

3.3 Sample Housing and Bond Wires

A well-designed sampleholder is at the heart of microwave experiments with superconducting qubits. It serves as a lead for currents, microwave pulses and fields we want to apply to our sample, while providing good thermalization and minimal coherence mismatch. Figure 3.6 shows a sampleholder designed specifically for TLS spectroscopy. The sample is held with four screws which serve both as thermalization pillars and provide counter-force to a piezo-element which is used to exert pressure to the sample from the bottom. An acrylic ball prevents harmful shearing forces in the Piezo-element and decouples it thermally and electrically from the sample.
Figure 3.6 a) shows the sample sitting in the center of a 1 mm thick silicone-copper PCB (printed circuit board) with six coplanar waveguide leads. The leads' 50 Ω impedance is important to carry microwaves and fast pulses to the sample without unwanted reflections.
25 µm diameter aluminium bond wires are placed to connect the leads to the corresponding launchers on the sample. To keep impedance mismatch to a minimum, wires are also placed to the sides of each launcher, closely following the narrowing of the wider PCB leads to the narrower on-sample launchers.

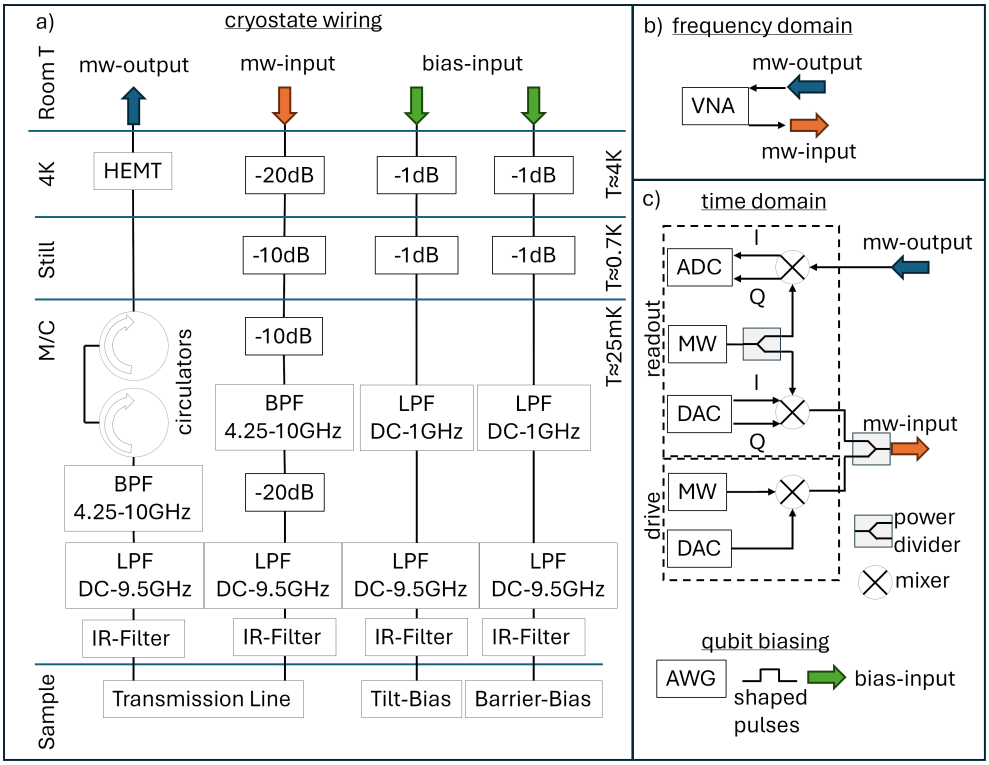

Figure 3.5: Wiring setup for fully tunable flux qubits. a) Setup inside the cryostat. b) Room temperature setup for frequency domain measurements. c) Room temperature setup for time domain measurements. Legend: BPF=band-pass filter, LPF=low-pass filter, IR-Filter=infrared filter, MW=microwave source, AWG=arbitrary waveguide generator, HEMT=high mobility electron transistor, ADC= analogue to digital converter, VNA=vector network analyzer.

Additional wirebonds connect the on-sample ground-plane to the PCB ground-plane, which in turn is connected to the copper main body of the sample-box. This ensures a balanced global electrical ground and provides additional sample thermalization. Further balancing of the on-sample ground plane is achieved by placing "air bridge" style wirebonds to bridge structures that would otherwise subdivide the ground-plane. The right inset of Fig. 3.6 b) shows schematic examples of placed bonds.
One finding of this work is that these wirebonds can sometimes form unwanted RF-SQUIDs, which is detailed in chapter 5. This underlines the importance of careful experimental setup design, as the boundary between sample and housing is especially transparent in quantum physics.

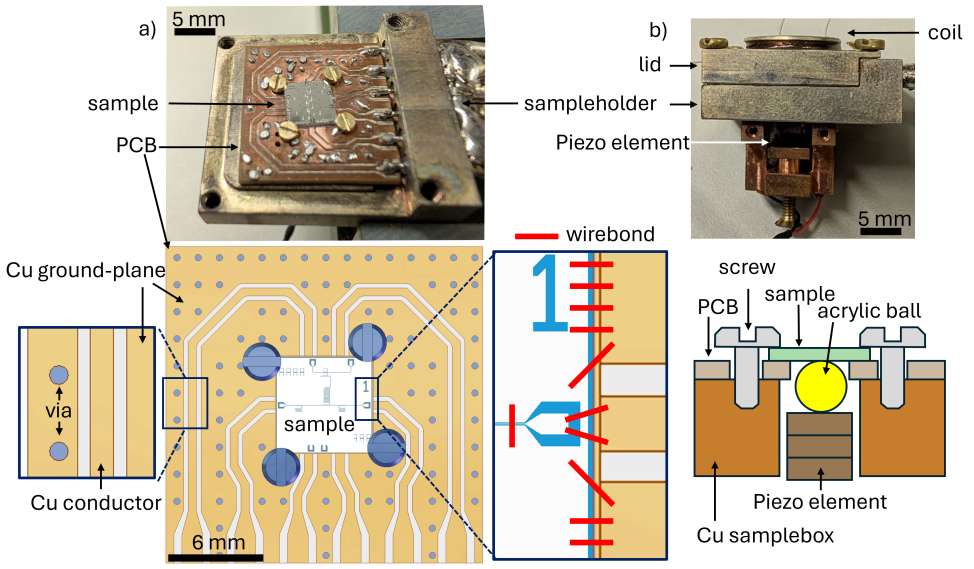

Figure 3.6: Sampleholder for TLS spectroscopy. a) Top: Photograph of a sampleholder consisting of a silver-plated copper body and a silicone-copper PCB. A sample is fixed to its center by screws. Bottom: Schematic of the PCB with zooms showcasing the CPW leads, examples of wirebonds and tin vias connecting its ground plane to the sampleholder body. b) Top: sideview of the sampleholder with attached lid. Bottom: cross-section schematic of how the Piezo actuator connects to the sample via an acrylic ball.

3.4 Microwave Measurements of Qubits

Microwave techniques provide the primary interface for both controlling and measuring superconducting qubits. In the frequency domain, continuous-wave spectroscopy reveals the qubit transition frequencies and dispersive shifts through resonator response. In the time domain, shaped microwave pulses prepare and manipulate qubit states, while dedicated readout tones probe the state-dependent response of the coupled resonator. Here, we review how these techniques can be used to characterize a qubit sample, and understand its electromagnetic environment.

3.4.1 Frequency Domain

In frequency domain measurements, we sweep the qubit bias fluxes, while measuring the frequency-dependent transmission coefficients through the transmission line using a VNA (vector network analyzer), whose port 1 and 2 are connected to

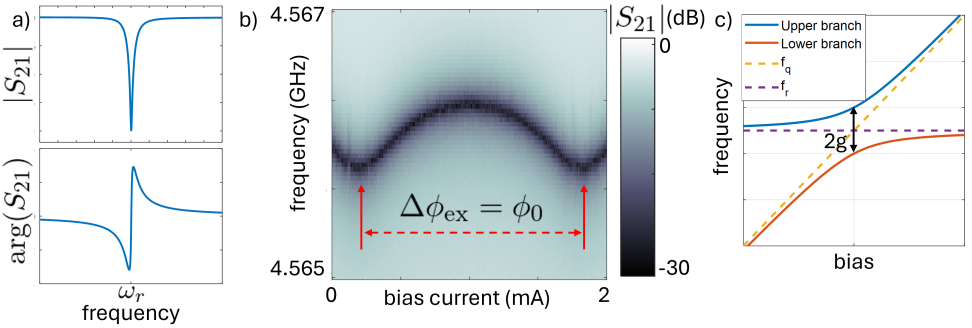

Figure 3.7: Frequency-domain characterization of a qubit-resonator system. a) Transmission magnitude $|S_{21}|$ and phase of the readout resonator measured with a vector network analyzer (VNA), showing the characteristic resonance dip and phase jump (illustration). b) Two-dimensional scan of $|S_{21}|$ as a function of probe frequency and bias current applied to the qubit. The black line is the resonator's resonance dip and shows a Φ_0-periodicity with Φ_{ex}. c) Schematic illustration of the avoided crossing between the qubit and resonator modes. The splitting $2g$ corresponds to the qubit-resonator coupling strength.

the input and output line of the setup, respectively. The readout resonator appears as a dip in the amplitude of the transmitted signal and a jump in the transmitted phase (see Fig. 3.7). Since the frequency at which these signals appear depends on the bias-fluxes in the qubit, these traces allow us to map the qubit bias-fluxes to the applied biasing currents. As VNA frequency scans are much faster than time domain measurements, these scans are practical for qubit bring-up and allow for bias line calibration and characterization of the readout resonator and the qubit-resonator coupling strength.
For a transmon qubit, we sweep the external flux by applying a magnetic field with a lid-coil or a local bias line. This tunes the qubit frequency f_q, which in turn tunes the readout-resonator frequency f_r, according to Eq. (5.1). An example of such a scan is shown in Fig. 3.7, which allows identification of the bias current of the highest and lowest qubit frequency, and thereby calibration of the bias line or lid-coil.
If the qubit frequency crosses the resonator's undressed resonance frequency, an avoided level crossing can be observed as shown in Fig. 3.7. As a result of Eq. (5.1), the width of the crossing is $2g$, where g is the qubit-resonator coupling strength.

In the case of a fully tunable flux qubit, two bias lines are involved, making a scan of the full resonator response to the bias-fluxes cumbersome. A more convenient measurement can be found in e.g. [53], where it was nicknamed "fireball"-scan. In these scans we only observe the transmission at a single probe-frequency while sweeping both bias lines, and infer the resonator's resonance frequency from the

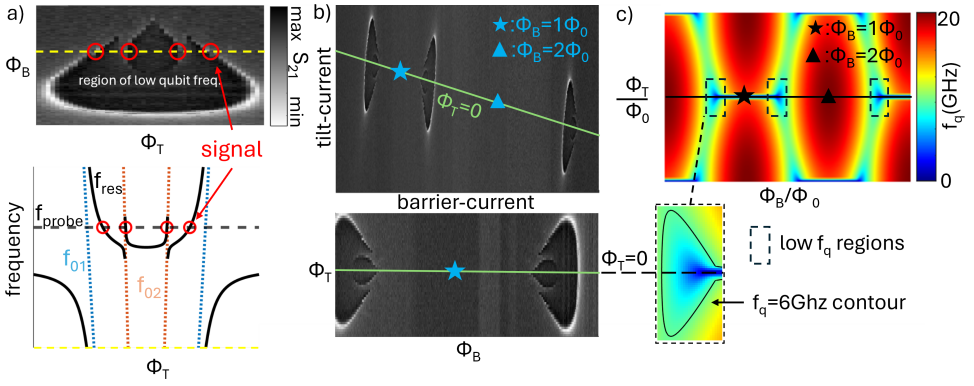

Figure 3.8: "Fireball" scan characterization of a fully tunable flux qubit. a) principle of a Φ_T-Φ_B-sweep calibration measurement. A signal (red circles) is detected, when f_{res} is shifted into resonance with f_{probe} by a qubit transition. b) Calibration measurements used to identify symmetry points in the Φ_T-Φ_B-landscape and the bias line cross-talk (corrected in the bottom measurement). c) Numerical calculation of the qubit resonance frequency f_{q}, revealing the characteristic tear-shaped areas where f_{q} is lowest.

results.
Figure 3.8 a) illustrates the principle. The transmitted signal (S_{21}) is minimal when the readout resonator resonance f_{res} equals the probe frequency (red circles). Since f_{res} depends on the qubit resonance frequency, this minimum indicates that the qubit was tuned to a certain frequency which depends on the chosen f_{probe}.
An example measurement is shown in Fig. 3.8 b), where the inside of the tear-shaped region thus corresponds to flux bias combinations where the qubit has lowest resonance frequencies. Comparing these characteristic shapes to a numerical calculation map of the qubit frequency as shown in Fig. 3.8 c), allows one to map the applied bias currents I_B and I_T to the induced bias fluxes Φ_B and Φ_T.
Due to crosstalk of the flux bias lines, the uncalibrated measurement (top panel in Fig. 3.8 b) is skewed. The lower panel shows the same measurement when the crosstalk is compensated by balancing the flux bias currents. Along the green line in the panels, the qubit potential has zero tilt $\Phi_T = 0$. Points of lowest and highest qubit frequency along this line are indicated by a star and triangle as in Fig. 3.8 c).

3.4.2 Time Domain

In time domain measurements, sequences of EM-pulses are used to probe time-dependent qubit properties, such as energy relaxation and phase coherence. Microwave pulses sent via the transmission line are used to excite the qubit population

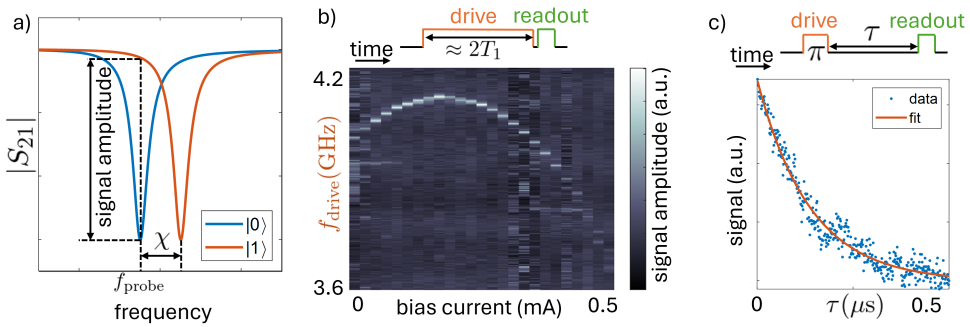

Figure 3.9: Example time-domain measurement of a superconducting qubit. a) Illustration of readout of the qubit state by observing the qubit-state dependent dispersive shift of the readout resonator via the signal shift it induces in $|S_{21}|$. b) Pulse sequence (top) and example measurement (bottom) for a qubit spectroscopy. A long microwave drive pulse excites the qubit to equilibrium ($P(e) \approx 0.5$), followed by a readout pulse probing the resonator response. c) Pulse sequence (top) and example decay (bottom) of the measured signal after a π-pulse as a function of the delay time τ. The qubit energy relaxation time T_1 can be extracted via an exponential fit.

and probe the state of the readout resonator, while DC-pulses in the qubit control lines are used to quickly manipulate the qubit potential energy. In the protocols presented here, these measurements are then averaged over ca. a thousand repetitions which allows us to ascertain the statistical probability of each possible outcome.

Qubit Spectroscopy

Figure 3.9 a) shows a pulse sequence used to identify the qubit resonance frequency. The first microwave pulse excites the qubit and the second pulse probes the resonance frequency of the readout resonator. The length of the excitation pulse should be chosen about twice the expected qubit T_1 time, to prevent coherent oscillations of the qubit excitation from interfering with the spectroscopy (see next section). If the excitation pulse is on resonance with the qubit, the resonator will be shifted out of resonance, and a higher transmission amplitude will be detected. Thus, repeating this sequence while sweeping the excitation pulse frequency reveals the qubit resonance frequency as a peak, as shown in Fig. 3.9 b). Figure 3.9 c) shows how repeating this sequence at different qubit bias points results in a qubit spectroscopy. Qubit parameters, such as E_C and E_J, can be extracted from the spectroscopy, by fitting of the appropriate Hamiltonian (see section 2).

Rabi Oscillations

Driving Rabi oscillations serves as a basic demonstration of coherent quantum control, and allows for pulse calibration for subsequent experiments. In this protocol, a continuous-wave microwave pulse of fixed frequency $\omega_d = \omega_q$ is applied to the qubit with variable pulse duration τ, see Fig. 3.10. After the pulse, the qubit state is immediately measured. Repeating the sequence for different τ-durations allows one to map out the qubit excitation probability $P_e(\tau)$, revealing coherent oscillations between the $|0\rangle$ and $|1\rangle$ states, described by the expression

$$P_e(\tau) = \frac{1}{2} - \cos(\Omega_R \tau) e^{-\tau/T_R}. \tag{3.3}$$

. These oscillations arise from the resonant drive inducing rotations on the Bloch sphere with a *Rabi frequency* Ω_R, which depends on the amplitude of the drive pulse. Experimentally, the drive amplitude is controlled by adjusting the microwave source power delivered to the qubit input line. As the drive power increases, Ω_R increases accordingly, resulting in faster oscillations. These oscillations are damped and decay exponentially over the Rabi damping time T_R, which is caused by phase decoherence of the qubit.
From the observed oscillation, we extract the amplitude-dependent π-pulse length $\tau_\pi = \pi/\Omega_R$, which is the pulse length required to invert the qubit population, i.e. to excite the qubit from the ground state. In practice, chosing a microwave power so that τ_π is in the 100 - 250 ns range has been proven practical.

T_1 Measurement

The energy relaxation time T_1 is an important benchmark for the performance of a quantum circuit, as explored in section 2.5. Figure 3.9 c) shows an example measurement and the pulse sequence. After letting the qubit decay to the ground state, it is excited with a π-pulse (see previous section) after which it is left to decay for a time τ. Then, the qubit state is measured. Repeating this measurement for different τ values, allows one to observe the exponential decay of the qubit excitation probability

$$P_e(\tau) = P_e(0) e^{-\tau/T_1}. \tag{3.4}$$

From this the T_1 time can be extracted via an exponential fit. Sometimes, the decay will have a beating which indicates that the qubit is coherently exchanging energy with another system. If it is a TLS-defect it can be tuned out of resonance with the qubit by an electric field or mechanical strain.

Ramsey Fringes

While the energy relaxation time T_1 characterizes the decay of population from the excited state to the ground state due to energy dissipation into the environment, the Ramsey experiment probes the loss of phase coherence between the qubit eigenstates, yielding the dephasing time T_2^*. In this protocol, a $\pi/2$-pulse (half a π-pulse) rotates the qubit state from the ground state $|0\rangle$ onto the equator of the Bloch sphere, preparing a coherent superposition state $(|0\rangle + |1\rangle)/\sqrt{2}$. The qubit is then left to freely evolve for a variable delay time τ without any applied drive, during which the state precedes around the z-axis. After the free evolution period, a second $\pi/2$-pulse is applied, converting the accumulated phase into a measurable population difference. By recording the excited state probability $P_e(\tau)$ as a function of the delay time τ, which are modulated by a decay envelope due to dephasing processes. By varying the frequency of the drive pulse ω_d, Ramsey fringes can be observed in

$$P_e(\tau) = \frac{1}{2}\left[1 + \cos(\Delta\omega \cdot \tau)\right] e^{-\tau/T_2^*}, \tag{3.5}$$

where the detuning $\Delta\omega = \omega_q - \omega_d$ determines the frequency of the fringes. The decay time T_2^* extracted from this fit includes contributions from both energy relaxation and pure dephasing according to

$$\frac{1}{T_2^*} = \frac{1}{2T_1} + \frac{1}{T_\phi}, \tag{3.6}$$

where T_ϕ denotes the pure dephasing time arising from fluctuations in the qubit transition frequency. The observed oscillation frequency $\Delta\omega$ can be used to determine the qubit frequency with high precision, as $\omega_q = \Delta\omega + \omega_d$.

3.5 TLS Swap Spectroscopy

As motivated in section 2.5.5, the qubit energy relaxation time is shortened when a parasitic mode, like a TLS defect, comes into resonance with the qubit. Taking advantage of this, we can make individual resonances visible using the swap spectroscopy protocol, which is illustrated in Fig. 3.11 a). The qubit is excited with a π-pulse, then immediately tuned to a probe frequency, where it stays for a fixed duration τ. Afterwards the qubit is tuned back to the original frequency, where the qubit population is measured. Resonances will show up as dips in the remaining population as shown in Fig. 3.11 b). This sequence is repeated for different applied fields, like strain, electric or magnetic fields. The fields change the environment

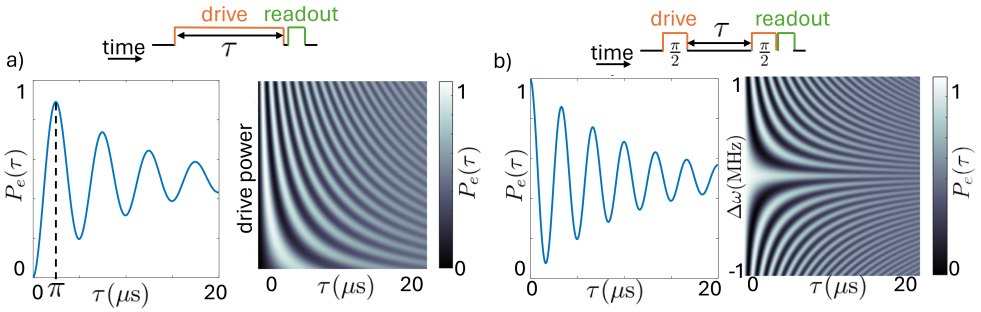

Figure 3.10: Illustration of typical time-domain qubit experiments. For both experiments, the pulse sequence is shown at the top, an example single trace on the left, and the dependence on the experimental control parameter on the right. a) Rabi experiment: a resonant microwave drive of variable duration τ induces coherent oscillations of the excited-state probability $P_e(\tau)$ between the qubit states. The right panel illustrates the dependence of the oscillation frequency on the drive power, corresponding to the Rabi frequency Ω_R. b) Ramsey experiment: two $\pi/2$ pulses separated by a delay time τ allow the qubit state to freely evolve, converting the accumulated phase into a measurable population difference. The right panel illustrates the dependence of the oscillation frequency on the detuning between the drive frequency and the qubit transition frequency, resulting in Ramsey fringes that decay with the characteristic time T_2^*.

of the defects in the amorphous lattice and thereby tune the ε parameter, as was introduced in section 2.1.3, resulting in hyperbolic TLS traces. TLS on the electrode surfaces react to both strain and electric fields, while TLS in the tunnel junctions only react to strain.
The sensitivity of the TLS detection is limited by the minimum qubit-TLS coupling strength that still produces a measurable change in the qubit decay. According to Eq. (2.65), the relaxation rate increases compared to the intrinsic qubit relaxation rate $\Gamma_{1,Q}$ when the qubit is brought close to resonance with a TLS. For a TLS to be detectable, the difference between the unperturbed decay $P_0 \exp(-\tau\Gamma_{1,Q})$ and the enhanced decay $P_0 \exp(-\tau\Gamma_1)$ must exceed the noise level of the measurement.

From this condition, an estimate for the minimum detectable coupling strength can be derived as

$$g_{\min} = \sqrt{-\frac{\Gamma}{2}\left(\frac{1}{\tau}\ln\left(\exp(-\tau\Gamma_{1,Q}) - \frac{2\sigma}{P_0}\right) + \Gamma_{1,Q}\right)}, \tag{3.7}$$

where τ denotes the interaction time during the swap sequence, σ is the standard deviation of the measured excited-state population, and Γ contains the decoherence rates of the qubit and the TLS. This expression provides an estimate of the smallest

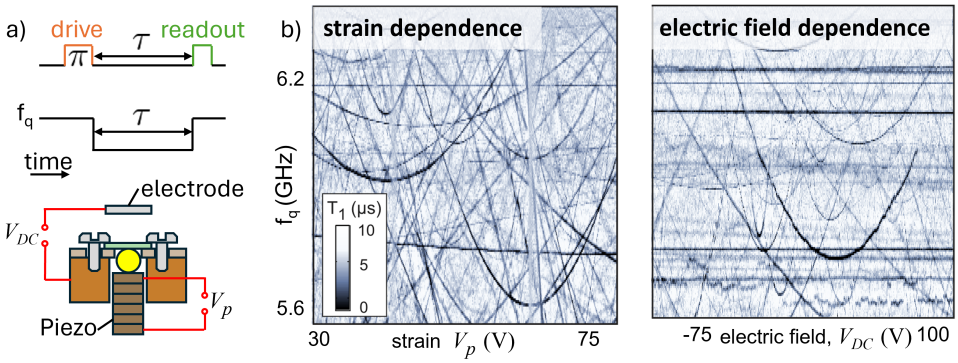

Figure 3.11: Swap spectroscopy used to detect individual TLS defects. a) Pulse sequence of the swap spectroscopy protocol. A π-pulse excites the qubit, which is then tuned to a probe frequency for a time τ. The remaining qubit population is then measured. b) Example swap spectroscopy maps (from [6]) showing the remaining qubit excitation as a function of probe frequency and applied tuning parameter, which are illustrated in the bottom-left inset as mechanical strain and applied electric field for the left and right scan, respectively. Dark lines indicate reduced qubit population caused by resonant coupling to individual TLS defects, which appear as characteristic hyperbolic traces.

coupling strength that can be resolved for a given qubit lifetime and measurement noise level. In practice, the optimal interaction time is typically chosen on the order of the qubit relaxation time, $\tau \approx 0.8\ T_1$, which maximizes the contrast between intrinsic qubit decay and TLS-induced relaxation. For further discussion of this, see e.g. [16].

This type of spectroscopy provides a powerful tool to study the electromagnetic environment of a qubit. A major goal of this thesis is to expand the scope of this method by developing fully tunable flux qubits designed to increase the TLS detection range, which is detailed in the next chapter.

4 Enhanced TLS Detection with Fully Tunable Flux Qubits

Based on the motivation outlined in chapter 1, namely the need for coherent and widely tunable superconducting circuits to systematically investigate microscopic decoherence mechanisms, we present here two experimental realizations of fully tunable flux qubits: fully tunable C-shunted flux qubits and fluxmon qubits.

4.1 Fully Tunable C-Shunted Flux Qubits

All measurements in this section were performed using capacitively shunted flux qubits as introduced in section 2.3.5. A micrograph of a device, showcasing its half-gradiometric design, is shown in Fig. 4.1 a).

4.1.1 Experimental Parameters

With the general functioning principles of fully tunable flux qubits derived in section 2, and the available experimental methods explored in section 3, we can now bring these together to find suitable experimental parameters. The goal of these considerations can be broken down into achieving two desirable properties:

Qubit Tunability - A broad range in which the qubit frequency can be tuned is desirable. The maximal range is determined by the qubit parameters E_J and E_C, which are fixed during sample fabrication. During experiment, the available range might be further constrained by the amount of current a bias line can support without heating the cryostat. This depends on the mutual inductances between the line and the qubit, the line's attenuation setup and the cryostat cooling power.

TLS Detectability - The qubit's capability of resolving individual TLS defects.

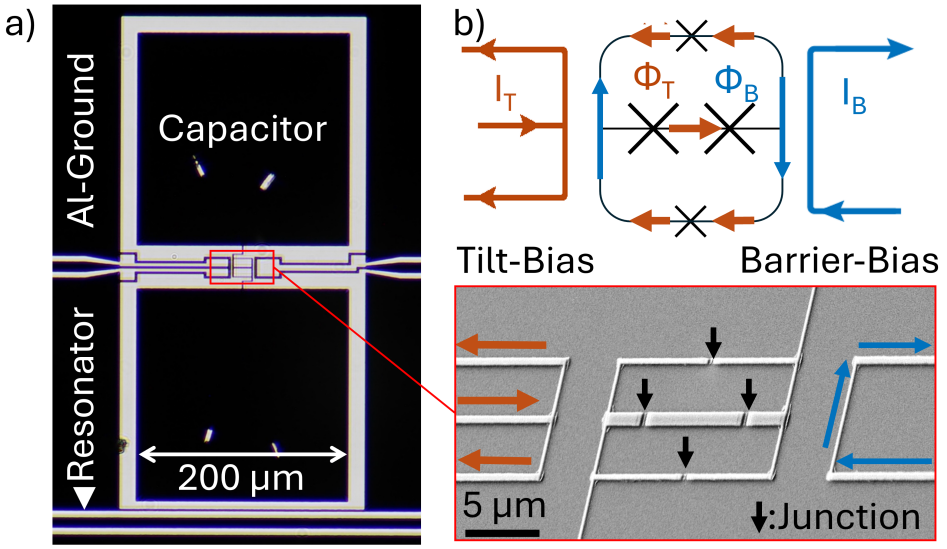

Figure 4.1: a) Micrograph of a fully tunable C-shunted flux qubit, with an inset zooming in on the junction layout under a 45° angle. b) Circuit diagram of the half-gradiometric junction layout. The currents (I_T, I_B) in the local bias lines induce the fluxes Φ_T and Φ_B.

As introduced in section 3.5, this depends on the qubit's T_1 time and the signal-to-noise ratio of the qubit population measurement. This in turn depends on the dispersive shift between qubit and resonator, the resonator's linewidth and the signal-to-noise ratio of transmission measurements in the setup.

The interdependencies of these aspects can make finding acceptable parameters a delicate process of balancing several trade-offs. In the following, we want to give a component-for-component overview on how the parameter choice can be approached. Another useful treatment of this topic can be found in [53].

Resonator Parameters - The resonator's relevant properties are its resonance frequency f_r, its linewidth κ and its coupling strength to the qubit g. The choice of f_r will influence the scannable frequency range, as the dispersive shift $\chi = g^2/\Delta$ reduces with the detuning $\Delta = f_q - f_r$. Here, we choose f_r in the 7-8 GHz range, which is both well addressable with the available electronics, and close to the center of the frequency range of interest. While a higher g leads to a larger χ, it also increases the Purcell-loss, and thereby creates a low-T_1 band around f_r. Our choice of $g \approx 75$ MHz leads to a χ of at least 700 kHz in the 0-15 GHz range. The resulting readout contrast is further determined by κ, which depends primarily

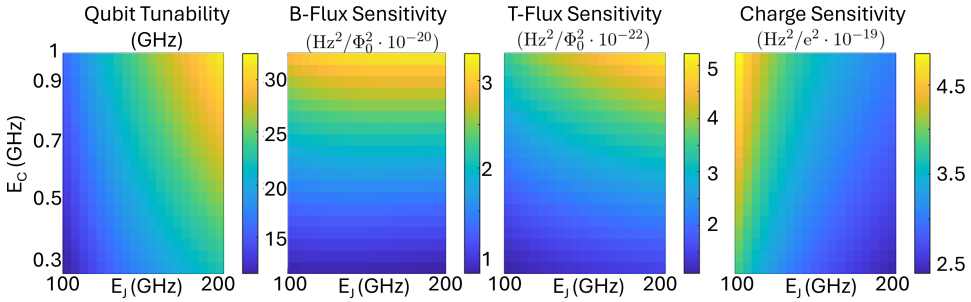

Figure 4.2: Simulated qubit properties as a function of the design parameters E_J and E_C. From left to right: the achievable qubit tuning range, the sensitivity to flux noise in the barrier loop, the sensitivity to flux noise in the tilt loop and the sensitivity to charge noise, which are here defined as $1/\hbar^2 \left|\langle 1|\partial H/\partial \Phi_B|0\rangle\right|^2$, $1/\hbar^2 \left|\langle 1|\partial H/\partial \Phi_T|0\rangle\right|^2$, and $1/\hbar^2 \left|\langle 1|\partial H/\partial Q|0\rangle\right|^2$, respectively. The sensitivities are evaluated at the symmetry point $\Phi_T = 0$ for $\alpha = 0.5$.

on the coupling of the resonator to the transmission line. A stronger coupling leads to a larger κ, which leads to a larger Purcell-loss and a lower signal strength. On the other hand, a lower κ leads to a slower resonator ring-up and can prevent excitation microwaves from reaching the qubit, with the resonator acting like a Purcell-filter. We found a κ in the range of 0.5-1.5 MHz, which corresponds to a resonator quality factor $Q = 2\pi f_r/\kappa$ between 3,000 and 10,000, to be compatible with our requirements.

Qubit Parameters - As given by Eq. (2.49), the qubit is defined by the energy scales E_J and E_C, and the junction scaling factor α. Since $1 > \alpha > 0.5$ leads to a double-well qubit potential and $0.5 > \alpha$ to a single-well, a good approach is to first determine a suitable α-factor, based on the desired regime. In fully tunable flux qubits, α can effectively be reduced by the control flux Φ_B during experiment, but not increased, so a design value slightly above the desired range is a prudent choice. In other architectures, it has been shown that an asymmetric α-SQUID can be used to further adjust the available effective α-range [38], yet here this would compromise the half-gradiometric nature of the design. To explore both the double-well and single-well regimes, we chose α in the 0.55 to 0.85 range.
To find suitable E_J and E_C parameters, we simulate the expected tuning range and noise sensitivites as shown in Fig. 4.2. At the $\Phi_\mathrm{T} = 0$-sweet spot, tuning range increases with both E_J and E_C, charge noise sensitivity decreases with $E_\mathrm{J}/E_\mathrm{C}$, while flux noise sensitivity increases with $E_\mathrm{J}/E_\mathrm{C}$. To prioritize protection from charge noise, which has been shown to be the dominant relaxation mechanism in similar devices [32], we chose a relatively high $E_\mathrm{J}/E_\mathrm{C}$ between 100 and 350. Combined with a desired tuning range of ≈ 20 GHz, this fixes the desired E_J and E_C values

as shown in table 4.1.

Bias Lines - Currents in the bias lines, i.e. I_B and I_T, induce flux in the qubit loops, defining the desired inductances $M_B = \Phi_B / I_B$ and $M_T = \Phi_T / I_T$ and the parasitic inductances $M'_B = \Phi_T / I_B$ and $M'_T = \Phi_B / I_T$. The energy relaxation caused by bias line noise is proportional to the square of these inductances, setting an upper limit for the desired values. A properly filtered bias line will radiate Johnsson-Nyquist noise at the coldest cryostate stage temperature into the qubit. For our circuits, assuming a 25 mK temperature and a 50 Ω bias line impedance, a value of $M_T = 2$ pH gives a T_1-limit of ≈ 50 µs (see section 4.1.3), which should not be exceeded. Figure 4.2 shows that the qubit is less sensitive to energy relaxation caused by noise in the barrier-loop, causing the expected T_1-limit at a value of $M_B = 2$ pH to be in the milliseconds.

4.1.2 Qubit Bring-up

After the qubits were fabricated as detailed in section 3.1, the following measurements were performed in the setup shown in section 3.2, beginning with time-domain characterizations introduced in section 3.4.1.
First, a VNA frequency scan at sufficiently high probe power decouples the resonator from the qubit, allowing the bare resonator frequency f_r to be identified. Then, the qubit–resonator coupling strength g is extracted from the avoided crossing that appears when the qubit is tuned through the resonator frequency.
Due to fabrication variance, the mutual inductances M_B and M_T, as well as the bias line crosstalk can deviate from the desired design parameters. Furthermore, during cooldown, offset-flux is trapped on the sample leading to *a priori* unknown offsets in the bias fluxes Φ_B and Φ_T. Therefore, these parameters need to be characterized experimentally. While this could be achieved with a full spectroscopy of the qubit at any $\Phi_\mathrm{B} - \Phi_\mathrm{T}$-combination, these measurements would be needlessly cumbersome and time consuming. A more streamlined method for these preliminary calibrations is to only measure the transmission S_{21} at a fixed probe frequency f_probe, while

Table 4.1: Extracted parameters for qubits A and B, defined with respect to the Hamiltonian Eq. (2.49). Design values are displayed in brackets.

	α	E_J (GHz)	E_C (GHz)	g (MHz)	f_res(GHz)	tuning-range
A	0.83 (0.85)	160 (164)	0.6 (0.5)	75	7.662	60 kHz-21 GHz
B	0.6 (0.55)	89 (61)	0.4 (0.57)	62	7.615	70 MHz-13 GHz

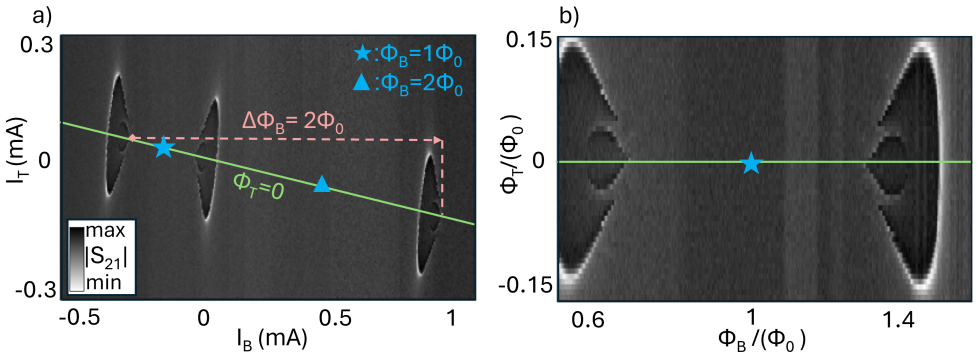

Figure 4.3: a) "Fireball" calibration measurements used to identify symmetry points in the Φ_T-Φ_B-landscape and calibrate the bias line cross-talk. b) The same measurement with corrected cross-talk, with the bias now expressed in terms of the fluxes Φ_B and Φ_T. Measurements were performed on sample A.

sweeping the bias-currents I_B and I_T, which results in the so-called "fireball"-scans, as described in section 3.4.1.
An example of such a scan is shown in Fig. 4.3 a). We use the tear-shaped regions of low qubit frequency to orient ourselves and map the applied bias-currents to the induced bias fluxes. First, we identify the line connecting the tips of tear-shapes as the $\Phi_T = 0$-line. The point of lowest qubit frequency, where $\Phi_B = \Phi_0$, is found on this line at the mid-point between tear-shapes which point towards each other and is indicated by a star. The point of highest qubit frequency, where $\Phi_B = 2\Phi_0$, is indicated by a triangle and is found at the mid-point between tear shapes pointing away from each other. We correct the bias line crosstalk by balancing the bias line currents so that the $\Phi_T = 0$-line is leveled and the scan is mirror-symmetric with respect to it. The same scan with corrected cross-talk is shown in Fig. 4.3 b). A discussion of the observed crosstalk and further notes on the bias line design can be found in section 6.2.

After these basic calibrations, we characterize the qubit parameters by performing spectroscopy (see section 3.4.2) along the zero-tilt line ($\Phi_T = 0$), while varying the barrier height by sweeping Φ_B. Figure 4.4 a) shows the measured spectroscopy together with the expected behavior from the design parameters and a fit of the qubit transition frequency f_q, obtained by numerical diagonalization of the qubit Hamiltonian. The design parameters are in good agreement with the data and imply the desired large tuning range of ≈20 GHz according to the Hamiltonian model. We note however that due to the chosen filtering setup, only a 3-8 GHz

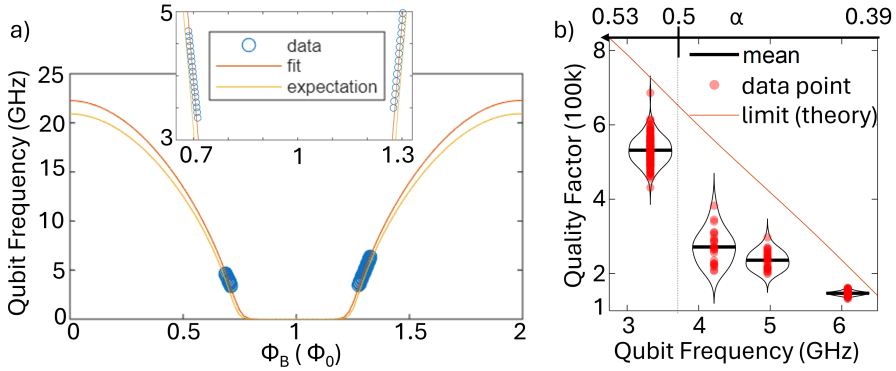

Figure 4.4: a) Qubit A spectroscopy data compared to the expectation from design values (yellow line) and a fit of Eq. (2.49) to the data (red line). b) Violin- and scatter-plots of quality factor measurements at the potential symmetry point $\Phi_T = 0$ for different qubit frequencies, which correspond to different α-values, compared to the theoretical limit (orange line). The mean quality-factors (from left to right) correspond to T_1 of 26.8 µs, 10.2 µs, 7.6 µs and 3.9 µs.

range is directly observed.
All extracted parameters are detailed in table 4.1.

4.1.3 Energy Relaxation Measurement

We measure the qubit energy relaxation time T_1 for a symmetric potential at different qubit frequencies by tuning the size of the potential barrier via the flux $\Phi_B$and following the pulse sequence outlined in section 3.4.2. Since the T_1 time of a device fluctuates over time (see e.g [54]), measurements are repeated multiple times at the same point.
Figure 4.4 b) shows that the qubit reaches an average quality factor $Q = 2\pi f_q\, T_1$ up to 530k at an operation frequency of 3.32 GHz, which corresponds to $T_1 \approx 26\,\mu s$. The quality factor is comparable to that of transmon qubits (Q $\sim$ 600k) [9] and quarton qubits (Q $\sim$ 500k) [55] fabricated in the same facility.
To our knowledge, this is the longest reported energy relaxation time for a fully tunable flux qubit, exceeding the previously reported value of approximately 8 µs [38].

4.1.4 Energy Relaxation Analysis

We observe an increase in qubit coherence at lower qubit frequencies. Similar behavior has been reported in capacitively shunted flux qubits by other groups,

where the energy relaxation in this frequency range was found to be limited by a combination of readout-resonator induced Purcell loss and ohmic charge noise [32]. To compare our results with these findings and to understand how the addition of the α-loop and the local control bias lines affects the relaxation in our device, we estimate the contributions of common loss channels following the methods outlined in section 2.5.

Charge Noise
The relaxation rate induced by charge noise is calculated using Fermi's golden rule

$$\Gamma_{\text{charge}} = \frac{1}{\hbar^2} \left|\langle 1|\partial H/\partial Q|0\rangle\right|^2 S_Q(\omega_{\text{qubit}}), \tag{4.1}$$

where $\langle 1|\partial\hat{H}/\partial Q|0\rangle$ is the matrix element of the charge operator between the ground and first excited state, and $S_Q(f_{\text{qubit}})$ is the spectral density of induced charge noise evaluated at the qubit transition frequency. Using $\hat{n} = \hat{Q}/2e$ and Eq. (2.49), we derive $\partial\hat{H}/\partial Q = E_C/2e\,\hat{n}$ and calculate $n_{01} = \langle 1|\,\hat{n}\,|0\rangle$ numerically from the Hamiltonian, as detailed in section 2.4.
Ohmic charge noise is described by the spectral density $S_Q(\omega) = A_Q^2\omega/(\text{GHz})$. A value of $A_Q^2 = (10.4 \times 10^{-9}e)^2/\text{Hz}$ matches the data, which is in good agreement with the range of $A_Q^2 = (5.2 \times 10^{-9}e)^2/\text{Hz}$ to $(11 \times 10^{-9}e)^2/\text{Hz}$ found in comparable C-shunted flux qubits[32].

Purcell loss
The Purcell-induced energy relaxation is given by

$$\Gamma_{\text{Purcell}} = \frac{g^2\kappa}{(2\pi)^2(f_{\text{res}} - f_{\text{qubit}})^2}, \tag{4.2}$$

where f_{qubit} is the qubit frequency, f_{res} is the resonator frequency, g is the coupling strength between qubit and resonator, and κ is the resonator linewidth (i.e., its energy decay rate). The coupling strength is proportional to the charge matrix element, $n_{01} = \langle 1|\,\hat{n}\,|0\rangle$, and therefore frequency dependent. Here, n_{01} is calculated numerically from Eq. (2.49) and the proportionality matched to measurement.

Flux Noise
Analogous to charge noise, the energy relaxation rate caused by flux noise in the B- and T-loops is given by $\Gamma_{\Phi_i} = 1/\hbar^2 \left|\langle 1|\partial H/\partial\Phi_i|0\rangle\right|^2 S_{\Phi_i}(f_{\text{q}})$, $i \in [\text{B}, \text{T}]$. Here, we calculate these matrix elements numerically via phase space discretization from the qubit Hamiltonian (Eq. (2.49)). As possible noise sources, we consider intrinsic $1/f$-noise, and external noise coupled into the qubit via the bias lines.

The spectral density for $1/f$-noise is given by $S_\Phi^{1/f} = A_\Phi^2/f^\gamma$. Here, we assume $S_\Phi^{1/f}$ to be equal for both loops and choose $\gamma = 0.9$ and $A_\Phi^2 = (1.4e^{-6}\phi_0)^2/\mathrm{Hz}$ (as measured in [32]).
The bias line noise spectral density is given by $S_{\Phi_i}^{ex}(f) = M_i^2 S_{I_i}(f)$, with M_i being the mutual inductance between line i and the qubit loop, and S_{I_i} the current spectral density in line i. Since low-pass filters reject noise at the qubit frequency from higher temperature stages, we assume that Johnsson-Nyquist noise at the lowest temperature stage dominates the bias line current noise, whose spectral density is given by $S_{I_i}(f) = 2hf/R\coth(hf/2k_BT)$. We assume a line impedance of $R = 50\ \Omega$, $T = 0.025\,\mathrm{K}$ temperature, and use Sonnet to simulate the mutual inductances as $M_T = 1.46\,\mathrm{pH}$ and $M_B = 2.93\,\mathrm{pH}$.

Quasiparticle Loss
The decay rate caused by non-equilibrium quasiparticles is given by [47]

$$\Gamma_{qp} = |\langle 0|\sin\frac{\hat{\phi}}{2}|1\rangle|^2 S_{qp}(\omega_q), \tag{4.3}$$

where $S_{qp}(\omega_q)$ is the quasiparticle spectral density evaluated at the qubit frequency. In thermal equilibrium at low temperatures $k_BT \ll \Delta$, where Δ is the superconducting gap of the material, it is given by

$$S_{qp}(\omega) = \chi_{qp}\frac{8E_{Jk}}{\pi}\sqrt{\frac{2\Delta}{\omega}}, \tag{4.4}$$

with the normalized quasiparticle density χ_{qp} and E_{Jk} the Josephson energy of junction k. A lower bound of $\chi_{qp} = 10e^{-8}$ matches our data.

The total relaxation time is then given by $T_1^{total} = (\sum_i 1/T_i)^{-1}$, with i indexing the considered relaxation channels. Figure 4.5 a) shows that a combination of charge noise and Purcell loss explains most of the energy relaxation, while the order of magnitude of all considered channels can be seen in Fig. 4.5 b).
In the observed frequency range, the qubit is not significantly limited by flux noise, despite addition of the α-loop and local flux lines. We conclude that energy relaxation of future qubits could possibly be extended into the hundreds of microseconds by optimized qubit design using Purcell filters, and higher quality fabrication procedures and materials.

4.1.5 Strain-Tuned TLS Spectroscopy

The qubit's good energy relaxation and wide tunability makes it especially attractive to investigate TLS defects in a wide frequency range. As introduced in

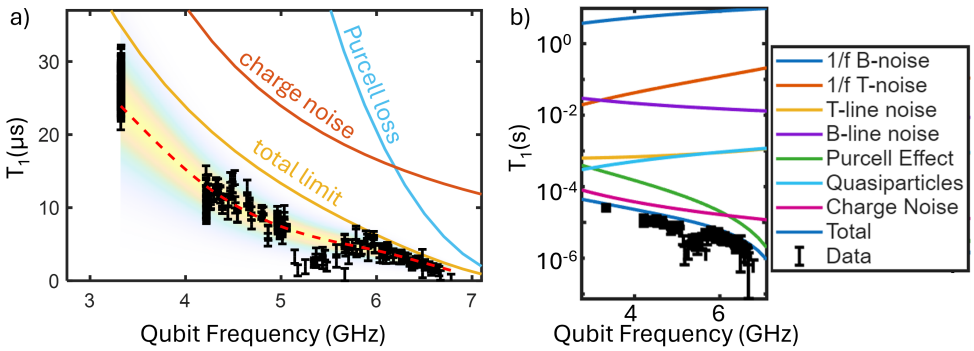

Figure 4.5: Qubit A T_1 measurements (black) compared to the dominant energy relaxation limits (see text). a) Zoomed in to the two most dominant channels. A dashed red line serves as a guide for the eyes, which is accompanied by a gaussian colorscale with constant relative spread ($\sigma/T1 = \text{const.}$). b) Orders of magnitude of all considered channels.

section 3.5, a powerful method to study origins of decoherence is qubit swap spectroscopy [6, 48], which reveals parasitic circuit modes and resonances of individual strongly-coupled TLS defects by minima in the frequency-dependent qubit T_1 time. Figure 4.6 shows examples of TLS spectra that were acquired with the qubit operating in the single- or double-well regime. Both spectra span a similar strain and frequency range, while a larger number of TLS are visible at higher qubit frequencies. Such measurements allow one to probe the frequency-dependence of the TLS density of states, which can give clues about underlying microscopic defect mechanisms. This first strain-tuned TLS spectroscopy in a flux qubit demonstrates TLS-detection in a frequency range spanning almost one octave. It furthermore showcases the unique combination of fast, wide, and coherent frequency tuning our design provides. We note that the experimentally demonstrated tuning range is still a fraction of what is theoretically possible. In future experiments, using an optimized experimental setup, qubit operation spanning close to four decades, e.g. 3 MHz - 21 GHz, could be achieved.

4.1.6 Discussion

In this section, we have presented a novel design for a fully tunable, capacitively shunted flux qubit featuring local flux biasing and a half-gradiometric geometry. We observed coherence times up to $T_1 = 25\mu s$ (Q=500k) and demonstrate qubit frequency tunability spanning nearly an octave, with a close to four decade range theoretically possible. This design combines the advantages of high coherence

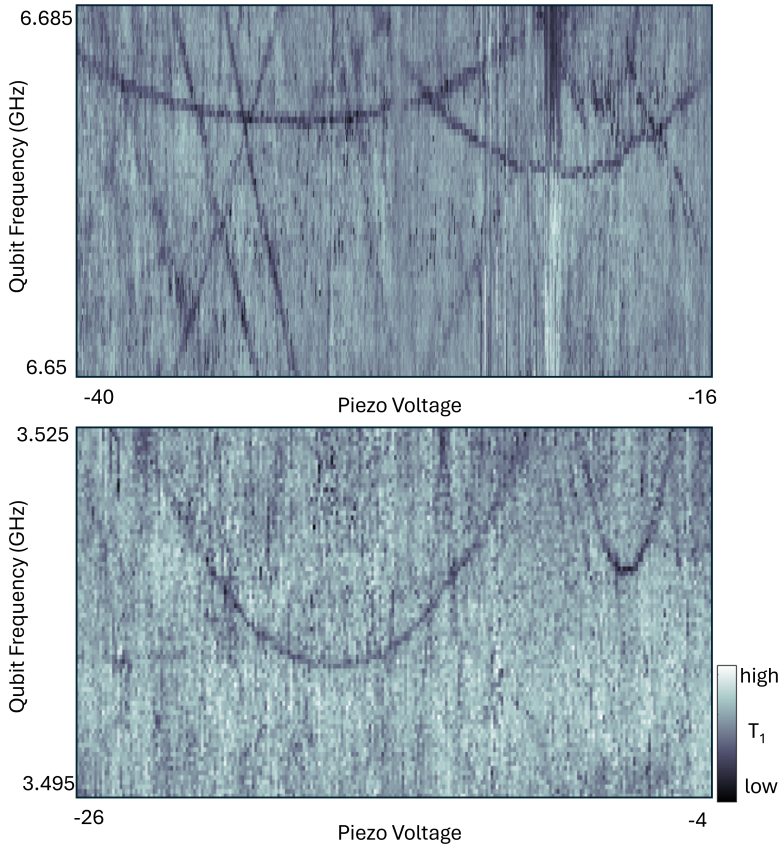

Figure 4.6: TLS-spectra in dependence of applied mechanical strain applied via a piezo-electric element. Dark lines indicate a drop in T_1 caused by resonant TLS defects. Spectra were taken on qubit B with similar strain ranges for different frequency intervals.

with fast and wide frequency control, making it a promising platform for quantum material research and quantum information experiments.
As a model application, we have demonstrated strain-tuned TLS spectroscopy, showcasing the capability to probe TLS defects across a wide frequency range and in both the single- and double-well qubit regimes. These features are particularly valuable for future investigations into TLS density of states and defect classification schemes.
Beyond TLS spectroscopy, the combination of good coherence and broad tunability renders this design attractive for a wide range of applications. With advances in hybrid architectures [56–58], gap-tunable flux qubits could see use as intermediaries between high-frequency qubits and low-frequency quantum memories,

where their wide tuning range could mitigate frequency crowding. The capability to quickly transition between single-well and double-well potential shapes, enables alternative qubit operation schemes [40], and provides a unique testbed for studying decoherence mechanisms in distinct potential landscapes. The ability to couple via flux [59], and to implement strong ZZ-type interactions through barrier biasing [37], further underlines their versatility as building blocks for multi-qubit systems.

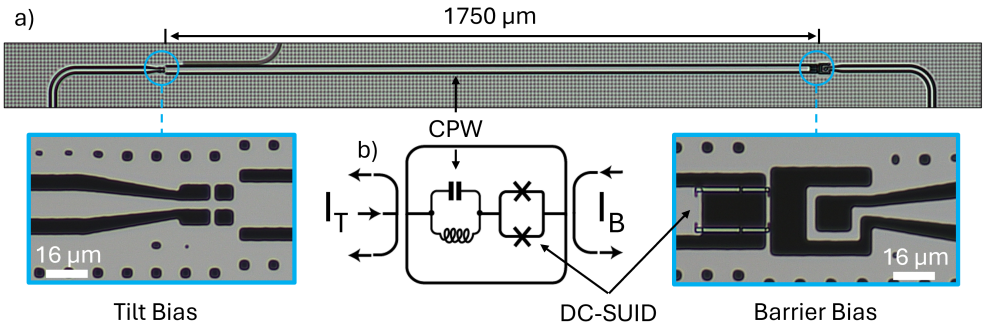

Figure 4.7: Fluxmon qubit device and circuit model. a) Micrograph of the fluxmon sample. A $\lambda/2$ coplanar waveguide is terminated by a DC-SQUID and controlled by two local bias lines. b) Equivalent circuit diagram. The CPW provides a linear inductance L and capacitance C, while the DC-SQUID acts as a tunable Josephson junction.

4.2 Fluxmon Qubits

Here, we present measurements performed on a fluxmon qubit. Detailed additional information on this unusual design can be found in [53].

4.2.1 Fluxmon Design

As shown in Fig. 4.7, a fluxmon consists of a $\lambda/2$ coplanar waveguide resonator terminated by a DC-SQUID. The waveguide provides a linear inductance L and distributed capacitance C, while the DC-SQUID acts as a tunable Josephson junction. The resulting Hamiltonian reads

$$\hat{H} = 4E_C\hat{n}^2 - E_J \cos\left(\pi\frac{\Phi_B}{\Phi_0}\right)\cos(\hat{\varphi}) + \frac{1}{2}E_L\left(\hat{\varphi} - 2\pi\frac{\Phi_T}{\Phi_0}\right)^2 \tag{4.5}$$

where $E_C = e^2/2C$ is the charging energy, E_J the Josephson energy, $E_L = (\Phi_0/2\pi)^2/L$ the inductive energy, $\hat{\varphi}$ the superconducting phase difference, $\hat{n}$ the number operator, and the tilt and barrier control fluxes Φ_T and Φ_B, respectively. The potential energy is identical to that of an RF-SQUID with a tunable Josephson term (compare Eq. (2.35)).
At the closed end of the waveguide, a current-divider style "tilt" bias line controls the flux Φ_T, which is equivalent to the Φ_{ext} in a conventional RF-SQUID (see Eq. (2.35)). At the DC-SQUID end, a symmetric "barrier" coil tunes the effective Josephson energy of the qubit via the control flux Φ_B.

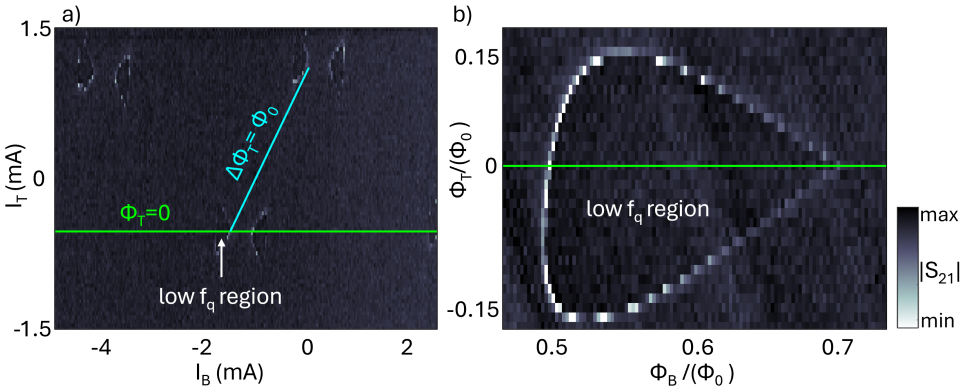

Figure 4.8: Calibration of the Fluxmon bias landscape using a fireball scan. a) Measured transmission $|S_{21}|$ as a function of the bias currents I_B and I_T. The characteristic tear-shaped region indicates combinations of bias currents where the qubit frequency f_q is lowest. The green line marks the symmetry line $\Phi_T = 0$. The distance between neighboring shapes (blue line) reveals the induced bias-flux. b) A finer scan of a low f_q region expressed in flux coordinates after calibration of the bias lines, showing the dependence on Φ_B and Φ_T.

The investigated sample was designed with a charging energy of $E_C/h \sim 0.19$ GHz, an inductive energy of $E_L/h \sim 270$ GHz, and a ratio of $\beta = E_J/E_L \approx 2.5$, which allows for exploration of the single-well and the multi-well potential energy regime. With these values, diagonalization of the Hamiltonian predicts a tuning range of 3 kHZ - 35 GHz.

4.2.2 Fluxmon Bring-up

The initial calibration of the fluxmon qubit follows the same procedure described in section 4.1.2. A high-power VNA scan reveals the bare resonator frequency $f_r = 7.35$ GHz. A scan of an avoided level crossing at lower power determines the qubit-resonator coupling $g = 65$ MHz.
Offset flux trapped during cooldown and deviations in the bias line mutual inductances are determined using two-dimensional "fireball" scans of the readout transmission while sweeping the bias currents I_B and I_T.

Figure 4.8 shows such a scan for the fluxmon device. As discussed in section. 4.1.2, regions of low qubit frequency appear as characteristic tear-shaped features, which provide convenient landmarks for identifying the symmetry line $\Phi_T = 0$ and calibrating the flux offsets.

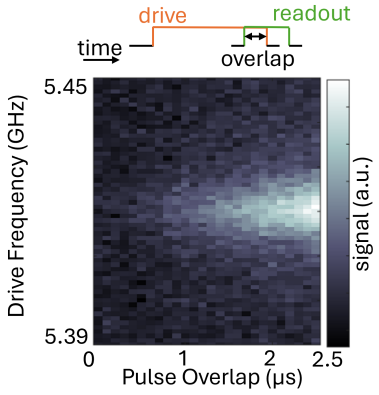

Figure 4.9: Pulse sequence (top) and measurement (bottom) of the qubit resonance being made visible despite fast energy relaxation by overlapping the drive pulse with the readout pulse.

Once the $\Phi_T = 0$ line is identified and the bias line crosstalk is compensated, the applied currents (I_B, I_T) are mapped to the flux biases (Φ_B, Φ_T). This calibration allows the device to be operated in well-defined regions of the potential landscape, ranging from the single-well regime to the double-well regime where the qubit gap becomes exponentially suppressed.

4.2.3 Fluxmon Coherence

The investigated qubit exhibited very short energy relaxation times. As a consequence, standard time-domain spectroscopy, π-pulse calibration and a measurement of T_1 by the standard methods as described in section 3.4.1 proved infeasible. Nonetheless, Fig. 4.9 shows that the qubit resonance could still be observed when adding a substantial overlap of the qubit drive-pulse with the readout-pulse. This hints towards a T_1 much lower than the resonator ring-up time.
Since this prevented systematic study of the device's energy relaxation, its exact origin remains unknown. However, the extensive dimensions of the qubit suggest a large presence of surface TLS, whose detrimental effect is made worse by the large electric fields in the long and tight gaps of the qubit's CPW-component, which enhance the coupling strength of TLS to the qubit mode. Furthermore, the qubit's large inductive loop is likely to couple to unwanted modes on the sample or its housing. Fluxmon qubits in the literature don't exceed a T_1 time of one microsecond [53, 60], which suggests inherent limitations of this design.

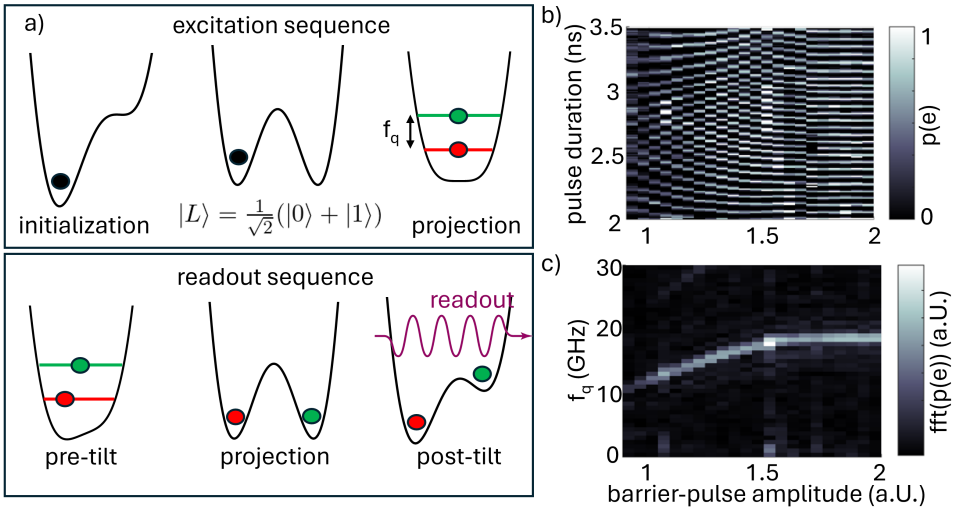

Figure 4.10: Microwave-free manipulation of the fluxmon qubit following the protocol introduced by Poletto *et al.* [40]. a) Schematic illustration of the pulse sequence. The qubit is first initialized in a localized persistent current state of a double-well potential. A fast flux pulse temporarily transforms the potential into a single-well, allowing coherent evolution between the two lowest energy eigenstates. After a variable pulse duration, the double-well potential is restored and the accumulated phase is projected back onto the flux basis for readout. b) Measured oscillations of the excited-state probability $p(e)$ as a function of duration and amplitude of the barrier-pulse, which projects into the single-well configuration. c) Fourier transform of the oscillation data revealing qubit oscillation frequencies in the range of approximately 10–20 GHz, determined by the level spacing of the transient single-well potential.

4.2.4 Microwave Free Operation

Since conventional microwave control of the qubit was not feasible under the experimental conditions, an alternative manipulation protocol based on fast flux pulses was employed. In this approach, the qubit state is controlled by dynamically modifying its potential shape. This protocol was first demonstrated for flux qubits by Poletto *et al.* [40] and relies on rapid transitions between double-well and single-well potential regimes.

The manipulation sequence is illustrated in Fig. 4.10a. The qubit is first initialized in one of the persistent current states $|L\rangle$ or $|R\rangle$ by strongly tilting the double-well potential. After initialization, the potential is returned to a symmetric double-well configuration with a high barrier, preventing tunneling between the wells.

A fast flux pulse applied to the barrier control line then lowers the central barrier and temporarily transforms the potential into a single-well configuration. In this

regime, the system is described by the two lowest energy eigenstates $|0\rangle$ and $|1\rangle$ of the single-well potential. The initial localized state can be written as a superposition $|L\rangle = (|0\rangle + |1\rangle)/\sqrt{2}$, such that the flux pulse itself prepares a coherent superposition of the two eigenstates without the use of external microwave driving.

The relative phase between these eigenstates evolves at the Larmor frequency $\omega_q = \frac{E_1 - E_0}{\hbar}$. After a variable pulse duration Δt, the potential is restored to the double-well configuration. This maps the accumulated phase back onto the flux basis $\{|L\rangle, |R\rangle\}$. A sufficiently high barrier suppresses tunneling between the wells, and effectively freezes the qubit state in its configuration. Then, a final tilt is applied to the potential, which allows the state occupation to be read out dispersively by observing the state-dependent dispersive shift of the readout resonator.

By varying the duration of the barrier pulse, coherent oscillations between the two flux states are observed. The oscillation frequency is determined by the level spacing of the transient single-well potential and can therefore be tuned by the amplitude of the flux pulse. Using this protocol we observed coherent oscillations in the range $f_{01} \approx$ 10–20 GHz, as shown in Fig. 4.10 b) and c).

4.2.5 Discussion

In this section we investigated a fluxmon qubit as an alternative platform for defect spectroscopy. The device architecture provides exceptional control over the circuit potential through the independent tuning of the barrier and tilt fluxes. This flexibility enables operation across different potential regimes and allows manipulation of the qubit state using purely flux-based control on a ns timescale.

Using the microwave-free manipulation protocol introduced by Poletto *et al.*, coherent oscillations with frequencies in the range of 10–20 GHz were observed. This demonstrates a wide qubit tuning range, desirable for the study of defects.

However, the investigated device exhibited very poor coherence properties. The short lifetime prevented the implementation of standard time-domain characterization protocols and made systematic measurements of T_1 and TLS swap spectroscopy infeasible. Since the sensitivity of TLS detection relies directly on the qubit coherence time, this severely limits the usefulness of the fluxmon as a detector of individual defects.

We therefore conclude that, despite its remarkable tunability and the ability to perform microwave-free qubit control, the fluxmon architecture in its present implementation is not well suited for TLS spectroscopy. Significant improvements

in coherence would be required before the device could serve as an effective probe of microscopic defects in superconducting circuits.

5 Parasitic RF-SQUIDs in Superconducting Qubits due to Wirebonds

5.1 Discovery and Motivation

During an experiment that was originally devised to study the response of microscopic defects to magnetic fields, we unexpectedly discovered a new type of macroscopic defect instead. We found a parasitic RF-SQUID (p-SQUID) that is formed by the linear inductances of on-sample wirebonds together with a parasitic Josephson junction (p-JJ). The formation of the p-JJ at a flawed contact between aluminium bonding wires and the natively oxidized aluminium of the sample ground-plane constitutes a previously unknown mechanism.
We believe this discovery to have relevant implications for the design of future quantum technology, as the quantized magnetic flux in the p-SQUID loop [61] may couple to neighboring qubits if they are based on SQUIDs, such as flux qubits [62] and fluxonium qubits[63], and if they employ DC-SQUIDs for tunability such as transmon qubits [44] and their couplers [64]. Moreover, AC-coupling of the p-SQUID's oscillatory eigenstates may induce dispersive shifts and avoided level crossings in neighboring qubits and resonators.

In our experiments, the existence of a p-SQUID was revealed from the characteristic signature it induces in the resonance frequency of a transmon qubit and its readout resonator during sweeps of the applied magnetic field. The data can well be fitted to a model that includes strong inductive and dispersive interactions of the p-SQUID with both the qubit and the readout resonator.
The conclusion that a bond wire is involved in the creation of the p-SQUID is supported by measurements with applied in-plane and off-plane magnetic fields which reveal the three-dimensional form of the p-SQUID loop. This is strongly supported by the fact that removing the wirebonds from the sample also removed the p-SQUID signature. Our finding reveals that parasitic Josephson junctions in

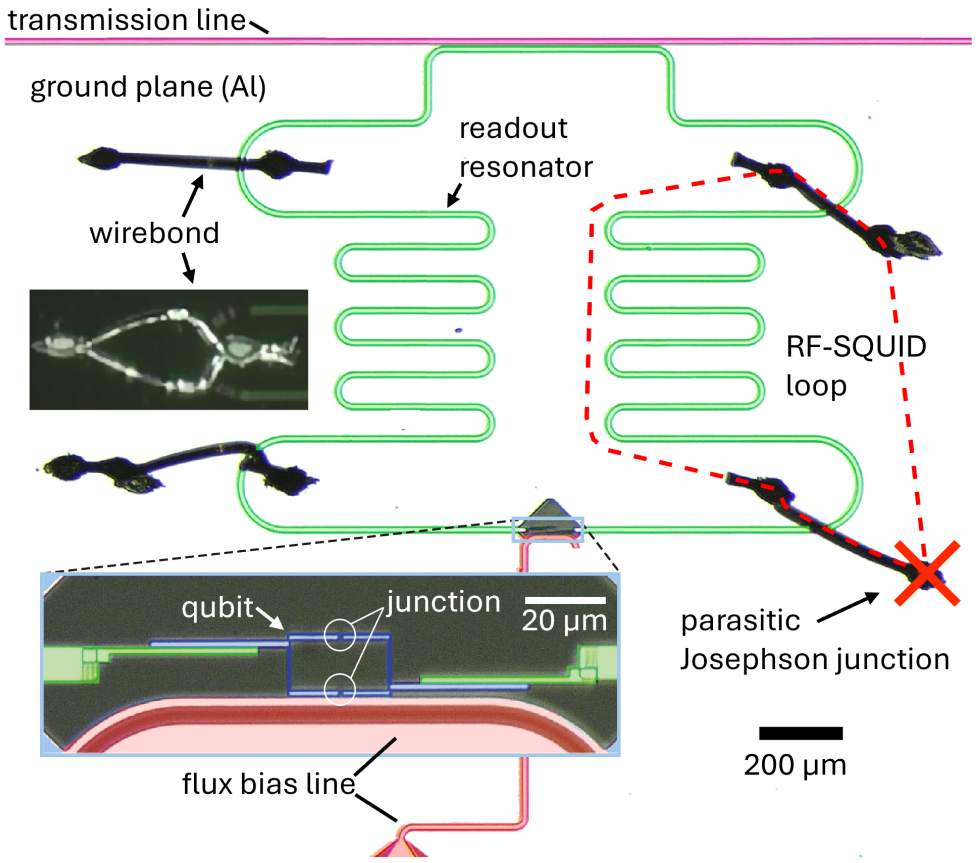

Figure 5.1: False-colored sample micrograph showing the coplanar $\lambda/2$ readout resonator (green) that is coupled at both ends to a mergemon qubit consisting of a DC-SQUID with two Josephson junctions (blue, see inset). Four wirebonds (black) connect the resonator's inner and outer ground planes to avoid slot-line modes. A parasitic Josephson junction within a wirebond (red cross) is enclosed in a superconducting loop (red dashed line) and so gives rise to an RF-SQUID that interferes with qubit and resonator.

the wiring circuitry of superconducting qubits add further decoherence channels for superconducting qubits, and can even completely spoil their operability.

5.2 Device and Measurement

As introduced in section 2.3.2, Transmon qubits conventionally consist of one or two submicron-sized Josephson junctions that are shunted by a planar capacitor. In

this experiment, we studied transmon qubits that employ larger-area Josephson junctions which possess sufficient self-capacitance so that no additional shunt capacitor is required. This so-called mergemon design [65, 66] significantly reduces the qubit footprint and promises less interference from charged two-level-system defects (TLS) known to reside at and near the interfaces of qubit electrodes [6, 49, 67, 68].
To enable in-situ tuning of the qubit's operation frequency, the junction is replaced by a DC-SQUID that can be flux-biased by a current in a nearby flux bias line. A photograph of the mergemon qubit sample is shown in the inset of Fig. 5.1.
Here, the qubit's resonance frequency f_q and state population are read out with a resonator that consists of a coplanar waveguide segment of electrical length $\lambda/2$, whose two open ends are each capacitively coupled to the opposing Mergemon electrodes as shown in Fig. 5.1. Since this design choice electrically isolates the inner ground plane of the coplanar resonator, we connected it by four air bridge wirebonds to the surrounding ground plane in order to suppress unwanted slotline modes. More details on this type of qubit can be found in [51].

In section 2.3.6 it was derived that for small qubit-resonator coupling energies hg_qr and sufficiently large detuning $|\delta| = |(f_\mathrm{q} - f_\mathrm{r})| \gg g_\mathrm{qr}$, the resonator's resonance frequency f_r obtains a dispersive shift [44]

$$f_\mathrm{r}' = f_\mathrm{r} - \frac{g_\mathrm{qr}^2}{\delta}. \tag{5.1}$$

In section 2.3.2 we've seen that the qubit transition frequency f_q depends on the flux Φ_Q threading its DC-SQUID and can be approximated by [44]

$$hf_\mathrm{q}(\Phi_\mathrm{Q}) = \sqrt{8E_C E_J(\Phi_\mathrm{Q})} - E_C, \tag{5.2}$$

where $E_C = e^2/2C_q$ is the charging energy of the qubit's capacitance C_q, e is the electron charge, $E_J = \hbar I_c/2e(\sqrt{\cos(\pi\Phi_\mathrm{Q}/\Phi_0)^2 + d^2\sin(\pi\Phi_\mathrm{Q}/\Phi_0)^2})$ is the Josephson energy assuming two slightly different junctions with a total critical current I_c, $\Phi_0 = h/2e$ is the flux quantum, h is Planck's constant, and the junction's asymmetry factor $d = \frac{E_{J1}-E_{J2}}{E_{J1}+E_{J2}}$.
Using a network analyzer connected to the on-chip transmission line, the dispersive shift of the readout resonator is determined to estimate the qubit frequency as a function of the applied magnetic fields, as was introduced in section 3.4.1. In addition to the on-chip flux-bias line, the sample is enclosed in a solenoid to control the magnetic field $B_\parallel$ in-plane of the qubit circuit, while another coil above the qubit chip applies a magnetic field $B_\perp$ perpendicular to the chip's surface.

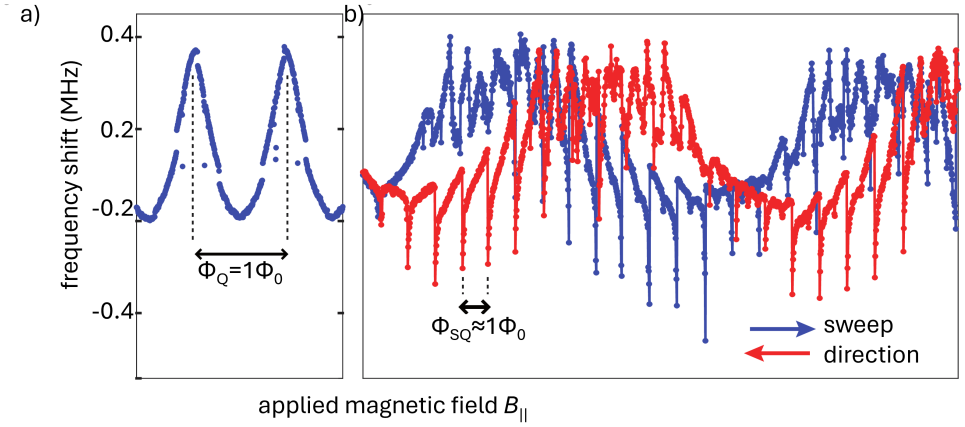

Figure 5.2: Resonance frequency shift of the readout resonator vs. the applied in-plane magnetic field $B_{||}$. a) Sample without chip-to-chip wirebonds, showing the expected modulation as the qubit is tuned according to Eq. (5.2) via the induced flux Φ_Q in its DC-SQUID. A shift of 0 corresponds to $f_r = 4.5662\,\text{GHz}$. b) With the wirebonds still in place, a saw-tooth pattern and sharp dips in the resonator frequency were additionally observed at regular intervals. Sweeping the applied magnetic field in different directions (blue and red curves) inverts the asymmetry of this signature, and reveals a large hysteresis in the qubit frequency. A shift of 0 corresponds to $f_r = 4.1902\,\text{GHz}$.

5.3 Evidence for Spurious Resonances

Figure 5.2 a) shows the expected periodic oscillations in the resonator's dispersive frequency shift when the qubit is tuned between its lowest and highest (at 4.5662 GHz ± 200 kHz) resonance frequencies according to Eqs. (5.1) and (5.2) by sweeping the magnetic field $B_{||}$. We note that $B_{||}$ should nominally be oriented perpendicular to the plane of the qubit's SQUID loop and therefore not couple to Φ_Q. Accordingly, we use these data to characterize the misalignment of the solenoid (see App. A for further details).

However, the data shown in Fig. 5.2 a) were acquired on the sample after the air bridge wirebonds had been removed. With the wirebonds still in place, the same experiment resulted in the data shown in Fig. 5.2 b). Most prominently, the resonator frequency displayed a sawtooth-pattern and pronounced asymmetric dips at regular flux intervals in addition to the expected modulation. Moreover, there is a large hysteresis when the direction of the applied field is reversed, which also inverts the asymmetry of the signature.

5.4 SQUID-Qubit-Resonator Model

For a closer test of our model, we numerically simulate the data shown in Fig. 5.2 b), based on the expected RF-SQUID behaviour introduced in section 2.3.3.
Assuming weak coupling and only a single relevant mode in each component, the Hamiltonian describing the coupled Qubit-Resonator-pSQUID system is given by

$$\frac{\hat{H}(\phi_x)}{h} = \begin{bmatrix} f_{\mathrm{r},0} & g_{\mathrm{r,q}} & g_{\mathrm{pSQ,r}} \\ g_{\mathrm{q,r}} & f_{\mathrm{q},0} & g_{\mathrm{pSQ,q}} \\ g_{\mathrm{pSQ,r}} & g_{\mathrm{pSQ,q}} & f_{\mathrm{pSQ},0} \end{bmatrix}, \tag{5.3}$$

which contains the transversal coupling strengths between resonator, qubit, and p-SQUID as off-diagonal elements. The p-SQUID's small oscillation frequency $f_{\mathrm{pSQ},0}$ in an initial well is found from the p-SQUID's potential energy (see Eq. (2.35)) and the qubit resonance frequency $f_{\mathrm{q},0}$ is calculated from Eq. (5.2), taking into account that the flux in the qubit loop Φ_{Q} is a function of the applied field and the flux in the p-SQUID loop Φ_{pSQ}. Here, the 0-subscript indicates a bare resonance frequency that would be observed if there was no coupling between the subsytems.
For each value of bias flux Φ_{ext}, the escape from the p-SQUID's current potential well is implemented by initializing the p-SQUID's ground state in the next deeper well once the tunnel rate [69] exceeds a value of $(20s)^{-1}$ which corresponds to the time required for one measurement of f_{r}.

To compare the data shown in Figs. 5.3 to the system of interacting qubit, resonator, and p-SQUID , we simulate magnetic field sweeps and obtain the eigenfrequency of the resonator by numerical diagonalization of the Hamiltonian Eq. (5.3). Best-fitting model parameters are then obtained by a least-square fit routine. These are listed in Table 5.1 and were used to plot the red lines in Fig. 5.3.
The parameters of the qubit and its coupling to the resonator (see Table 5.2) were obtained from a fit to spectroscopy data on the sample after the wirebonds had been removed. We note that the readout resonator's frequency was 4.5662 GHz when the wirebonds were removed, and 4.1902 GHz with installed air bridge wirebonds as shown in Fig. 5.1.
Figure 5.3 a) shows a striking agreement between the model and the data. To test the hypothesis that a wirebond is involved in the loop of the p-SQUID, the experiment is repeated by sweeping the out-of-plane component of the applied magnetic field $B_{\perp}$ as shown in Fig. 5.3 b). A comparison of the flux periodicity of the p-SQUID (given by the distance between dips in f_{r}) with that of the qubit (the distance between the broader maxima in f_{r}) shows that the relative coupling of qubit and p-SQUID to the B-field depends on its direction. This is consistent with

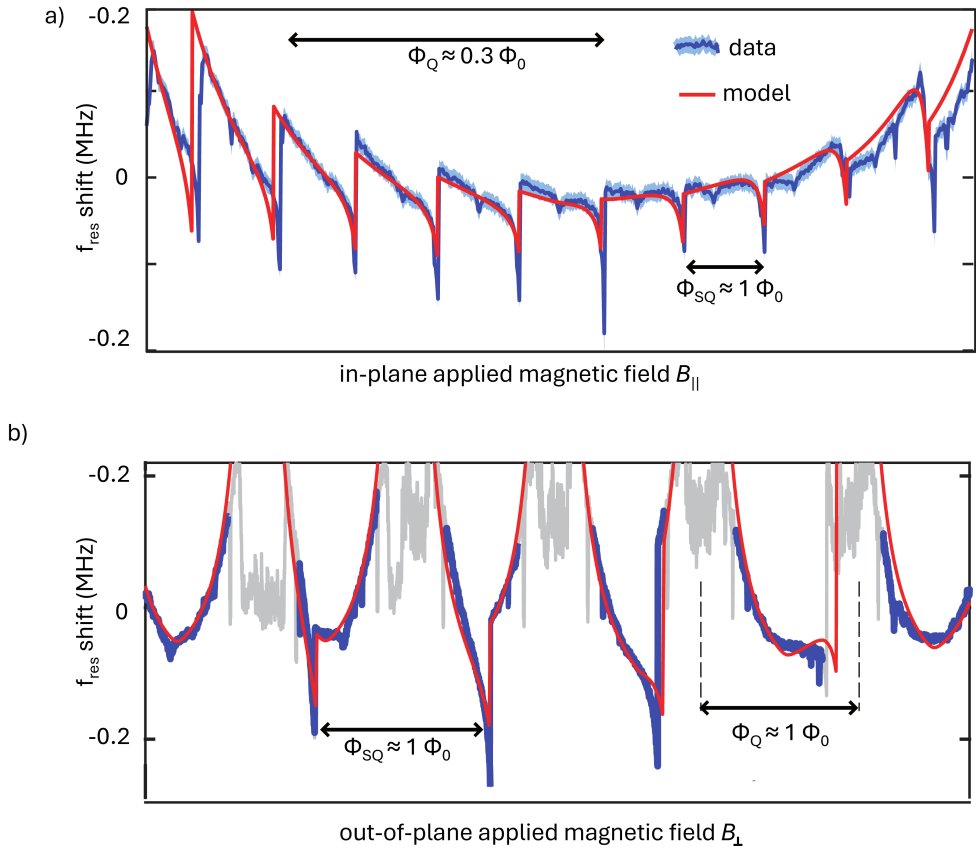

Figure 5.3: Dispersive shift of the readout resonator (a) vs. applied in-plane magnetic field $B_{\parallel}$, and (b) vs. the applied perpendicular field $B_{\perp}$. The red lines show good agreement with the model's prediction, using the same fitting parameters for both measurements.

the three-dimensional geometry of the wirebond's loops.
We note that the data obtained near maxima of the qubit frequency is distorted due to the small detuning of qubit and resonator, and has therefore been omitted from the fits.

5.5 Fit Parameters

Due to the large number and not fully independent model parameters, the confidence interval of most fitting parameters greatly exceeds their values so that we

cannot obtain precise information on the p-SQUID's parameters and geometry in a completely free fit.

parameter	value	description
$f_{\mathrm{res},0}$	4.19 GHz	uncoupled resonator frequency
$g_{\mathrm{pSQ,r}}$	9.9 MHz	coupling strength p-SQUID-resonator
$g_{\mathrm{pSQ,q}}$	70.3 MHz	coupling strength p-SQUID-qubit
ϕ^{Q}_{slope}	0.177 Φ_0	Φ_{Q} induced between well jumps
ϕ^{Q}_{qjump}	0.116 Φ_0	Φ_{Q} jump at well jump
L_{pSQ}	474 pH	p-SQUID inductance
C_{pSQ}	10.3 pF	p-SQUID capacitance
$I_{c,\mathrm{pSQ}}$	7.85 μA	p-SQUID critical current

Table 5.1: Model parameters and their values that best fit the data as shown in Fig. 5.3. We note that due to large uncertainties in the fitting values, the fit only serves for a qualitative comparison with the model.

parameter	value	description
E_J	12.3 GHz	qubit Josephson energy
$f_{\mathrm{q,max}}$	4.125 GHz	maximum qubit frequency at zero flux
E_C	0.19 GHz	qubit charge energy
d	0.12	qubit JJ asymmetry factor
$g_{\mathrm{q,r}}$	0.014 GHz	coupling strength qubit-resonator

Table 5.2: Qubit parameters, obtained in spectroscopy after removal of wirebonds.

To further pin down the range of p-SQUID parameters which result in reasonable agreement with the data, we fixed the parameter $\beta_L = 2\pi L_{\mathrm{pSQ}} I_{\mathrm{C,pSQ}}/\Phi_0$ to the value of 11.3 to ensure that the p-SQUID hysteresis matches the data shown in Fig. 5.2. A value of the p-SQUID inductance L_{pSQ} was then chosen, and the pJJ's critical current $I_{\mathrm{C,pSQ}}$ was calculated accordingly. The other parameters listed in Table 5.1 were kept as free fitting parameters.
Figure 5.4b shows the deviation from the data in the form of the root mean square error of the fit. The fit quality remains rather constant for a wide range of L_{pSQ} between 0.1-1.7 nH. For higher values, the fit quickly becomes worse as it becomes impossible to fulfill the three boundary conditions imposed by the p-SQUID-hysteresis, the fixed L_{pSQ}, and the requirement that the p-SQUID's resonance frequency must always exceed that of the readout resonator.
The uncertainties in the p-SQUID capacitance C_{pSQ}, and the parameters controlling

the p-SQUID-qubit flux-coupling ϕ^Q_{slope}, ϕ^Q_{qjump}, range between 5-12%. This is a much more narrow uncertainty range compared to a fit where all parameters are left free. The uncertainty in the dispersive coupling strengths $g_{\mathrm{pSQ,r}}$ and $g_{\mathrm{pSQ,q}}$ remains large (20 to 90%) because both contribute to the formation of the sharp dips in the resonator frequency.

5.6 Estimating p-SQUID Parameters

To estimate the range of realistic values for the inductance of the p-SQUID, we consider the geometry of the wirebonds shown in Fig. 5.1. Using optical microscopy, the lengths of the four wirebonds are measured as 381 µm, 466 µm, 466 µm, and 546 µm, respectively (see also App. A). Using the textbook formula [70]

$$L = \frac{\mu_0}{2\pi} l \left(\log\left(\frac{2l}{r}\right) - 1 \right), \tag{5.4}$$

where r is the wire radius and l is its length, we estimate inductances of 237pH to 379pH for our aluminum bond wires which have a diameter of 25 µm. In Fig. 5.5 b), the inductance per length is plotted also for other wire diameters, and compared to a common rule of thumb which estimates that a 1 mm long bond wire has a typical inductance of 1 nH.

To obtain a lower limit for the range of reasonable p-SQUIDinductance, we assume that the parasitic junction is contained in the shortest bond wire, and that the p-SQUID loop is closed by the parallel connection of the remaining three wirebonds. The upper limit is estimated by assuming that only the two longest bond wires are involved in the loop formation. This results in an estimated range of 347 pH $\lesssim L_{\mathrm{pSQ}} \lesssim$ 688 pH, which is well in accordance with the best fitting parameter L_{pSQ} of 474 pH. The limits are indicated by vertical dashed lines in Fig. 5.4.

For the p-SQUIDcapacitance, an upper limit can be estimated from the average area of a wirebond foot that is measured to about $A_{\mathrm{foot}} \approx (62\,\mu m)^2 = 3840\ \bar{}\mathrm{m}^2$. Taking $d = 2\,\mathrm{nm}$ as a minimal thickness of the capacitor dielectric (so that the whole bond wire foot would form a tunnel junction) and a relative permittivity $\varepsilon_r \approx 10$ for AlOx, we obtain $C_{\mathrm{pSQ}} = \epsilon_0 \epsilon_r A_{\mathrm{foot}}/d$ =170 pF which is much larger than the fitted $C_{\mathrm{pSQ}} \approx 10$ pF. Realistically, the whole bond foot area must contribute to C_{pSQ}. The discrepancy between this large area and relatively small (fitting) capacitance can

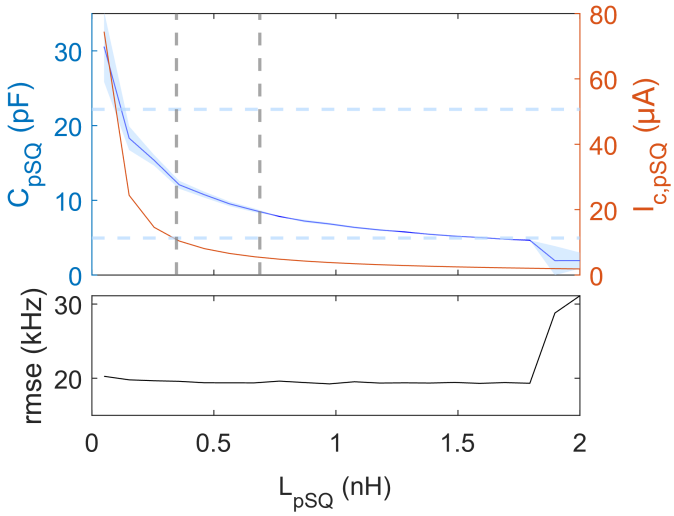

Figure 5.4: Top panel: Fitting values of C_{pSQ} and $I_{c,\mathrm{pSQ}}$ as a function of L_{pSQ} for fixed $\beta_L \equiv 2\pi L I_C/\Phi_0 = 11.3$ (as determined by a measurement of the p-SQUID's hysteresis). The bottom panel shows the root mean squared error of the fit, which remains similarly small in a wide range of L_{pSQ}. The vertical dashed lines in the top panel indicate the realistic range of bond wire inductances as described in the text.

be explained by a larger thickness and lower permittivity of the dielectric under the faulty bonding wire foot. For example, assuming that the bond foot area is contaminated by a 10 nm-thick layer of residual PMMA photoresist ($\varepsilon_r \approx 3$) results in a capacitance of 10 pF that corresponds to the best fitting value.

To reconcile the large bond foot area with the small capacitance (requiring a thick dielectric) and formation of a tunnel junction (requiring a tunnel barrier thickness of $\lesssim$ 3nm), one can assume that the thickness of the dielectric under the wirebond foot is non-uniform, possibly due to photoresist residuals. Figure 5.5 illustrates this situation in a cross-section through the wirebond foot. The actual contamination of our sample surface is unknown. In ultrasonic wirebonding, the amount of intermetallic formed at the bonded interface depends strongly on the bonding parameters such as ultrasound frequency, amplitude, and duration [71], so that inadequate settings could have played a role in the junction formation.

Since the Cooper-pair tunneling rate depends exponentially on the tunnel barrier thickness, the critical current of the parasitic junction can ot be predicted without exact knowledge of the junction geometry. The junction's active tunneling area

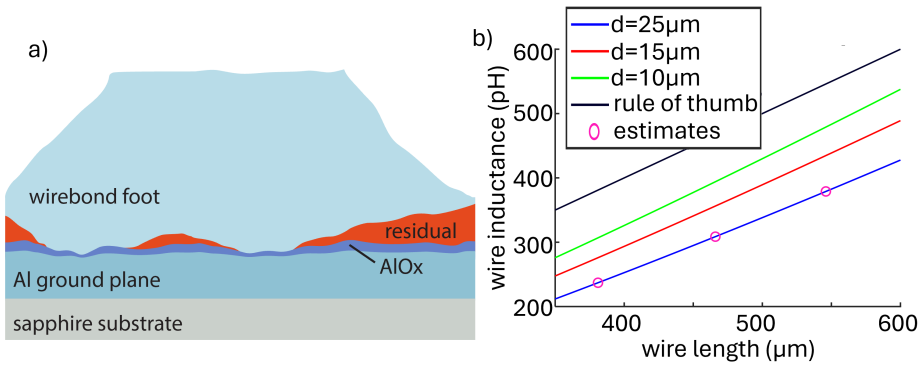

Figure 5.5: a) Sketch of the cross-section through the foot of a wirebond (not to scale), illustrating thickness variations of the native AlOx on the ground plane and a layer of contamination such as photoresist residual. The active junction area where Cooper pair tunneling occurs may be limited to small regions of least dielectric thickness in addition to pinholes. b) Bond wire inductance per length of wire calculated by the textbook formula for different wire diameters (blue, red and green line). Values for the on-sample wirebonds are encircled.

might be given by a small region of least surface contamination and could be largely affected by pinholes. In the restricted fit, compatible fit values for the critical current range between 2 and 80 µA as shown in Fig. 5.4.

5.7 Wirebond Investigation

Aiming to identify the flawed bond after the sample was warmed up, the bond wire bridges were touched and heavily bent using the micro-manipulator of a bonding station. However, all bonds appeared stable and did not disconnect easily.
Subsequently, chip-to-chip wirebonds were removed from the investigated qubit and the neighbouring qubit. With the wirebonds removed, the qubit returned to normal operation in subsequent cooldowns, as shown in Figs. 5.2. Images of the removal process and corresponding data can be found in App. A.

5.8 Discussion

The observed anomaly of resonator and qubit resonance frequencies in applied magnetic fields is fully explained by their interactions with a parasitic RF-SQUID. The notion that a faulty wirebond contains a parasitic tunnel junction is supported

by in- and out-of-plane magnetic field sweeps which confirm the three-dimensional form of the p-SQUID's loop. A further confirmation is the fact that the anomaly disappeared once the wirebonds were removed. Other possible origins of flux irregularities, such as the motion of trapped vortices [72], would not result in the observed strictly periodic signatures and observed dispersive resonance frequency shifts.

While it has been known that stray Josephson junctions between thin-film qubit electrodes are a source of qubit decoherence [6, 73], our finding sheds light on related issues in the remaining circuitry and packaging. In our experiment, two out of four qubits on the chip were inoperable due to their strong interference with the parasitic RF-SQUID formed by a faulty chip-to-chip wirebond. It can be seen as a coincidence that the parameters of the p-SQUID placed it into a regime where its interactions with qubit and resonator could be clearly observed. In more typical cases, the p-SQUID could be further detuned and induce only slight frequency shifts in a circuit that may remain unnoticed. Similarly, p-SQUIDs may be overlooked when only on-chip qubit flux bias lines are used that only slightly tune the p-SQUID's resonance frequency, while their parasitic modes would still contribute to decoherence and flux noise.

Related issues may arise for instance from detrimental modes in flux bias lines that were terminated by a junction in a flawed wirebond. Problems with parasitic junctions due to flawed air bridges, bond wires, or bump-pads in flip-chip architectures[74], may rise in importance as quantum processors increase in size and complexity. The observed strong DC-magnetic and AC-electric interactions of parasitic RF-SQUIDs can furthermore spoil the functionality of various other superconducting devices [75] such as for instance parametric amplifiers[76, 77], RSFQ-logic [78], MKID photon detectors[79], and passive resonator-based microwave filters [80].

6 Problems and Solutions

6.1 Shorts in Large Junctions

Josephson junctions in this work are fabricated using a three-angle Dolan deposition process detailed in section 3.1. This technique is suited to produce the

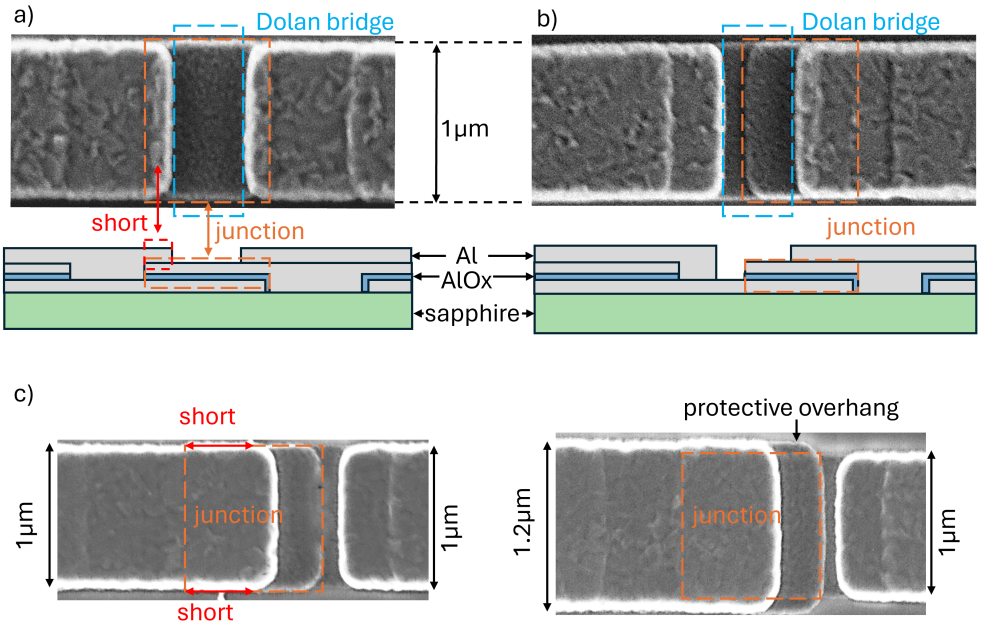

Figure 6.1: a) SEM image and cross-section schematic of a shorted junction (orange square). As both top and bottom electrodes extend beyond the Dolan bridge shadow (blue square), the junction is bypassed by a short (red square) which connects the top electrode and the bandage layer. b) SEM image and cross-section schematic of a junction where this short has been avoided, by having only the bottom electrode extend beyond the Dolan bridge shadow. c) SEM images of two junctions. The left one is shorted by the bandage layer connecting the bottom electrode at the sides of the junction (red arrows). In the right one this is avoided by depositing a wider top electrode, which protects the sides of the bottom electrode from the bandage layer.

wide-trench width (µm)	junction yield
1 - 1.05	0%
1.1	83%
1.25	100%

Table 6.1: Dependence of junction yield (percentage of short-free junctions) on the width of the wide trench.

comparatively large junctions of ≈ 1 µm^2 area, in order to realize the large Josephson inductances required in fluxmon qubits as well as the large capacitances required in mergemon qubits.
To achieve the desired junction size, a steep-angle Josephson deposition is used, where the evaporation angle is chosen such that the metal partially overshoots the Dolan bridge. While this technique enables larger overlap areas, it introduces an increased risk of unintentionally shorting the junction through the bandage layer deposited in subsequent processing steps.
Figure 6.1 illustrates two ways in which this short can occur and how it can be avoided.
First, the evaporation angles should be chosen such that the top electrode does not extend beyond the Dolan bridge. As shown in Fig. 6.1 a), an overextended top electrode can short the junction. This issue is avoided when the electrode remains within the bridge region, as shown in Fig. 6.1 b).
Second, the trench where the bottom electrode extends beyond the Dolan bridge should be widened, so that the top electrode covers the sides of the bottom electrode and thereby protects it from being contacted by the bandage layer. Examples of shorted and functioning junctions are shown in Fig. 6.1 c).
At a junction width of ≈ 1 µm, widths of 1, 1.01, 1.025, 1.05, 1.1 and 1.2 µm for the wider trench were tested. Table 6.1 shows that a width of 1.2 µm reliably avoided this problem.

6.2 Notes on Bias Line Design

To ensure precise alignment with the qubit loops, bias lines for the fully tunable C-shunted flux qubits are defined in the same lift-off process as the junctions, as described in section 3.1.
The precision of the electron-beam allows for definition of structures down to the 10th of nanometers. It is important however to make the bias line wide enough, so that the required bias-currents don't exceed the critical current at which the bias line loses superconductivity and substantially heats the sample. With a Mutual

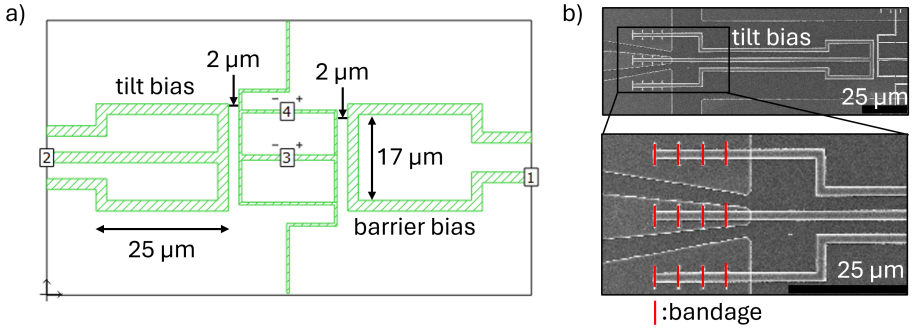

Figure 6.2: a) Sonnet simulation setup to simulate bias line inductances between the ports 1 (barrier-line), 2 (tilt-line), 3 (tilt loop) and 4 (barrier loop). The simulated values are $M_{14} = M_B = 2.93$ pH, $M_{23} = M_T = 1.46$ pH, $M_{24} = 0.15$ pH, and $M_{13} = 0.0001$ pH. b) SEM image of a tilt bias line with a zoom on the area where bandages (red lines) are used to connect the line to its launcher and the sample ground-plane.

inductance of $M \approx 1.5$ pH, a bias-current of ≈ 1.4 mA is needed to induce one quantum of flux. With a film thickness of 100 nm, a width of 2 µm was sufficient to perform the described experiments.

Fig. 6.2 a) shows the simulation setup used to estimate the mutual inductances between the bias lines and the qubit. We define the desired inductances $M_B = \Phi_B / I_B$ and $M_T = \Phi_T / I_T$ (see also Fig. 4.1) and the parasitic inductances $M'_B = \Phi_T / I_B$ and $M'_T = \Phi_B / I_T$. For the barrier-line, a Sonnet simulation predicts relative parasitic inductances of $M'_B / M_B = 3.4e^{-5}$ and for the tilt-line $M'_T / M_T = 0.102$. From the calibration procedure detailed in section 4.1.2, we measure $M'_B / M_B = 0.018$ $M'_T / M_T = 1.127$.

The very large M'_T / M_T points towards an imbalance in the current-division of the tilt-line. This might be caused by either a fault in the bandages which connect the line to the ground-plane (see Fig. 6.2 b), or from an unequal current return through the two ground plane parts separated by the line's launcher. These issues could be fixed by revision of the bandage fabrication recipe (e.g. more thorough development, aggravated oxide removal, more bandages, etc), or by balancing the separated grounds via an air bridge close to the qubit.

7 Conclusion and Outlook

Superconducting qubits are a leading platform for quantum computing. However, their performance remains limited by energy relaxation and decoherence mechanisms that are not yet fully understood. In particular, parasitic two-level systems (TLS) originating from atomic-scale defects are widely considered a dominant source of loss in superconducting circuits. Understanding and identifying such decoherence channels is therefore a crucial step toward scalable quantum processors.

In this work, we investigated fluxmon qubits and newly developed fully tunable C-shunted flux qubits as tools for studying microscopic decoherence mechanisms using TLS swap spectroscopy. During these experiments we also discovered a previously unknown type of parasitic resonance in the form of an RF-SQUID created by on-sample wirebonds.

Fluxmon Qubits consist of a $\lambda/2$ coplanar waveguide terminated by a DC-SQUID and effectively behave as an RF-SQUID with an in-situ tunable Josephson energy. Based on the design by C. Quintana, our fluxmon devices allowed independent control of both the potential asymmetry and the barrier height using nanosecond-scale flux pulses. Inspired by the work of S. Poletto, we implemented a microwave-free manipulation scheme and observed coherent Larmor oscillations over a frequency window of approximately 10-20 GHz.

However, the device coherence was severely limited, preventing TLS swap spectroscopy measurements. The observed performance is consistent with the few reports available for this qubit architecture. While fluxmon qubits offer exceptional tunability, our results indicate that the current implementation is not suitable for defect spectroscopy without significant improvements in coherence.

Possible improvements include reducing the device size to minimize surface participation, redesigning the coplanar waveguide to distribute surface currents over a wider area, and employing materials with lower surface loss.

Fully tunable C-shunted flux qubits are a new type of qubit we developed in this work based on the C-shunted flux qubit by Fey Yan. Replacing the α-junction by a DC-SQUID in a gradiometric arrangement together with the addition of e-beam patterned local bias lines allowed us to demonstrate full tunability with fast DC-pulses.

At the $\Phi_T = 0$ sweet spot, we observed a qubit tuning range of 3-7 GHz with a theoretic range of 60 kHz - 21 GHz possible. Our devices exhibited T_1times of up to 25 µs, making them at the time of writing the longest lived fully tunable flux qubits on record. Operation in both the single-well and double-well regime was demonstrated and TLS swap-spectroscopy was performed as a proof of concept.

We believe that this unique combination of fast and wide tunability, long energy relaxation and potential shape control makes this design well suited for future experiments. In an optimized setup, TLS swap-spectroscopy spanning up to 20 GHz could be performed, which would allow one to observe the density of states of TLS directly. This could provide long-needed insight in the TLS density of states and thereby help clarify their microscopic origins. Furthermore, the identification of low-TLS density frequency bands could lead to an overall improvement of qubit performance. This capability could be expanded to the study of different materials by interfacing the qubit with material probes through a coupling capacitance or a probe junction.

Parasitic RF-SQUIDs (p-SQUIDs) caused by wirebonds were discovered on a mergemon qubit sample during our experiments, by the characteristic, flux-dependent signature observed in the qubit's readout resonator. Fitting a qubit-resonator-SQUID model to the data further verified this conclusion, and revealed that the p-SQUID is both coupled to the qubit and the readout resonator directly. P-SQUIDS represent a previously undescribed type of parasitic system, and suggest the existence of Josephson tunnel contacts at the interfaces between some wirebonds and the sample ground-plane.

This sheds light on a possible pitfall in qubit prototyping, where on-chip wirebonds are often used as a convenient substitute for more labor-intensive air bridges.
Further related issues may arise for instance from detrimental modes in flux bias lines that were terminated by a junction in a flawed wirebond. Problems with parasitic junctions due to flawed air bridges, bond wires, or bump-pads in flip-chip architectures, may rise in importance as quantum processors increase in size and

complexity.

We believe that this type of p-SQUID might be an overall underreported phenomenon. Since the p-SQUID parameters are randomly distributed, only some of them land in the frequency range where circuits typically operate. Moreover, the p-SQUID might be geometrically insensitive to the magnetic field component used during experiment. In our findings for example, the p-SQUID signature revealed itself more clearly in the in-plane magnetic field scan, which is usually not performed in qubit operation. Finally, faulty samples are often discarded outright without finding the exact origin of their malfunction. To make sure a device is not detrimentally affected by a p-SQUID, we suggest performing wide magnetic field scans on qubits and resonators, looking for the characteristic periodic frequency dips. If available, varying the magnetic field direction would be ideal.

Bibliography

[1] R. P. Feynman: *Simulating physics with computers*. International Journal of Theoretical Physics **21** (1982), 467–488. DOI: 10.1007/BF02650179 (cit. on p. 1).

[2] D. Deutsch: *Quantum theory, the Church–Turing principle and the universal quantum computer*. Proceedings of the Royal Society A **400** (1985), 97–117. DOI: 10.1098/rspa.1985.0070 (cit. on p. 1).

[3] F. Arute et al.: *Quantum supremacy using a programmable superconducting processor*. Nature **574** (2019), 505–510. DOI: 10.1038/s41586-019-1666-5 (cit. on pp. 1, 2).

[4] G. Q. AI and Collaborators: *Quantum error correction below the surface code threshold*. Nature **638** (2025), 920–926. DOI: 10.1038/s41586-024-08449-y (cit. on p. 2).

[5] D. P. DiVincenzo: *The Physical Implementation of Quantum Computation*. Fortschritte der Physik **48** (2000), 771–783. DOI: https://doi.org/10.1002/1521-3978(200009)48:9/11<771::AID-PROP771>3.0.CO;2-E (cit. on p. 2).

[6] J. Lisenfeld, A. Bilmes, A. Megrant, R. Barends, J. Kelly, P. Klimov, G. Weiss, J. M. Martinis, and A. V. Ustinov: *Electric field spectroscopy of material defects in transmon qubits*. npj Quantum Information **5** (2019), 105. DOI: 10.1038/s41534-019-0224-1 (cit. on pp. 3, 4, 45, 55, 67, 75).

[7] J. Lisenfeld, A. Bilmes, S. Matityahu, S. Zanker, M. Marthaler, M. Schechter, G. Schön, A. Shnirman, G. Weiss, and A. V. Ustinov: *Decoherence spectroscopy with individual two-level tunneling defects*. Scientific Reports **6** (2016), 23786. DOI: 10.1038/srep23786 (cit. on pp. 3, 4).

[8] S. Eun, S. H. Park, K. Seo, K. Choi, and S. Hahn: *Shape optimization of superconducting transmon qubit for low surface dielectric loss*. Journal of Physics D: Applied Physics **56** (2023), 505306. DOI: 10.1088/1361-6463/acf7cf (cit. on p. 3).

[9] A. Bilmes, A. K. Händel, S. Volosheniuk, A. V. Ustinov, and J. Lisenfeld: *In-situ bandaged Josephson junctions for superconducting quantum processors*. Superconductor Science and Technology **34** (2021), 125011. DOI: 10.1088/1361-6668/ac2a6d (cit. on pp. 3, 52).

[10] W. A. Phillips: *Tunneling states in amorphous solids*. Journal of low temperature physics **7** (1972), 351–360. DOI: 10.1007/BF00660072 (cit. on pp. 3, 9).

[11] P. W. Anderson, B. I. Halperin, and C. M. Varma: *Anomalous low-temperature thermal properties of glasses and spin glasses*. The Philosophical Magazine: A Journal of Theoretical Experimental and Applied Physics **25** (1972), 1–9. DOI: 10.1080/14786437208229210 (cit. on pp. 4, 9).

[12] J. Lisenfeld, G. J. Grabovskij, C. Müller, J. H. Cole, G. Weiss, and A. V. Ustinov: *Observation of directly interacting coherent two-level systems in an amorphous material*. Nat Commun **6** (2015), 6182. DOI: 10.1038/ncomms7182 (cit. on p. 4).

[13] L. Faoro and L. B. Ioffe: *Interacting tunneling model for two-level systems in amorphous materials and its predictions for their dephasing and noise in superconducting microresonators*. Phys. Rev. B **91** (2015), 014201. DOI: 10.1103/PhysRevB.91.014201 (cit. on p. 4).

[14] C. Müller, J. L. Cole, and J. Lisenfeld: *Towards understanding two-level-systems in amorphous solids: insights from quantum circuits*. Reports on Progress in Physics **82** (2019), 124501. DOI: 10.1088/1361-6633/ab3a7e (cit. on pp. 4, 10).

[15] S. E. de Graaf, L. Faoro, L. B. Ioffe, S. Mahashabde, J. J. Burnett, T. Lindström, S. E. Kubatkin, A. V. Danilov, and A. Y. Tzalenchuk: *Two-level systems in superconducting quantum devices due to trapped quasiparticles*. Science Advances **6** (2020), eabc5055. DOI: 10.1126/sciadv.abc5055 (cit. on p. 4).

[16] A. Bilmes: *Resolving locations of defects in superconducting transmon qubits*. dissertation. Karlsruhe Institute of Technology (KIT), 2019. DOI: 10.5445/KSP/1000097557 (cit. on pp. 4, 33, 45).

[17] J. Lisenfeld, A. K. Händel, E. Daum, B. Berlitz, A. Bilmes, and A. V. Ustinov: *Mapping the positions of Two-Level-Systems on the surface of a superconducting transmon qubit*. 2025. arXiv: 2511.05365 [quant-ph] (cit. on p. 4).

[18] T. P. Orlando, J. E. Mooij, L. Tian, C. H. van der Wal, L. S. Levitov, S. Lloyd, and J. J. Mazo: *Superconducting persistent-current qubit*. Physical Review B **60** (1999), 15398–15413. DOI: 10.1103/physrevb.60.15398 (cit. on p. 5).

[19] J. E. Mooij, T. P. Orlando, L. Levitov, L. Tian, C. H. van der Wal, and S. Lloyd: *Josephson Persistent-Current Qubit*. Science **285** (1999), 1036–1039. DOI: 10.1126/science.285.5430.1036 (cit. on p. 5).

[20] I. Chiorescu, Y. Nakamura, C. J. P. M. Harmans, and J. E. Mooij: *Coherent Quantum Dynamics of a Superconducting Flux Qubit*. Science **299** (2003), 1869–1871. DOI: 10.1126/science.1081045 (cit. on p. 5).

[21] A. Lupaşcu, E. F. C. Driessen, L. Roschier, C. J. P. M. Harmans, and J. E. Mooij: *High-Contrast Dispersive Readout of a Superconducting Flux Qubit Using a Nonlinear Resonator*. Phys. Rev. Lett. **96** (2006), 127003. DOI: 10.1103/PhysRevLett.96.127003 (cit. on p. 5).

[22] P. De Groot, J. Lisenfeld, R. Schouten, S. Ashhab, A. Lupaşcu, C. Harmans, and J. Mooij: *Selective darkening of degenerate transitions demonstrated with two superconducting quantum bits*. Nature Physics **6** (2010), 763–766. DOI: 10.1038/nphys1733 (cit. on p. 5).

[23] A. Fedorov, A. K. Feofanov, P. Macha, P. Forn-Díaz, C. J. P. M. Harmans, and J. E. Mooij: *Strong Coupling of a Quantum Oscillator to a Flux Qubit at Its Symmetry Point*. Phys. Rev. Lett. **105** (2010), 060503. DOI: 10.1103/PhysRevLett.105.060503 (cit. on p. 5).

[24] T. Niemczyk, F. Deppe, H. Huebl, E. P. Menzel, F. Hocke, M. J. Schwarz, J. J. Garcia-Ripoll, D. Zueco, T. Hümmer, E. Solano, A. Marx, and R. Gross: *Circuit quantum electrodynamics in the ultrastrong-coupling regime*. Nature Physics **6** (2010), 772–776. DOI: 10.1038/nphys1730 (cit. on p. 5).

[25] M. Jerger, S. Poletto, P. Macha, U. Hübner, E. Il'ichev, and A. V. Ustinov: *Frequency division multiplexing readout and simultaneous manipulation of an array of flux qubits*. Applied Physics Letters **101** (2012), 042604. DOI: 10.1063/1.4739454 (cit. on p. 5).

[26] P. Bertet, I. Chiorescu, G. Burkard, K. Semba, C. J. P. M. Harmans, D. P. DiVincenzo, and J. E. Mooij: *Dephasing of a Superconducting Qubit Induced by Photon Noise*. Physical review letters **95** (2005), 257002. DOI: 10.1103/physrevlett.95.257002 (cit. on p. 5).

[27] F. Yoshihara, K. Harrabi, A. O. Niskanen, Y. Nakamura, and J. S. Tsai: *Decoherence of Flux Qubits due to1/fFlux Noise*. Physical review letters **97** (2006), 167001. DOI: 10.1103/physrevlett.97.167001 (cit. on p. 5).

[28] J.-L. Orgiazzi, C. Deng, D. Layden, R. Marchildon, F. Kitapli, F. Shen, M. Bal, F. R. Ong, and A. Lupascu: *Flux qubits in a planar circuit quantum electrodynamics architecture: Quantum control and decoherence*. Physical Review B **93** (2016), 104518. DOI: 10.1103/physrevb.93.104518 (cit. on p. 5).

[29] M. Stern, G. Catelani, Y. Kubo, C. Grezes, A. Bienfait, D. Vion, D. Esteve, and P. Bertet: *Flux Qubits with Long Coherence Times for Hybrid Quantum Circuits*. Phys. Rev. Lett. **113** (2014), 123601. DOI: 10.1103/PhysRevLett.113.123601 (cit. on p. 5).

[30] M. Steffen, S. Kumar, D. P. DiVincenzo, J. R. Rozen, G. A. Keefe, M. B. Rothwell, and M. B. Ketchen: *High-Coherence Hybrid Superconducting Qubit*. Phys. Rev. Lett. **105** (2010), 100502. DOI: 10.1103/PhysRevLett.105.100502 (cit. on p. 5).

[31] A. D. Córcoles, J. M. Chow, J. M. Gambetta, C. Rigetti, J. R. Rozen, G. A. Keefe, M. Beth Rothwell, M. B. Ketchen, and M. Steffen: *Protecting superconducting qubits from radiation*. Applied Physics Letters **99** (2011), 181906. DOI: 10.1063/1.3658630 (cit. on p. 5).

[32] F. Yan, S. Gustavsson, A. Kamal, J. Birenbaum, A. P. Sears, D. Hover, T. J. Gudmundsen, D. Rosenberg, G. Samach, S. Weber, J. L. Yoder, T. P. Orlando, J. Clarke, A. J. Kerman, and W. D. Oliver: *The flux qubit revisited to enhance coherence and reproducibility*. Nature Communications **7** (2016). DOI: 10.1038/ncomms12964 (cit. on pp. 5, 49, 53, 54).

[33] F. G. Paauw, A. Fedorov, C. J. P. M. Harmans, and J. E. Mooij: *Tuning the Gap of a Superconducting Flux Qubit*. Physical review letters **102** (2009), 090501. DOI: 10.1103/physrevlett.102.090501 (cit. on pp. 5, 6).

[34] S. Poletto, F. Chiarello, M. Castellano, J. Lisenfeld, A. Lukashenko, P. Carelli, and A. Ustinov: *A tunable rf SQUID manipulated as flux and phase qubits*. Physica Scripta **2009** (2009), 014011. DOI: 10.1088/0031-8949/2009/T137/014011 (cit. on p. 6).

[35] M. W. Johnson et al.: *Quantum annealing with manufactured spins*. Nature **473** (2011), 194–198. DOI: 10.1038/nature10012 (cit. on p. 6).

[36] D. Saida, M. Hidaka, and Y. Yamanashi: *4-Bit Factorization Circuit Composed of Multiplier Units With Superconducting Flux Qubits Toward Quantum Annealing*. IEEE Transactions on Applied Superconductivity **35** (2025), 1–11. DOI: 10.1109/TASC.2024.3486791 (cit. on p. 6).

[37] X. Zhu, A. Kemp, S. Saito, and K. Semba: *Coherent operation of a gap-tunable flux qubit*. Applied Physics Letters **97** (2010), 102503. DOI: 10.1063/1.3486472 (cit. on pp. 6, 57).

[38] T. Chang, T. Cohen, I. Holzman, G. Catelani, and M. Stern: *Tunable Superconducting Flux Qubits with Long Coherence Times*. Physical Review Applied **19** (2023), 024066. DOI: 10.1103/physrevapplied.19.024066 (cit. on pp. 6, 49, 52).

[39] K. V. Shulga, E. Il'ichev, M. V. Fistul, I. S. Besedin, S. Butz, O. V. Astafiev, U. Hübner, and A. V. Ustinov: *Magnetically induced transparency of a quantum metamaterial composed of twin flux qubits*. Nature Communications **9** (2018), 150. DOI: 10.1038/s41467-017-02608-8 (cit. on p. 6).

[40] S. Poletto, F. Chiarello, M. Castellano, J. Lisenfeld, A. Lukashenko, C. Cosmelli, G. Torrioli, P. Carelli, and A. Ustinov: *Coherent oscillations in a superconducting tunable flux qubit manipulated without microwaves*. New Journal of Physics **11** (2009), 013009. DOI: 10.1088/1367-2630/11/1/013009 (cit. on pp. 6, 57, 61).

[41] V. V. Schmidt, P. Müller, A. Ustinov, and I. V. Grigorieva: *Physics of Superconductors: Introduction to Fundamentals and Applications*. Berlin, Heidelberg: Springer, 2002 (cit. on p. 12).

[42] B. D. Josephson: *The discovery of tunnelling supercurrents*. Rev. Mod. Phys. **46** (1974), 251–254. DOI: 10.1103/RevModPhys.46.251 (cit. on p. 13).

[43] R. C. Jaklevic, J. Lambe, A. H. Silver, and J. E. Mercereau: *Quantum Interference Effects in Josephson Tunneling*. Phys. Rev. Lett. **12** (1964), 159–160. DOI: 10.1103/PhysRevLett.12.159 (cit. on p. 14).

[44] J. Koch, T. M. Yu, J. Gambetta, A. Houck, D. Schuster, J. Majer, A. Blais, M. Devoret, S. Girvin, and R. Schoelkopf: *Charge-insensitive qubit design derived from the Cooper pair box*. 2007. DOI: 10.1103/PhysRevA.76.042319 (cit. on pp. 18, 28, 29, 65, 67).

[45] G. Ithier, E. Collin, P. Joyez, P. J. Meeson, D. Vion, D. Esteve, F. Chiarello, A. Shnirman, Y. Makhlin, J. Schriefl, and G. Schön: *Decoherence in a superconducting quantum bit circuit*. Phys. Rev. B **72** (2005), 134519. DOI: 10.1103/PhysRevB.72.134519 (cit. on p. 28).

[46] E. M. Purcell, N. Bloembergen, and R. V. Pound: *Resonance Absorption by Nuclear Magnetic Moments in a Single Crystal of CaF_2*. Phys. Rev. **70** (1946), 988–988. DOI: 10.1103/PhysRev.70.988 (cit. on p. 28).

[47] G. Catelani, R. J. Schoelkopf, M. H. Devoret, and L. I. Glazman: *Relaxation and frequency shifts induced by quasiparticles in superconducting qubits*. Phys. Rev. B **84** (2011), 064517. DOI: 10.1103/PhysRevB.84.064517 (cit. on pp. 29, 54).

[48] R. Barends et al.: *Coherent Josephson Qubit Suitable for Scalable Quantum Integrated Circuits*. Phys. Rev. Lett. **111** (2013), 080502. DOI: 10.1103/PhysRevLett.111.080502 (cit. on pp. 30, 55).

[49] C. Wang, C. Axline, Y. Y. Gao, T. Brecht, Y. Chu, L. Frunzio, M. Devoret, and R. J. Schoelkopf: *Surface participation and dielectric loss in superconducting qubits*. Applied Physics Letters **107** (2015), 162601 (cit. on pp. 30, 67).

[50] W. A. Phillips: *Two-level states in glasses*. Reports on Progress in Physics **50** (1987), 1657 (cit. on p. 30).

[51] E. Daum, B. Berlitz, S. Deck, A. V. Ustinov, and J. Lisenfeld: *Investigation of Parasitic Two-Level Systems in Merged-Element Transmon Qubits*. 2025. arXiv: 2509.22593 [cond-mat.supr-con] (cit. on pp. 31, 67).

[52] A. Bilmes, A. K. Händel, S. Volosheniuk, A. V. Ustinov, and J. Lisenfeld: *In-situ bandaged Josephson junctions for superconducting quantum processors*. Superconductor Science and Technology **34** (2021), 125011. DOI: 10.1088/1361-6668/ac2a6d (cit. on p. 33).

[53] C. Quintana: *Superconducting flux qubits for high-connectivity quantum annealing without lossy dielectrics*. PhD thesis. Santa Barbara, CA, USA: University of California, Santa Barbara, 2017. URL: https://escholarship.org/uc/item/9844c3h3 (cit. on pp. 39, 48, 58, 60).

[54] K. Li, S. K. Dutta, Z. Steffen, B. S. Palmer, C. J. Lobb, and F. C. Wellstood: *Power-Law Scaling of Relaxation Time Fluctuations in Transmon Qubits*. IEEE Transactions on Applied Superconductivity **33** (2023), 1–5. DOI: 10.1109/TASC.2023.3243198 (cit. on p. 52).

[55] A. S. Kreuzer: *Quarton qubits with stacked Josephson junctions*. PhD thesis. Karlsruher Institut für Technologie (KIT), 2026. 148 pp. DOI: 10.5445/IR/1000190747 (cit. on p. 52).

[56] X. Zhu, S. Saito, A. Kemp, K. Kakuyanagi, S.-i. Karimoto, H. Nakano, W. J. Munro, Y. Tokura, M. S. Everitt, K. Nemoto, M. Kasu, N. Mizuochi, and K. Semba: *Coherent coupling of a superconducting flux qubit to an electron spin ensemble in diamond*. Nature **478** (2011), 221–224. DOI: 10.1038/nature10462 (cit. on p. 56).

[57] M. Reagor, W. Pfaff, C. Axline, R. W. Heeres, N. Ofek, K. Sliwa, E. Holland, C. Wang, J. Blumoff, K. Chou, M. J. Hatridge, L. Frunzio, M. H. Devoret, L. Jiang, and R. J. Schoelkopf: *Quantum memory with millisecond coherence in circuit QED*. Phys. Rev. B **94** (2016), 014506. DOI: 10.1103/PhysRevB.94.014506 (cit. on p. 56).

[58] O. Milul, B. Guttel, U. Goldblatt, S. Hazanov, L. M. Joshi, D. Chausovsky, N. Kahn, E. Çiftyürek, F. Lafont, and S. Rosenblum: *Superconducting Cavity Qubit with Tens of Milliseconds Single-Photon Coherence Time*. PRX Quantum **4** (2023), 030336. DOI: 10.1103/PRXQuantum.4.030336 (cit. on p. 56).

[59] S. H. W. van der Ploeg, A. Izmalkov, A. M. van den Brink, U. Hübner, M. Grajcar, E. Il'ichev, H.-G. Meyer, A. Fedorov, A. Shnirman, and G. Schön: *Controllable coupling of superconducting flux qubits*. Physical review letters **98** (2007), 057004. DOI: 10.1103/PhysRevLett.98.057004 (cit. on p. 57).

[60] C. M. Quintana et al.: *Observation of Classical-Quantum Crossover of* $1/f$ *Flux Noise and Its Paramagnetic Temperature Dependence*. Phys. Rev. Lett. **118** (2017), 057702. DOI: 10.1103/PhysRevLett.118.057702 (cit. on p. 60).

[61] J. Clarke and A. I. Braginski: *The SQUID handbook. Vol. 2. Applications of SQUIDs and SQUID systems*. Wiley-VCH, 2006 (cit. on p. 65).

[62] I. Chiorescu, Y. Nakamura, C. M. Harmans, and J. Mooij: *Coherent quantum dynamics of a superconducting flux qubit*. Science **299** (2003), 1869–1871 (cit. on p. 65).

[63] V. E. Manucharyan, J. Koch, L. I. Glazman, and M. H. Devoret: *Fluxonium: Single Cooper-pair circuit free of charge offsets*. Science **326** (2009), 113–116 (cit. on p. 65).

[64] Y. Chen, C. Neill, P. Roushan, N. Leung, M. Fang, R. Barends, J. Kelly, B. Campbell, Z. Chen, B. Chiaro, et al.: *Qubit architecture with high coherence and fast tunable coupling*. Physical review letters **113** (2014), 220502 (cit. on p. 65).

[65] R. Zhao, S. Park, T. Zhao, M. Bal, C. McRae, J. Long, and D. Pappas: *Merged-element transmon*. Physical Review Applied **14** (2020), 064006 (cit. on p. 67).

[66] H. Mamin, E. Huang, S. Carnevale, C. T. Rettner, N. Arellano, M. Sherwood, C. Kurter, B. Trimm, M. Sandberg, R. M. Shelby, et al.: *Merged-element transmons: Design and qubit performance*. Physical Review Applied **16** (2021), 024023 (cit. on p. 67).

[67] A. Bilmes, A. Megrant, P. Klimov, G. Weiss, J. M. Martinis, A. V. Ustinov, and J. Lisenfeld: *Resolving the positions of defects in superconducting quantum bits*. Scientific Reports **10** (2020), 1–6 (cit. on p. 67).

[68] C. E. Murray: *Material matters in superconducting qubits*. Materials Science and Engineering: R: Reports **146** (2021), 100646 (cit. on p. 67).

[69] K. Likharev: *Macroscopic quantum tunneling and dissipation in Josephson junctions and SQUIDs*. Physica B+C **108** (1981), 1079–1080. DOI: https://doi.org/10.1016/0378-4363(81)90843-3 (cit. on p. 69).

[70] E. B. Rosa: *The Self and Mutual Inductances of Linear Conductors*. Bulletin of the Bureau of Standards **4** (1908), 301–344. URL: https://nvlpubs.nist.gov/nistpubs/bulletin/04/nbsbulletinv4n2p301_A2b.pdf (cit. on p. 72).

[71] *Process Technology*. *Advanced Wirebond Interconnection Technology*. Boston, MA: Springer US, 2004, pp. 163–480. DOI: 10.1007/1-4020-7763-7_4 (cit. on p. 73).

[72] E. Marchiori, L. Ceccarelli, N. Rossi, G. Romagnoli, J. Herrmann, J.-C. Besse, S. Krinner, A. Wallraff, and M. Poggio: *Magnetic imaging of superconducting qubit devices with scanning SQUID-on-tip*. Applied Physics Letters **121** (2022) (cit. on p. 75).

[73] A. Dunsworth, A. Megrant, C. Quintana, Z. Chen, R. Barends, B. Burkett, B. Foxen, Y. Chen, B. Chiaro, A. Fowler, et al.: *Characterization and reduction of capacitive loss induced by sub-micron Josephson junction fabrication in superconducting qubits*. Applied Physics Letters **111** (2017), 022601 (cit. on p. 75).

[74] D. Rosenberg, D. Kim, R. Das, D. Yost, S. Gustavsson, D. Hover, P. Krantz, A. Melville, L. Racz, G. Samach, et al.: *3D integrated superconducting qubits*. npj quantum information **3** (2017), 42 (cit. on p. 75).

[75] A. I. Braginski: *Superconductor electronics: Status and outlook*. Journal of superconductivity and novel magnetism **32** (2019), 23–44 (cit. on p. 75).

[76] C. Macklin, K. O'brien, D. Hover, M. Schwartz, V. Bolkhovsky, X. Zhang, W. Oliver, and I. Siddiqi: *A near–quantum-limited Josephson traveling-wave parametric amplifier*. Science **350** (2015), 307–310 (cit. on p. 75).

[77] J. Aumentado: *Superconducting parametric amplifiers: The state of the art in Josephson parametric amplifiers*. IEEE Microwave magazine **21** (2020), 45–59 (cit. on p. 75).

[78] P. Bunyk, K. Likharev, and D. Zinoviev: *RSFQ technology: Physics and devices*. International journal of high speed electronics and systems **11** (2001), 257–305 (cit. on p. 75).

[79] B. A. Mazin: *Microwave kinetic inductance detectors: The first decade*. *AIP Conference Proceedings*. Vol. 1185. American Institute of Physics. 2009, pp. 135–142 (cit. on p. 75).

[80] D. E. Oates: "Microwave resonators and filters". *Handbook of Superconductivity*. CRC Press, 2022, pp. 596–608 (cit. on p. 75).

List of Publications

[1] B. Berlitz, S. Deck, A. V. Ustinov, and J. Lisenfeld: *Parasitic RF-SQUIDs in superconducting qubits due to wirebonds*. Superconductor Science and Technology **38** (2025), 095002. DOI: 10.1088/1361-6668/adfd92.

[2] B. Berlitz, A. K. Händel, E. Daum, A. V. Ustinov, and J. Lisenfeld: *Gradiometric, Fully Tunable C-Shunted Flux Qubits* (2025). arXiv: 2509.26024 [quant-ph].

[3] E. Daum, B. Berlitz, S. Deck, A. V. Ustinov, and J. Lisenfeld: *Investigation of Parasitic Two-Level Systems in Merged-Element Transmon Qubits*. 2025. arXiv: 2509.22593 [cond-mat.supr-con].

[4] J. Lisenfeld, A. K. Händel, E. Daum, B. Berlitz, A. Bilmes, and A. V. Ustinov: *Mapping the positions of Two-Level-Systems on the surface of a superconducting transmon qubit*. 2025. arXiv: 2511.05365 [quant-ph].

Appendix

A Supplementary Notes on P-SQUID Wirebonds

Figure A.1 a) shows a micrograph of the sample studied in chapter 5. Micrographs from different angles as shown in Fig. A.1 b) were used to estimate the individual wirebond lengths.
To estimate the misalignment of the in-plane magnetic field with respect to the chip's ground plane, we measure the periodicity of the qubit resonance frequency as a function of $B_{\parallel}$. Using the area of the qubit's DC-SQUID loop $A = 276\,\mu m^2$, we calculate the misalignment angle α from the relation

$$\alpha = \sin^{-1}\left(\frac{\Phi_0}{AB_{||}}\right) = 0.0725^{\circ}, \tag{A.1}$$

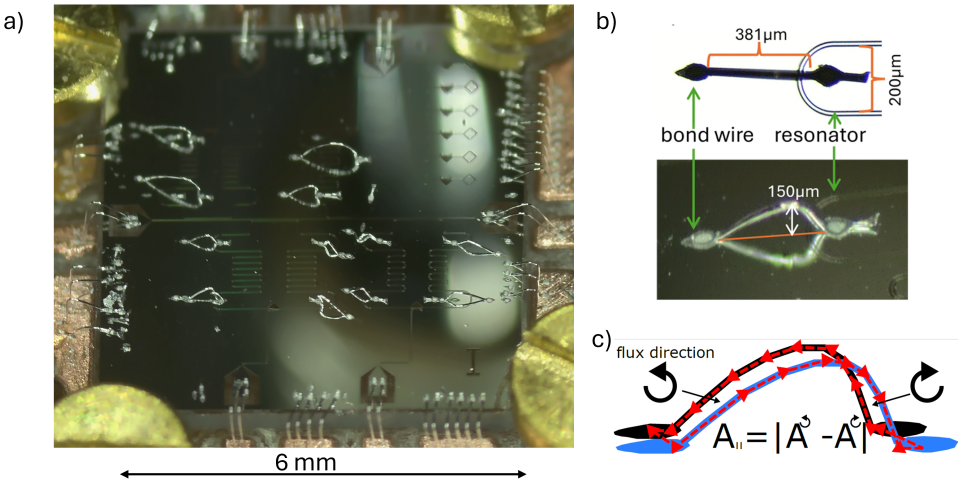

Figure A.1: a) Sample micrograph showcasing wirebond placement. b) Microscopy from different angles used to determine a wirebond's length. c) Illustration how parallel wirebonds can form a partly gradiometric conduction path, reducing the effective loop area.

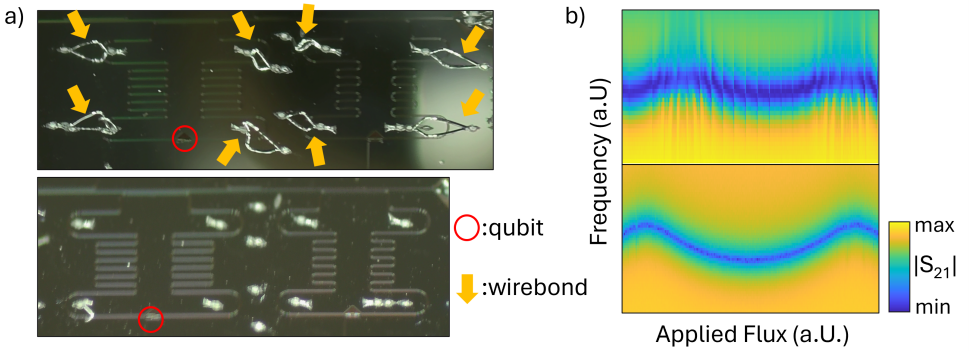

Figure A.2: Normal operation was restored by removal of wirebonds. a) Micrographs of the sample before (top) and after (bottom) removal of chip-to-chip wirebonds. b) Raw VNA data corresponding to the resonator frequency shift shown in Figs. 5.2. Disturbances in the modulation vanished after removal of wirebonds.

where the field $B_{||}$ generated by the solenoid is estimated from COMSOL simulations.
The p-SQUID's effective loop area $A_{pSQ,||}$ can accordingly be estimated from the periodicity of the dips in the resonator frequency (Fig. 5.3) as a function of the estimated $B_{||}$-field strength. This results in

$$A_{pSQ,||} = \frac{\Phi_0}{B^0_{||}} = 2068\,\mu m^2. \tag{A.2}$$

The effective p-SQUID area is rather small due to gradiometer effects in the wirebond connections, as illustrated in Fig. A.1 c).

After removing chip-to-chip wirebonds, normal qubit operation was restored as shown in Fig. A.2.

Acknowledgements

I would first like to express my gratitude to my supervisor, Jürgen Lisenfeld, for his good natured guidance, and continuous support throughout my doctoral studies. I am grateful that I was able to discuss any problem with him, professional and private.

My thanks go to Professor Alexey V. Ustinov, for giving me the opportunity of doing this research. I am grateful for the research environment he provided and the academic freedom I enjoyed in this group.

I am also grateful to Hannes Rotzinger for the good conversations we had, and the practical advice he gave me.

I would also like to thank my friend Alexander Konstantin Händel for the good times we had as colleagues and for mentoring me during my transition from theoretical physics into laboratory and cleanroom work.

I further thank my friend Etienne Daum for having been a great student who later became a helpful, and cherished colleague.

Further thanks go to my friend Julian Feiler, for making work more fun.

I would like to express my gratitude for the entire work group for the friendly atmosphere, and all the moments we shared.

I thank the cleanroom team of the CFN lab for their engagement. Especially Lucas Radtke and Silvia Diewald were indispensable for this work.

I am grateful to my friends and family from Solingen, who supported me from the distance, and the new friends I made here in Karlsruhe.

Finally, I want to acknowledge the larger circumstances that enable scientific research in the first place, which all too often are taken for granted. In that vein, I am grateful for a stable society, civil infrastructure, the rule of law, freedom of expression, and the human spirit of curiosity and cooperation.